DOTTORATO DI RICERCA IN INDUSTRIAL AND INFORMATION ENGINEERING AND ECONOMICS

CURRICULUM CHEMICAL ENGINEERING

XXXVIII CICLO

TESI DI DOTTORATO IN

Recycling Of Spent Batteries And E-Wastes Of The Automotive Sector With A Circular Economy Approach By Integrated Hydrometallurgical Processes

SSD: ICHI-01/C

Coordinatore del Corso
Prof. Katia Gallucci

Dottorando
Touseef Younas

Tutor
Prof. Francesco Veglio'

Anno Accademico 2024/2025

Declaration

I hereby declare that the work presented in this thesis, entitled "*Recycling Of Spent Batteries And E-Wastes Of The Automotive Sector With A Circular Economy Approach By Integrated Hydrometallurgical Processes,"* is my original research carried out in the *Department of Industrial & Information Engineering & Economics*, *University of L'Aquila*. This work has not been submitted in part or in full for the award of any other degree or diploma at this or any other university.

All the information derived from the published or unpublished work of others has been duly acknowledged and referenced in the text.

This PhD work was supported by VITALITY and carried out in the ambit of some R&D activities of LIFE-GRAPHIREC. This thesis is submitted in partial fulfillment of the requirements for the degree of Doctor of Philosophy at the University of L'Aquila.

Touseef Younas
PhD candidate
Department of Industrial & Information Engineering & Economics
University of L'Aquila
Date: December 20, 2025

Dedication

I dedicate this thesis to my beloved family, for their endless love, patience, and encouragement, and to everyone who believed in me. Your faith pushed me forward and has been my greatest strength throughout this journey.

Acknowledgments

I would like to express my deepest gratitude to my supervisor, ***Prof. Francesco Vegliò***, for his invaluable guidance, continuous support, and encouragement throughout the course of my PhD research. His expertise, constructive feedback, and patience have been instrumental in shaping the direction and quality of this work and thesis.

I am equally grateful to my co-supervisor, ***Prof. Valentina Innocenzi***, whose insightful suggestions, technical advice, and constant motivation have played a vital role in the successful completion of my research work. The combination of their mentorship has not only enriched this study but also greatly contributed to my academic and personal growth.

I sincerely thank the faculty members and staff of the *Department of Industrial & Information Engineering & Economics*, *University of L'Aquila*, for their valuable assistance and encouragement. I also wish to acknowledge my colleagues and friends in *Prof. Francesco Veglio's Lab* for their cooperation, discussions, and for creating a friendly and motivating environment. My special thanks go to ***Dr. Hossein Shalchian*** for his guidance, friendship, and support throughout this journey, ***Dr. Pietro Romano*** for his help and facilitation, and to ***Dr. Marco Passadoro*** for his valuable aid with ICP analysis, which significantly contributed to the success of my experiments.
I gratefully acknowledge the ***Vitality Project*** for its financial support, which made this research possible.

Finally, I owe the deepest gratitude to my family for their unconditional love, patience, and encouragement. Their unwavering support has been my strength throughout this journey.

Table of Contents

Abstract

Lithium-ion batteries are widely used worldwide in daily energy storage applications and electronics as they show high energy efficiency, high charge density, and long lifespan. Additionally, alkaline spent batteries are a type of portable battery used in household applications and electronic devices. Due to their high usage, a significant amount of spent batteries is also generated every year as waste. The recycling of these spent batteries is crucial not only for environmental sustainability but also for implementing a circular economy framework. These batteries contain harmful substances, such as electrolytes containing toxic organic solvents like ethylene carbonate (EC), Ethyl methyl carbonate (EMC), diethyl carbonate (DEC), dimethyl carbonate (DMC), and fluorinated salts like lithium hexafluorophosphate ($LiPF_6$) in lithium spent batteries and other compounds like Hg, Cd and Pb in alkaline spent batteries, that can cause health and environmental issues. The leakage of these electrolytes can contaminate soil and water through metal leaching, cause air pollution by releasing toxic gases such as carbon dioxide and hydrogen fluoride, and create health issues, including skin burns and respiratory problems, for humans. The lithium spent batteries also contain valuable materials such as Cu, Fe, Al, Mn, Co, Ni, Li, and graphite, in contrast, alkaline spent batteries contain potassium (K), manganese (Mn), zinc (Zn), and graphite, which can be recycled from battery waste to minimize raw material dependency in battery manufacturing, making it economically beneficial. There are various methods for recycling this type of waste, including pyrometallurgy, hydrometallurgy, and direct recycling. This study focuses on the development of integrated hydrometallurgical processes compared to conventional methods, which require high energy consumption, making them costly and resulting in increased carbon emissions. The elements from alkaline spent batteries (K, Mn, Zn) were recovered using two different recovery routes, in the form of nitrates and sulfates, via leaching with nitric acid (HNO_3) and sulfuric acid (H_2SO_4), respectively. Each recovery route has its own advantages, depending on the targeted product and its further use in different applications. The elements from spent lithium batteries (NMC-type and LFP-type) were recovered through hydrometallurgical methods using an acid-reductive leaching process (with acid and reducing agents such as H_2O_2), cementation, precipitation, and solvent extraction under mild conditions, thereby eliminating the high thermal energy demand associated with the roast-leaching route. A good recovery was achieved from NMC-type, with 85% of Cu, 83% of Fe-Al, 92% of Mn, 91% of cobalt, and 94% of nickel, while Li remained in the solution. From the LFP-type, 90.8% of Li and 98% of Fe recovered. Another work was also investigated in this study based on the

recovery of graphite from both lithium and alkaline spent batteries. The initial impurities in alkaline batteries were titanium (Ti), iron (Fe), barium (Ba), strontium (Sr), lead (Pb), and silica, which were removed through a two-step leaching process using acid and inorganic salts, yielding high-purity graphite with a purity of more than 94%. Graphite from lithium spent batteries was purified through counter-current leaching, yielding a graphite of good purity of >98%. This recovered graphite can be used for the remanufacturing of graphite anodes for batteries by mixing with the mined graphite. The overall study aimed to facilitate the transition to a circular economy by transforming battery waste into valuable secondary resources, thereby reducing reliance on virgin mining and mitigating environmental risks associated with the clean energy transition.

CHAPTER 1

Introduction

1.1 Background

Batteries have quietly become the most important part of everyday life as energy storage technology has improved. Today, people are completely dependent on these batteries. They are used to power everything, from small household electrical devices to large renewable energy systems, including electric cars [1]. The most frequently employed batteries are lithium-ion batteries, also known as LIBs, and alkaline batteries. It also allows the application of more sustainable energy. Despite their advantages, these batteries present major environmental hazards when discarded improperly [2].

According to the recent survey, both types of batteries are important to accomplish the energy needs and power the electrical devices. The majority of domestic appliances based on alkaline batteries to power their portable electronics. It is composed of different metals such as potassium (K), zinc (Zn), and manganese (Mn). On the other hand, LIBs can store large amount of energy as compared to alkaline batteries [3]. Therefore, LIBs are used to power electric vehicles and large electronic devices. It is composed of graphite, aluminum (Al), copper (Cu), nickel (Ni), cobalt (Co), manganese (Mn), and lithium (Li) [4].

Despite its importance, discarding these batteries improperly without following a proper procedure causes considerable environmental damage. If these batteries are discarded or burned, carcinogenic fumes and flammable chemicals are disposed of into the soil and water. Which causes serious health risks [5]. By considering these hazards, recycling and reusing are not choices; in fact, it's essential to protect the environment as it helps to slow down the depletion of resources, cut down the waste, and conserve resources [6].

The production of LIBs has increased dramatically due to a rapid expansion of renewable energy technologies and the electric vehicle industry. They are an essential component in reducing greenhouse gas emissions due to their high energy content and long lifespan. However, over one-third of all greenhouse gas emissions come from transportation [7]. As more people switch to electric vehicles, a new issue arises: what to do with all the dead batteries? According to the recent studies, researchers predict that millions of tons of this type of waste will accumulate annually by the end of this decade [8], [9].

Recent studies only focused on the recycling of LIBs compared to alkaline batteries [10]. However the alkaline batteries also play a significant role in environmental pollution and contain valuable metals that need to be recovered to conserve the resources. Therefore, recycling of both batteries are critical to transform this waste into an opportunity by creating a **circular battery economy** focused on resource recovery instead of disposal.

1.2 The Global Requirement for Battery Waste Management

The global transition to renewable energy has an impact on the transportation of materials. The demand for metals used in batteries is expanding rapidly [11]. Increasing resources, on the other hand, often causes government problems and harms the environment. In this scenario, recycling and reusing spent batteries are advantageous to the environment while conserving resources.

Recycling is particularly crucial because incorrect disposal of old batteries can affect ecosystems by accumulating heavy metals, flammable liquids, and acids in landfills [12]. On the other hand, LIBs may be harder to store and handle at recycling centers because they pose more risks, such as the chance of burning and short circuits. In addition to being concerned about the environment, it is also important to protect resources. Recycling plays a significant role by ensuring a consistent supply of resources while lowering the dangers associated with them.

As discussed earlier, LIBs include valuable metals such as Li, Co, Ni, Mn, Cu, and Al. Within the European Union, Li, Co, and Ni are acknowledged as Critical Raw Materials (CRMs). It is essential to identify secure, sustainable sources of these materials within the EU [12], [13]. Alkaline batteries offer a more user-friendly experience than LIBs. Additionally, it encompasses recoverable metals such as Zn and Mn. These metals play a crucial role in the production of chemicals, fertilizers, and alloys.

As a result, recycling is a key approach that not only relieves mining pressures, but also uses less energy than new extraction and maintains the stability of the battery sector [14]. Despite the obvious advantages, global recycling rates remain low. For example, only approximately 20% of batteries in the EU are recycled. Progress has been slow since there are no good methods for collecting, safely disassembling, and processing items together[15]. Therefore, it is essential to find a thorough and safe recycling system for alkaline and LIBs.

1.3 The Complexity of Battery Recycling Processes

Recycling of batteries consists of several steps before they are treated with chemicals. Usually, it starts with collecting, sorting, and safely separating the different parts[16], [17]. After that, the materials are recovered physically and chemically.

1.3.1 Safe Handling and Dismantling

The first and most important step in recycling is dismantling. Usually, it follows a step-by-step process. First, big EV packs entail the disconnection of high-voltage circuits. After that cooling lines are removed, and the separation of hundreds of cells is carried out, as shown in Figure 1 (parts 1 and 2). There are two types of dismantling: manual and automatic [18]. During manual handling, worker safety and health are at risk of exposure to chemicals, burns, and electric shock. Compared to manual dismantling, automatic dismantling is safe. However, automation poses some challenges due to the absence of a universal dismantling standard, which is a result of the design differences between manufacturers [19].

Therefore, it is crucial to develop structured and safe manual dismantling protocols. A consistent dismantling strategy assures worker safety and increases the purity of recovered materials, which has a direct impact on the quality of subsequent recovery procedures [14]. In this study, dismantling is viewed as a core process rather than a preliminary phase.

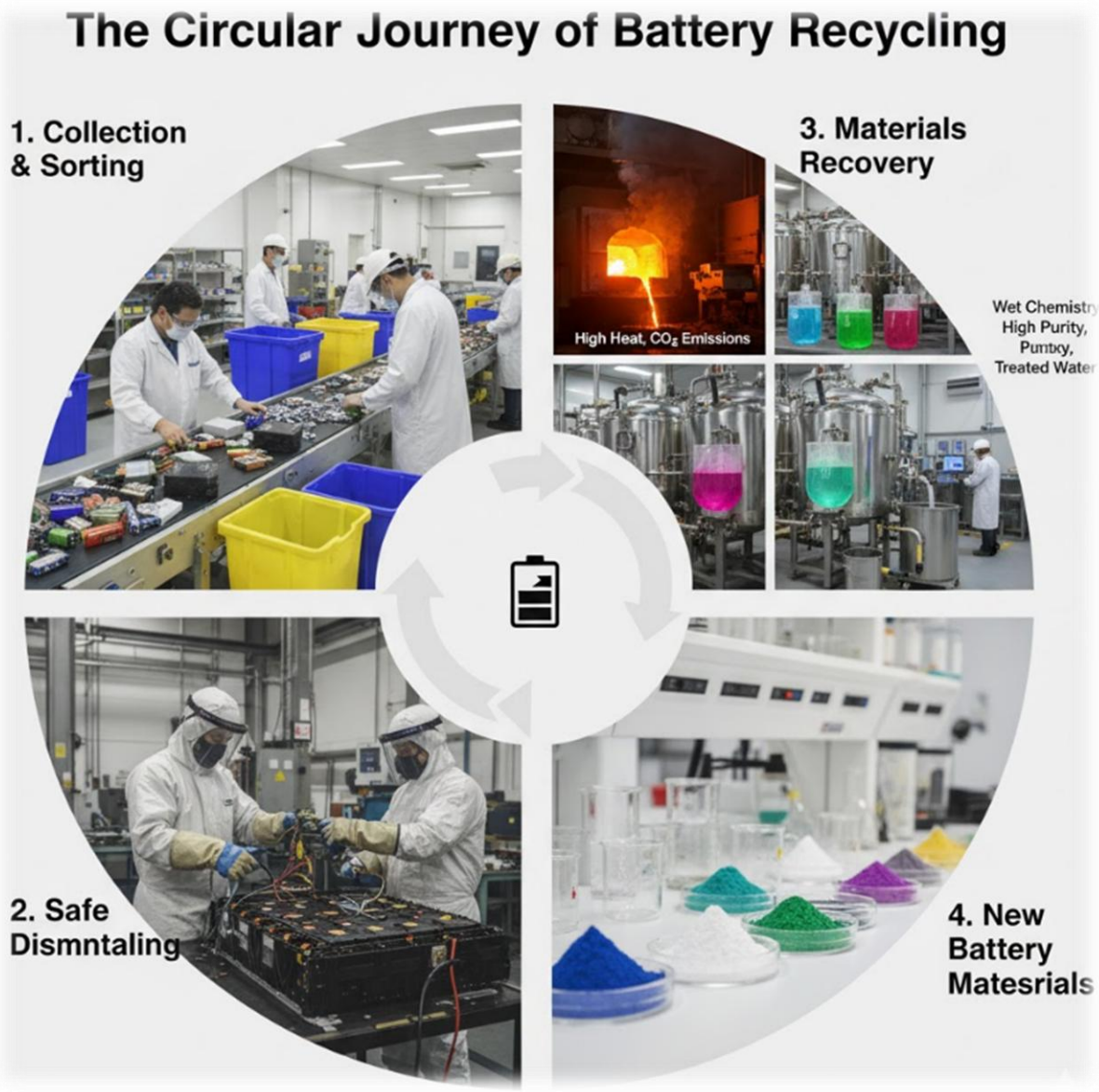

Figure 1: Visualizing the circular process of battery recycling: (1) collecting and sorting, (2) safe dismantling, (3) material recovery, and (4) new battery material synthesis.

1.3.2 Material Recovery Methods

Following the dismantling of the samples, they were subjected to chemical treatment, which was followed by the physical and chemical recovery of the materials.

- **Pyrometallurgy:**

  Pyrometallurgical methods involve the high-temperature melting of valuable metals, which increases their industrial application due to efficiency and simplicity. Fluxing agents such as silica (SiO_2), lime (CaO), and sodium carbonate (Na_2CO_3) are widely utilized in these processes [20]. These help to create slag and separate metals. Nonetheless, there is an urgent need to increase environmental sustainability because

these processes consume significant energy, produce hazardous gases, cause lithium loss during high-temperature operations, and require specialized treatment equipment [21].

- **Hydrometallurgy:**
  Hydrometallurgical techniques use a variety of chemical processes for mineral extraction, such as acid-base leaching, solvent extraction, precipitation, ion exchange, and electrolysis [22]. Metals are typically dissolved in these operations using powerful acids such as sulfuric acid (H_2SO_4), hydrochloric acid (HCl), and nitric acid (HNO_3). Hydrogen peroxide (H_2O_2) is commonly used to improve leaching efficiency. Following leaching, organic solvents such as Cyanex 272 and D2EHPA are used to separate and purify metals such as Co, Li, and Ni. Some procedures use ammonia (NH_3) or oxalic acid to selectively precipitate metals.
- Because these procedures frequently work at lower temperatures and have a lesser environmental impact, they are ideal for Li recovery.

On the other hand, the hydrometallurgy industry faces its own set of challenges, including the generation of significant acid waste, which poses risks to both human health and the environment, as well as increased disposal costs. Beyond typical recycling technologies such as pyrometallurgy and hydrometallurgy, direct recycling is seen as a more straightforward solution because it reduces the number of procedures required to manufacture new cells. It minimizes energy use, battery costs, and greenhouse gas emissions, thus improving the environment [22].

Direct recycling involves removing pieces from obsolete batteries and repurposing them to build new batteries while leaving their structure or morphology intact, which helps to preserve the quality of the cathode material [23]. Direct recycling uses supercritical carbon dioxide (CO_2) to extract materials from cathodes and anodes, allowing for electrolyte recovery during dismantling and crushing of cells. This technology separates cell components using physical processes, facilitating the reuse of cathode materials [24].

1.4 Current Limitations and Research Directions

In comparison to prior years, the world is now more aware of the importance of battery recycling. However, considerable gaps are still present in both research and industrial practices. Currently, there are numerous methods for recycling spent batteries. However, the majority of them concentrate only on recovering a small number of high-value metals. This indicates that

some resources are not being fully recovered and disposed of. Considering these factors, developing a sustainable and circular battery economy is difficult when addressed from such a narrow perspective.

Furthermore, significant research and effort are dedicated to lithium-ion systems due to their increased market value compared to alkaline batteries. However, it is important to understand that alkaline batteries also constitute a significant portion of global battery waste. They also include metals that can be recycled, such as Zn and Mn. Unfortunately, limited research was conducted on the recovery of these metals, particularly in the context of nitrates and sulfates via hydrometallurgical leaching. Many individuals possess these batteries, resulting in a lack of effective large-scale recycling solutions for them. This suggests that valuable resources are being wasted, which makes the environment worse.

Moreover, an important element of lithium-ion cells is graphite. Generally, it undergoes pyrometallurgical processes that lead to combustion or is disposed of as waste in hydrometallurgical approaches. Recycling and recovering these components have the potential to greatly reduce the waste and pollution linked to the process. This outcome would yield high-quality carbon suitable for the production of new anodes or for diverse industrial applications. The issue of graphite recovery continues to lack sufficient focus, which negatively impacts both the economy and the environment. This study also aims to address that issue.

Still, a lot of research focuses on chemical extraction while ignoring the crucial physical dismantling phase that is necessary for recycling to be both safe and efficient. Therefore, safety and disassembly remain crucial concerns. There is a pressing need for risk assessment frameworks and structured disassembly procedures that may be applied to all battery types without endangering material quality or safety.

Another problem is making sure that processes are sustainable, especially when it comes to managing wastewater. Hydrometallurgical recycling generates significant amounts of acidic, dissolved metal, and organic wastewater. These increase the Chemical Oxygen Demand (COD) of water if released without treatment, causing further environmental issues. Most studies focus on recovering metals and not treating waste streams. Sludge reduction and COD removal in recycling are crucial to environmental sustainability [25].

A comprehensive framework unifying all aspects of battery recycling is lacking. Current research often focuses on specific chemistries, such as lithium or alkaline concentrate, exclusively for selective metal extraction. A comprehensive model that integrates both metal

and graphite recovery from these battery types, alongside safe disassembly and efficient wastewater treatment, remains unavailable.

This study aims to develop a secure, comprehensive, and durable recycling system for depleted alkaline and lithium-ion batteries. The primary objective of the study is to explore environmentally friendly hydrometallurgical and extraction techniques for recovering valuable metals and graphite. The primary objective is to complete the material cycle by transforming used batteries into new, valuable resources, all while minimizing waste and pollution. This study is significant due to its thorough approach to methodology. Previous studies have often focused on battery types and recycling methods separately, typically emphasizing only the high-value metals. This research combines the processes of recycling alkaline and lithium batteries into a cohesive methodological approach. The research outlines a self-sustaining system that effectively recovers metals and graphite, while also ensuring safety and managing wastewater efficiently.

1.5 Thesis Structure

This thesis is structured into eight chapters, demonstrating the sequential and logical progression of research activities.

- **Chapter 1**: gives the basic idea of the whole thesis by giving the background and the problem statement. It also discusses the aims and importance of the work that was carried out. It also gives a general idea of how the thesis is put together, with a short summary of each chapter.
- **Chapter 2** includes the materials and reagents used to carry out the work, with experimental methods and characterization techniques in detail that have been applied to carry out the research work. The procedures described here include acid attack, leaching, cementation, precipitation, solvent extraction, counter-current leaching, and protocols for graphite recovery. The characterization techniques include XRF, TGA, LOI, Moisture, Ball milling, ICP-OES, Particle size distribution (PSD), and XRD.
- **Chapter 3** describes the recovery of elements associated with alkaline spent batteries. These elements are potassium, manganese, and zinc, which are being recovered in the form of salts. Two different strategies were employed in the recovery process, utilizing two distinct acids. Each recovery strategy has its own benefits, depending on the targeted materials in the product and their intended uses.

- **Chapter 4:** focuses on how to obtain precious metals out of the black mass of used Li-ion batteries. This section addresses a way to recycle NMC-type spent Li-ion batteries. These batteries have valuable metals in them, like copper, aluminum, iron, manganese, cobalt, nickel, and lithium. The work employed different methods, like cementation, precipitation, and solvent extraction, which are also discussed.
- **Chapter 5:** describes how Li and Fe were taken out of the spent lithium-ion batteries. Different hydrometallurgical experiments were carried out to get these elements from the LFP-type Li-ion battery scrap. It also explains how to selectively extract these elements and how statistically important each method is.
- **Chapter 6**: is about the recycling of high-purity graphite from spent alkaline batteries. The first impurities were taken out using a hydrometallurgical method, resulting in a high-purity graphite that can be used to make battery anodes.
- **Chapter 7**: includes the steps performed and the results of recovering graphite from spent Li-ion batteries. The process produced highly pure graphite by getting rid of the impurities through leaching.
- **Chapter 8**: summarizes the main results and presents the problems and limits that came up during the research. It also gives ideas for how to move forward with a large-scale recycling process for different materials, such as graphite from used lithium and alkaline batteries.

1.6 Summary

This research offers a distinctive and essential cohesive framework for the recycling of both alkaline and lithium batteries, integrating domains that have historically been examined in isolation. By concentrating on the combined recovery of metals and graphite, it promotes material circularity and endorses sustainable manufacturing practices.

The results are expected to help shape future industrial practices by:

- Improving the recovery efficiency of less-prioritized materials like graphite.
- Providing clear protocols for generating valuable precursor chemicals (nitrates and sulfates) for new battery production and other applications.
- Reducing environmental pollution through effective wastewater management and sludge minimization.

This study is very important because it looks at how to combine wastewater treatment and process safety directly into the recycling chain. It aims to provide the battery industry with not only the best possible material recovery, but also sustainable environmental protection and long-term sustainability.

CHAPTER 2

Experimental Methods and Analytical Techniques

2.1 Introduction

In this chapter, a detailed description of the experimental procedures for the hydrometallurgical recovery of critical metals from LiBs and alkaline batteries was provided. Later, the working principles of some analytical techniques used in this study were also discussed before moving to the next chapters. Each experimental technique describes the basic procedure, working principle, and advantages. This study deals specifically with two cathode chemistries: lithium iron phosphate ($LiFePO_4$, LFP) and lithium nickel manganese cobalt oxide ($LiNiMnCoO_2$, NMC), and alkaline spent batteries.

In the first part of this chapter, the experimental procedures for the recovery of LiBs or alkaline batteries are described, which first involve the mechanical pre-treatment, followed by crushing, grinding, and sieving [26]. After that, ball milling was generally used, which is considered an important step to convert the samples into fine powders for further experiments. After mechanical pre-treatment, the sample is generally moved towards drying to measure moisture content, to remove possible volatile liquids such as electrolyte, and to determine ignition loss in the furnace. Then, chemical treatment is performed, using various methods such as leaching, solvent extraction, and precipitation [27], [28]. In the second part of the chapter, the basic principles and working processes of analytical characterizations are described, which were carried out using ICP, XRF, CHNS, XRD, PSD, and TGA/DTA techniques to evaluate the efficiency and selectivity of metal recovery at each stage.

2.2 Experimental Methods

2.2.1 Mechanical pre-treatment

Mechanical pre-treatment is an important phase in the recycling of some critical metals present in LiBS and alkaline batteries. The process involves physical grinding of battery components using various pre-mechanical techniques, including crushing and shredding of large components, and then separating different particle sizes by sieving and magnetic separation [29]. As these batteries are composed of different compartments that vary in composition; therefore, a grinder is required to grind or separate each material effectively. Additionally, the mechanical properties of different battery components vary significantly, including the toughness of metal foils and the brittleness of electrode coatings. To begin the process, the air is usually excluded from the grinding chamber to reduce the air exposure and dust emissions.

For the grinding, a number of tools are used, including hammer mills, blade crushers, and granulators.

After grinding, the deactivated batteries are crushed and shredded, a process that roughly divides into some larger and smaller fragments based on differences in density and magnetic characteristics. The larger fragments are mostly current collectors composed of Cu and Al, as well as plastic separators and steel casing [30]. However, the smaller pieces are actually active electrode materials (cathode and anode). After that, these fragments are separated by size through sieving to improve the purity of each fragment. Sometimes the separation of parts may be sorted by their density and magnetic properties to separate these specific materials more effectively. This process helps to selectively isolate non-ferrous metals, ferromagnetic parts, and carbonaceous materials. A detailed systematic visual representation was shown in Fig. 2.

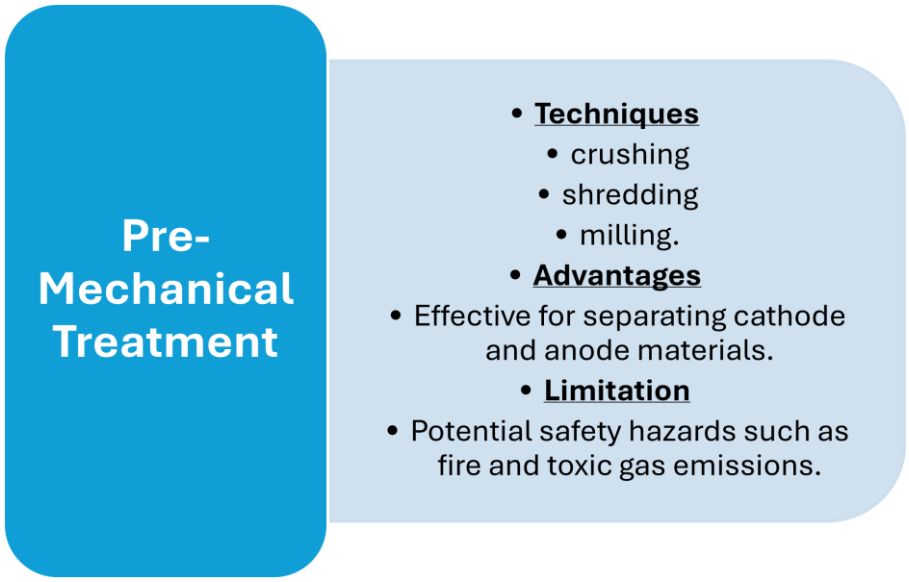

Figure 2: Visual representation of pre-mechanical treatment

- **Working Principle**

This technique follows the principle of size reduction and material separation. It applies structured mechanical energy to break down the weak edges or connections of complex layers of battery electrodes and casings. This energy enables the physical separation of the crushed material based on various factors such as particle size, magnetic properties, and density. A suitable and efficient separation system should be applied, as this process can cause noise, generate dust, and emit harmful gases during its operation [31]. Even so, this process is used effectively due to the following advantages:

Advantage

- Allows recovery of individual fractions (metals, polymers, and active mass) without chemical reagents.
- Simple, scalable, and cost-effective.
- Provides feedstock of uniform particle size for subsequent hydrometallurgical steps.
- Minimizes reagent consumption and improves leaching efficiency.
- Can be coupled with automated separation systems for industrial operation

2.2.2 Ball Milling

The last and most crucial step in the mechanical pre-treatment of LIBs and alkaline batteries is ball milling after the crushing and shredding, which served to obtain a homogeneous, fine powder with enlarged surface area for subsequent chemical reactions. In this operation, the black-mass powder was loaded into a sealed cylindrical jar together with hard milling balls (zirconia or stainless steel) and rotated at a constant speed. As the jar turned, the balls were lifted and then dropped under gravity, repeatedly striking the particles. The combined effects of impact, friction, and shear progressively reduced particle size and detached the remaining coatings of **$LiCoO_2$, $LiFePO_4$, or MnO_2** from the metallic foils [32].

- **Working Principle**

The working principle of ball milling relies on the transfer of kinetic energy from moving balls to the particles. Continuous collisions and sliding motion lead to mechanical deformation and refinement of the powder (Figure 2). During milling, jar temperature was monitored, and short cooling intervals were introduced to prevent overheating or oxidation [33]. Appropriate control of milling duration and speed was essential to balance efficiency with material stability., as depicted in Fig. 2.

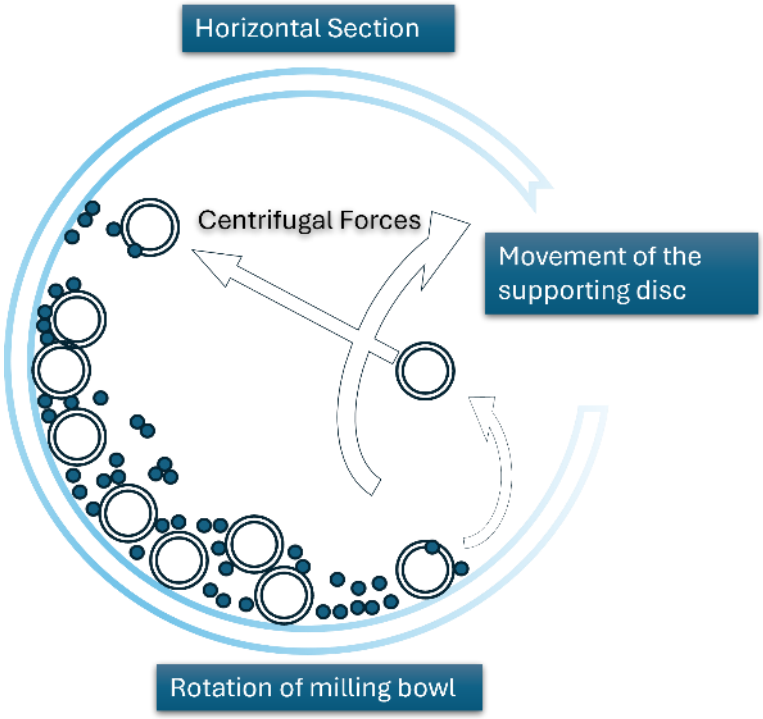

Figure 2: Schematic illustration of a ball motion and powder mixture

Advantages

- Produces fine and uniform powders with enhanced reactivity.
- Promotes the detachment of active materials from current collectors.
- Increases surface area, which improves the kinetics of subsequent leaching.
- Can induce partial mechanochemical activation of oxides.
- Operates under ambient conditions with a lower energy cost compared to thermal treatments.

2.2.3 Moisture Content and Loss on Ignition (LOI)

After the initial mechanical process, the processed black material or powder obtained from LIBs and alkaline batteries may still have some moisture and leftover liquid from the battery's electrolyte. Determining and removing this moisture is important to make sure that the mass of the sample is accurate before chemical analysis or leaching.

2.2.3.1 Moisture Content Using Oven Drying

The oven-drying method is based on a simple principle: the moisture evaporates when the sample is heated. Furthermore, the amount of moisture lost can be calculated by measuring the weight before and after drying [34].

In this process, about 2–5 grams of the black mass are placed in a clean and dry crucible and then heated in an oven at a temperature of 105 °C for around 12 hours. After heating, the sample is cooled in a desiccator to avoid moisture absorption from the air and then weighed again as shown in Fig. 3. The difference between the initial and final weights represents the percentage of moisture in the sample [35].

Figure 3: Moisture Content Using Oven Drying

Advantages

- Simple, reliable, and inexpensive.
- Provides true dry weight for accurate solid-to-liquid ratios.
- Prevents side reactions caused by residual moisture.
- Ensures consistency between analytical and experimental stages.

2.2.3.2 Loss on Ignition (LOI) Using Furnace

The Loss on Ignition (LOI) is used to measure the amount of volatile substances, organic materials, and carbon residues that burn off when the black mass is heated to a high temperature. In this method, a known amount of the dried sample is put in a clean crucible and then heated in a muffle furnace at about 950 °C for 2 hours. After heating, the crucible is cooled in a desiccator and weighed again. The difference in weight before and after heating represents

the percentage of material lost, primarily due to the burning of carbon, binder, and other volatile compounds [36]. This test is important because it helps to estimate the amount of non-metallic impurities in the recycled material and provides information about its composition and purity.

Advantages

- Estimates non-metallic and organic impurities.
- Confirms purity and readiness of samples for chemical processing.
- Helps optimise furnace and leaching parameters.
- Simple and repeatable analytical procedure

2.2.4 Leaching

The active material, which is obtained from the battery scrape after the pre-treatment, is usually called black mass [37]. This material is shifted toward the leaching step, which is a crucial step for the high yield during a hydrometallurgical recovery method. Any metal or material that is not leached out into the leaching solution cannot be recovered, as it remains in the sludge. The aim of the leaching process is to dissolve metals present in calcinated cathode and anode scrap powder (black mass) with the assistance of a leaching agent [38]. This process is typically performed using various acidic media such as sulfuric acid (H_2SO_4), nitric acid (HNO_3), and hydrochloric acid (HCl). Commonly, H_2SO_4 is used as the leaching agent owing to its low cost and high efficiency in breaking the crystal lattices of Li and transition-metal oxides [39]. On the other hand, mineral acids (HCl and HNO_3) have also been used. But during their reactions, they produce toxic gases like chlorine (Cl_2) and nitrogen oxides (NO_x) [40].

Conversely, alkaline or basic leaching agents such as potassium hydroxide (KOH) and sodium hydroxide (NaOH) are generally less effective, particularly in dissolving valuable metals like Co and Ni. Additionally, strong acids and bases often lead to corrosion in processing equipment. Due to these complications, researchers are now investigating various organic acids, for example, oxalic acid ($C_2H_2O_4$) and citric acid ($C_6H_8O_7$), as possible leaching agents by determining their potential as safer and more environmentally friendly substitutes for conventional leaching agents like sulfuric acid [41].

Sometimes, while selecting a suitable leaching agent, a reducing agent is also needed. For example, if Co(III) or some other useful metals like Mn(III) are present in the black mass, they need to be converted to lower valence ions like Co (II) or Mn (II) to be more stable in the leaching solution [42]. Usually, hydrogen peroxide (H_2O_2) is a good choice among all the

reducing agents at 3- 5% wt or even more, as no additional anion or cation is introduced in solution.

- **Working Principle**

Leaching is based on the principle of chemical dissolution. When the solid material is exposed to a solvent or acid, the metal oxides or compounds react with the leaching agent to form soluble metal ions. These ions then migrate into the liquid phase, leaving behind insoluble residues. Various parameters, such as type and concentration of the acid, reaction time, temperature, particle size, and agitation speed (rpm). These parameters should be optimized to ensure a high recovery yield with minimal reagent consumption**.**

Advantages:

- Allows high metal recovery under relatively mild conditions.
- Controlling different parameters such as pH, acid concentration, and temperature allows selective extraction.
- Relatively lower energy consumption compared to pyrometallurgical processes.
- Able to incorporate organic acids that help
- reduce environmental impact.

2.2.5 Solvent Extraction

Solvent extraction is a technique to separate and purify a targeted element from the solution. In this research work, this technique is used to separate different elements such as manganese, cobalt, and nickel from the leaching solution. These elements are extracted selectively using different solvents and dilutants combinations. These solvents can be polar or nonpolar; selection is based on the targeted metal. The pH of the solution during solvent extraction is carefully controlled and monitored as it can greatly affect the extraction efficiency and selectivity. For example, an increase or decrease in the pH can cause co-extraction of other elements along with the targeted component and can affect the purity [43].

- **Working Principle**

In solvent extraction, a solute distributes itself between two solvents in such a way that these solvents are immiscible and have no affinity for each other. These solvents are referred to as the organic phase and aqueous phase. The organic phase is a suitable solvent for the selective

elemental recovery and is based on the nature of the elements to be extracted. Sometimes, a combination of organic solvent and a suitable dilutant is used as the organic phase. The aqueous phase is a leaching solution containing the targeted elements. During the mixing of both phases, the extractant of the organic phase reacts with the metal ions in the aqueous phase and shifts them to the organic phase [44]. The extracted metals in the organic phase are removed using some fresh solutions, usually containing acids or complexing agents, and act as the aqueous phase. A good extraction efficiency can be achieved by carefully controlling reaction conditions (pH, temperature, etc) and by selecting a suitable solvent for the selective elements [45].

Advantages:

- High selectivity and purity of recovered metals.
- Mild operating conditions and re-usable extractants.
- Lower solid-waste generation compared with precipitation alone.

2.2.6 Precipitation

This method is commonly used in the recovery process to extract selected metals from the leaching solution because of the solubility variations of metal compounds at specific conditions, like temperature and pH. Basically, precipitation was used to recover Li and other dissolved metals, such as Fe and Al, from the purified leachate by converting them into solid compounds. High-purity Li compounds are achievable due to the ability of Li to precipitate out selectively [46].

Metals are separated using reagents such as NaOH, Na_3PO_4, and Na_2CO_3, which enable Li to form Li_2CO_3 by adding sodium carbonate (Na_2CO_3) or lithium hydroxide (LiOH) by adding calcium hydroxide ($Ca(OH)_2$) and Li_3PO_4 precipitates. Particularly, because of its low solubility, Li_2CO_3 readily precipitates at regulated pH and temperature levels. In addition to this, precipitating Li as Li_2CO_3 is more easy since increasing the pH of the leachate increases the availability of carbonate ions (CO_3^{2-}) in the solution [47].

Figure 4: visual representation of precipitation

- **Working Principle:**

Precipitation is based on the recovery of some elective elements, such as lithium, iron, and aluminium, from the leaching solution with the help of some precipitants. These precipitants are selective for different kinds of metals and are added under controlled conditions to effectively recover the elements from the solution.

Advantages:

- Simple, low-cost method using common reagents.
- Produces high-purity lithium salts ready for reuse.
- Adaptable to industrial scale and environmentally safer than some solvent routes.
- Precipitation thus completes the hydrometallurgical cycle by producing a stable lithium product suitable for re-manufacturing.

2.3 Analytical Techniques

2.3.1 ICP-OES

The Inductively Coupled Plasma Optical Emission Spectroscopy (ICP-OES) is utilized to find the elemental concentrations in the solution during the process. It is used as a characterization technique to measure the elemental composition of the samples quantitatively, as well as a semi-qualitative technique to find traces or impurities of elements in the sample. The results produced by this technique are versatile, rapid, and sensitive up to ppb and ppm, with very low interferences [48].

- **Working Principle**

The principle of working depends upon photon generation of specific wavelengths as a result of excited atoms or ions by a high-temperature plasma, and is powered by a radio frequency generator. The intensities of the emitted photons are measured and compared to known standards to estimate the concentrations of various elements in the solution [49]. A schematic diagram of ICP-OES instrumentation is shown below:

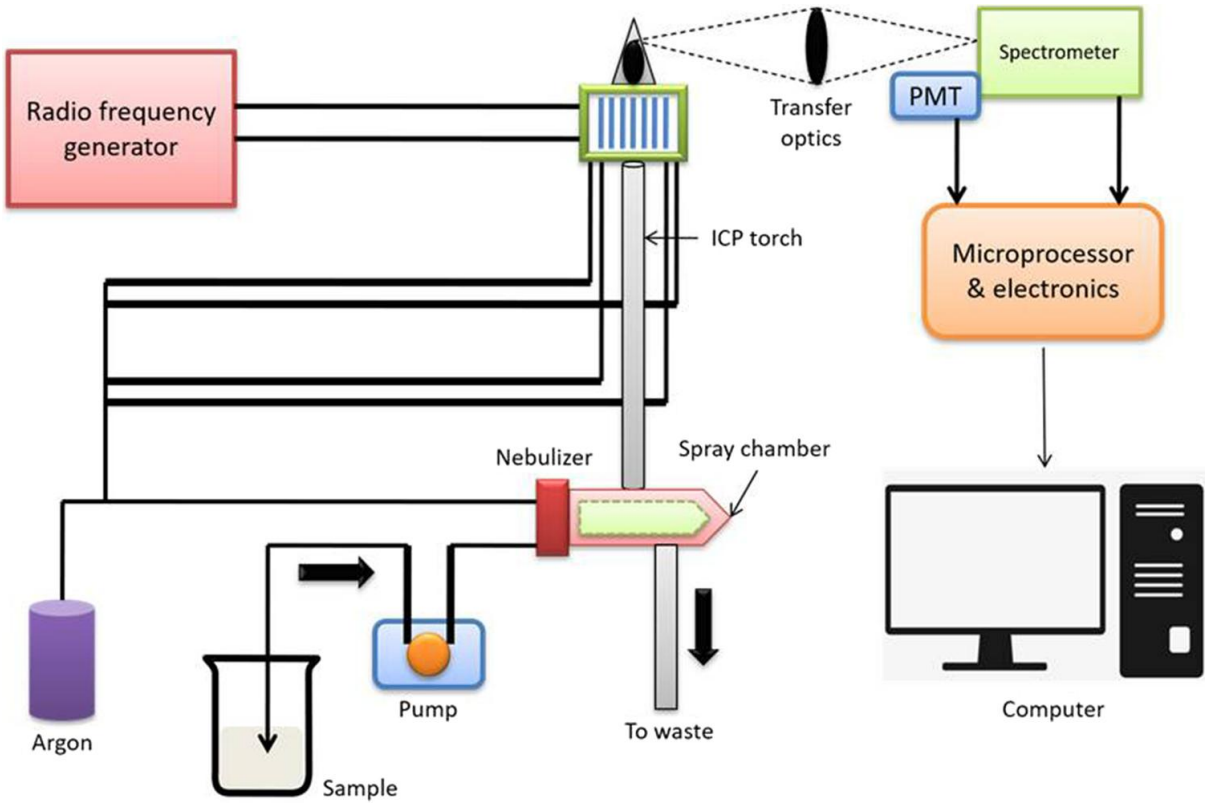

Figure 5: Instrumentation of ICP-OES with different components

The most important part of the instrumentation is a suitable nebulizer to convert the liquid sample into aerosols so that it can be atomized and ionized well by the plasma discharge. The plasma is high-pressure argon gas, and it produces good aerosols, required for ICP analysis. The nebulized sample is shifted to an ICP torch form nebulizer with the help of a spray chamber, where it contacts with plasma discharge. The ICP torch has three tubes: for argon flow, an aerosol injector, and one auxiliary flow tube for high-speed argon gas passage. A radio frequency generator is used to supply power to plasma discharge. The emissions from plasma discharge are collected by focusing optics, usually called a convex lens or concave mirror. These optics generate an image of discharged emissions on the input slits of a wavelength-

dispersing device. The intensity of the emissions is measured by an Emission Detector. These measured signals are processed by a photomultiplier tube and converted to computer data for further processing, resulting in the final information. Software is also generally used to simplify the instrumental operations and develop analytical methods for final reporting [49].

Advantages

- Provides rapid, sensitive, and accurate multi-element analysis with high reproducibility.
- Enables simultaneous detection of both trace and major elements.
- Capable of analyzing light elements such as lithium, which are difficult to detect by XRF.
- High-temperature plasma minimizes matrix interferences for reliable results.
- Suitable for quantitative analysis of both liquid and solid samples in recycling studies.

2.3.2 X-Ray Fluorescence Spectroscopy (XRF)

It is a non-destructive analytical technique utilized to measure the initial elemental composition of the samples quantitatively. The qualitative and quantitative composition of the sample can be determined by measuring intensity and energy of these emitted X-rays. which were used to calculate the mass balances of the different processes, particularly for Fe and phosphorus, as Li cannot be detected due to its low atomic radius [50].

- **Working Principle**

XRF follows a process in which atoms are excited by ejecting electrons from the innermost orbitals with high-energy radiations. When the atom relaxes as the outer electrons fill inner shells, X-Ray fluorescence radiation is emitted at that time. All this happens without damaging or touching the sample [51].

The emitted radiation acts like a fingerprint for each atom. For example, the fluorescence of Cu differs significantly from the Zn fluorescence and from that of any other element fluorescence in the periodic table [52]. This unique characteristic makes X-ray fluorescence (XRF) one of the simplest and most convenient methods for elemental analysis.

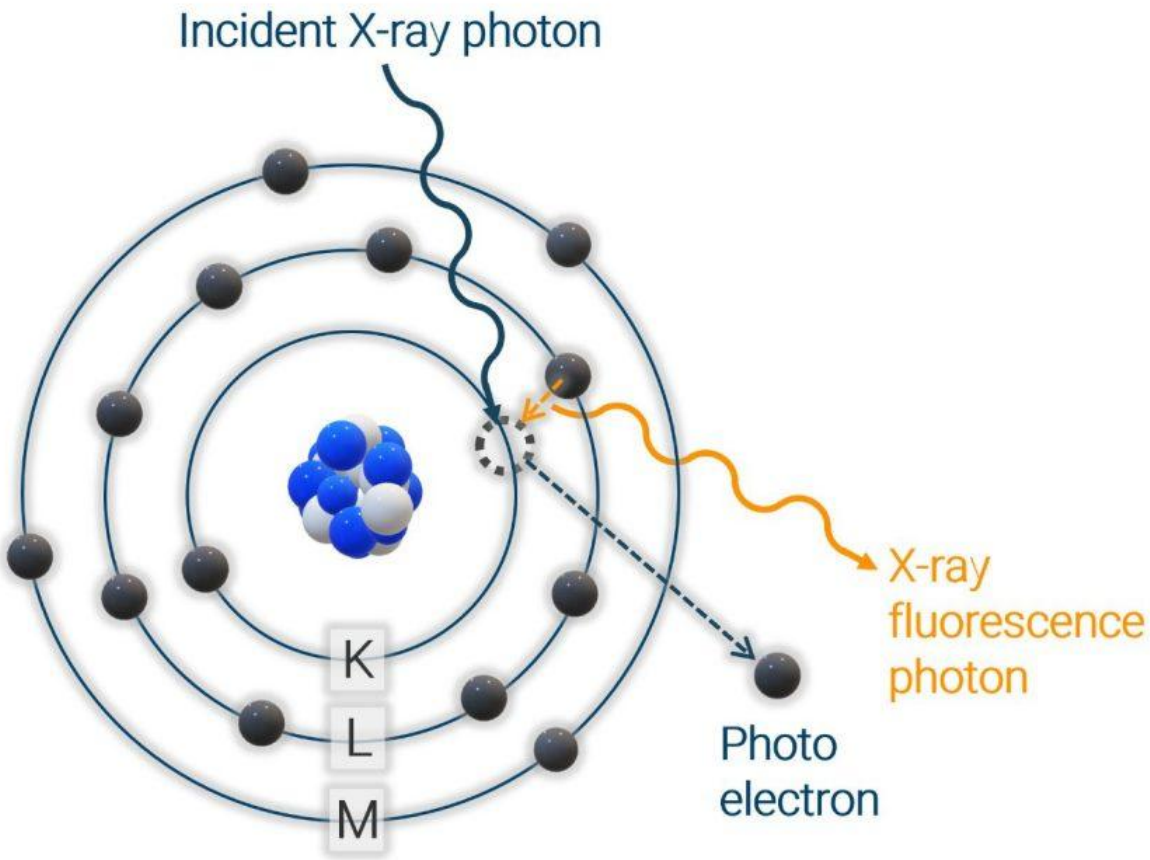

Figure 6: Demonstration of the interaction of X-rays with the material

Advantages

- It is a non-destructive method and requires minimal sample preparation.
- It provides sensitive, rapid, simultaneous multi-element analysis.
- Suitable for solids, powders, and liquids.
- Highly accurate for medium to heavy elements.

2.3.3 CHNS Analysis

This analytical technique is utilized to find the composition of elements in organic and inorganic substances. The percentages of carbon (C), Hydrogen (H), Nitrogen (N), and sulfur (S) are determined in the materials.

- **Working Principle**

The sample undergoes a complete combustion during the analysis at a very high temperature, almost 900°C to 1200°C, in oxygen-rich environment. The reaction mechanism of these elements during the combustion is as follows:

For Carbon,

$C + O_2 \rightarrow CO_2$ (Carbon Dioxide CO_2 is released)

For Hydrogen,

$H_2 + O_2 \rightarrow H_2O$ (Vapours of water are produced)

For Nitrogen,

$N + O_2 \rightarrow NO_x \text{ or } N_2$ (convert to nitrogen gas)

For Sulfur,

$S + O_2 \rightarrow SO_2$ (sulfur dioxide, SO_2 gas emits)

These gases, which are being produced during the combustion, are separated in another column and are measured. The amount of an element present in the initial sample depends on the quantity of these gases [53]. The instrumentation diagram and brief descriptions of the different components are provided below.

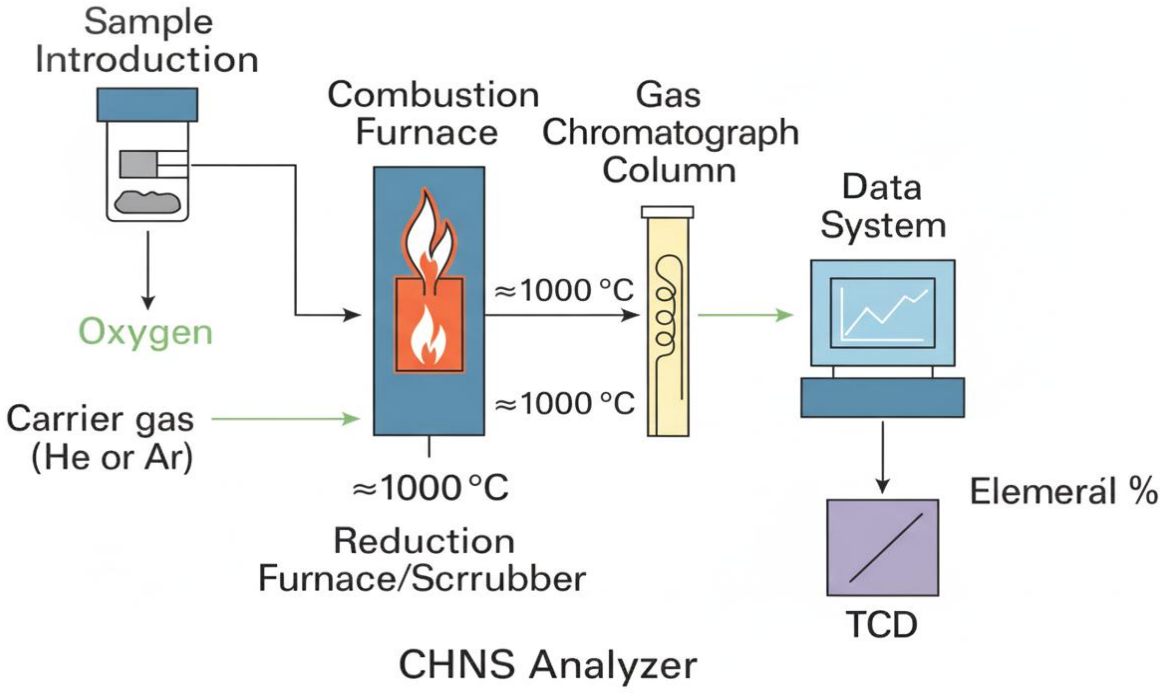

Figure 7: Instrumentation of the CHNS analyzer with different components

In the combustion chamber, the sample is turned into gaseous oxides by burning in a rich oxygen environment, and an excess of oxygen is then removed in a reduction furnace. These gases are then moved to the next column by some gas-carriers such as helium (He) or Argon (Ar). The mixed stream of the gaseous oxides is separated selectively for their individual detection in a gas chromatography column. The thermal conductivity of every separate gas is

measured by a thermal conductivity detector or TCD. From the detected peaks by TCD, the percentages of the elements (C, H, N, S) are calculated by a data processor unit [53].

Advantages

- Real-time determination for C, H, N, S
- Quick and accurate measurement is usually in minutes
- A very small amount of sample (1 to 3 grams) is required for analysis
- All types of samples are analysed (solid, liquid, and powder)

2.3.4 X-ray Diffraction (XRD)

This technique is applied to find structural properties like crystal or amorphous structures, phase compositions, and the orientation of a sample. It is a non-destructive technique where X-rays are generated in a cathode ray tube due to the interaction or collisions of high-energy electrons with a material and causing the emission of X-rays. The generated X-rays further produce monochromatic radiation that is focused on the sample under study. These radiations scatter in a precise direction after interacting with matter and determine the crystal lattice. The peak intensity is measured by the constructive interference of monochromatic X-rays, which are scattered or diffracted from a crystal structure [54].

- **Working Principle**

A typical XRD system has three main components, as shown in Fig. 8, including a sample holder for sample introduction, an X-ray source that can generate X-rays, and a detector. X-rays are emitted from the source and then directed toward the sample and interact with crystalline phases of the sample. The detector produces a diffraction pattern by capturing the diffracted X-rays. Additionally, the diffraction angle, denoted as 2θ in Fig 8, is the angle formed between the diffracted and incoming X-ray beams. By controlling this angle, the intensity of the X-rays can be measured. The angle between the incident beam and the sample can vary based on the diffractometer's design and the sample's properties [55].

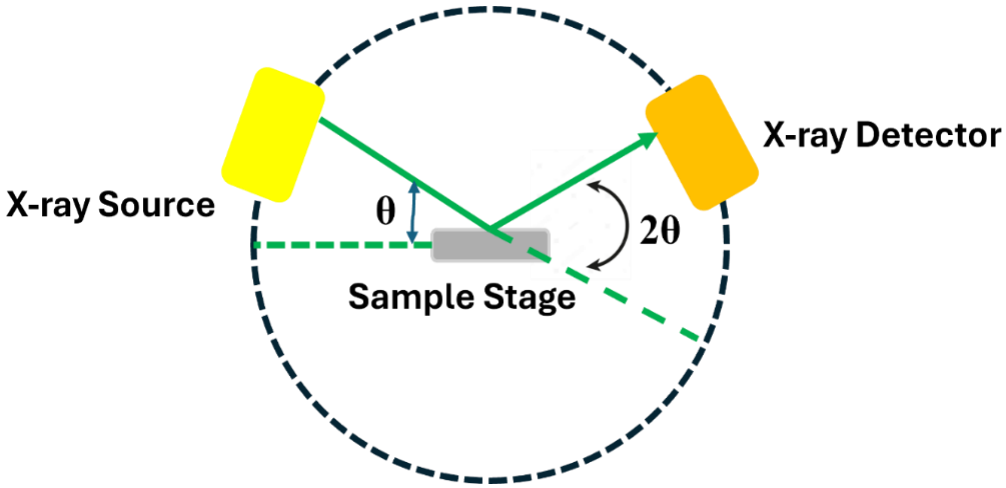

Figure 8: Schematic representation of XRD

Advantages

- Provides a precise identification of crystalline phases and compounds.
- Determines the crystal structure, lattice parameters, and degree of crystallinity.
- Non-destructive technique requiring minimal sample preparation.
- Suitable for both qualitative and quantitative phase analysis.

2.3.5 Particle Size Distribution

Particle size distribution (PSD) is used to determine the particle size, as indicated in the name, and to indicate the range and proportion of particles in the sample.

- **Working principle**

In battery recycling, PSD analysis is commonly performed by laser diffraction, which helps to measure the size distribution of particles obtained after mechanical pre-treatment. Mostly, PSD is performed after crushing and sieving. When a laser beam passes through the dispersed powder, larger fragments scatter the light at smaller angles, whereas smaller particles scatter at wider angles. The scattering data are then analyzed to evaluate the range of particle size and distribution of the processed material [56].

Advantages:

- It can help in the optimization of separation processes as it correlates particle size with the composition of material.

- By assessing the overall uniformity of the powder material, it can help in controlling leaching and recovery steps.
- It gives rapid and reproducible results with accuracy for both granular and fine fractions.
- The mechanical pre-treatment efficiency can be evaluated in terms of grinding, milling, and sieving.

2.3.6 TGA/DTA

The mass of the samples can be determined by thermogravimetric analysis (TGA/DTA) on the basis of a thermogram output obtained when the sample is exposed to a temperature change. A graphical thermogram is plotted after the analysis, which is the representation of the relationship of the mass of a sample and temperature or time. The decomposition temperature and thermal stability of the sample can be estimated, along with the identification of any plastics, filters, or polymers present in the sample that is being treated under this technique [57].

- **Working Principle**

TGA/DTA follows a simple principle, in which a sample is placed in a furnace with well-controlled temperature using a small crucible. The sample is heated at a constant rate with precise temperature control. The mass change of the sample is monitored continuously and precisely during the heating procedure. A highly sensitive and accurate balance is used to measure the change in mass. The changes that occurred in the mass of the sample under heating are due to the different phenomena (physical or chemical), such as decomposition, oxidation, and dehydration.

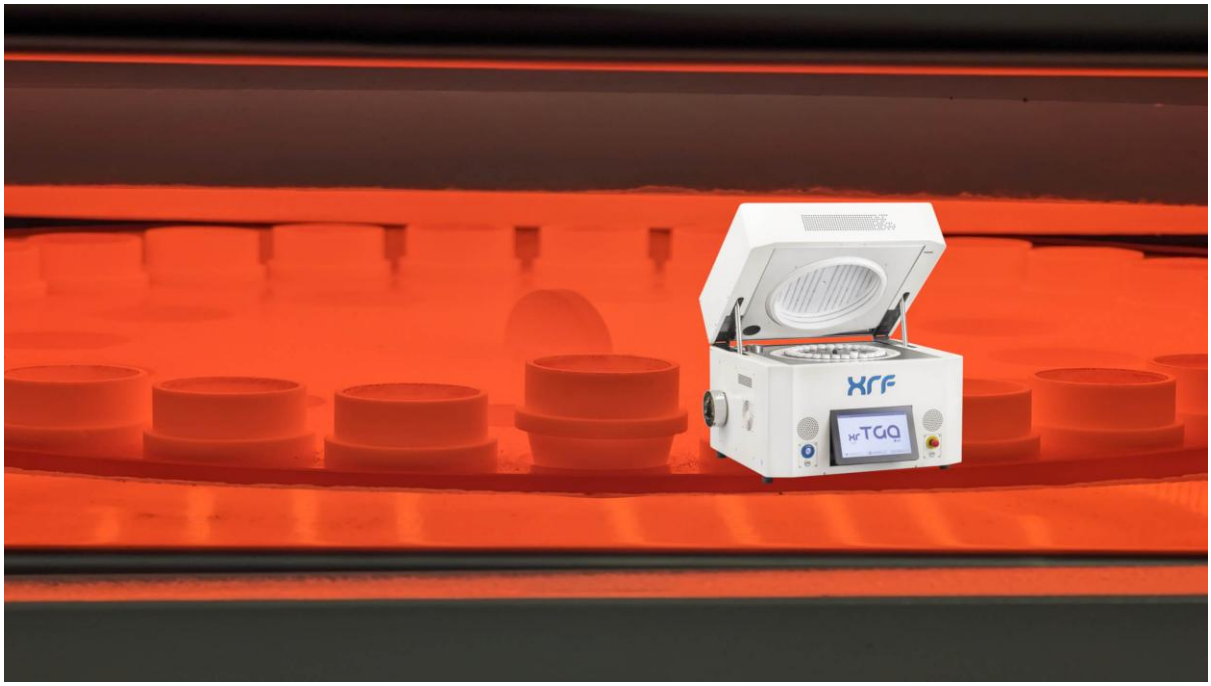

Figure 9: Visual representation of the TGA analyzer

Advantages

- Applicable to a wide range of materials, including polymers, metals, ceramics, and composites.
- Provides quantitative information on composition, decomposition, and thermal stability.
- Highly sensitive to small mass changes, allowing accurate analysis of minute samples.

CHAPTER 3

Recovery Of Different Elements From Alkaline Spent Batteries In The Form Of Nitrates And Sulphates: A Comparative Study

3.1 Introduction

Alkaline batteries are a portable type of primary battery that are extensively used in daily life and household devices like calculators, clocks and watches, toys, remote controls, and similar gadgets[58]. Every year, a large amount of these batteries are generated worldwide due to their short lifespans[59]. As these batteries contain some valuable elements such as manganese, zinc, iron, and copper[60], so it is critical that these elements need to be recovered. Besides this, some harmful substances such as Hg, lead, and cadmium are also associated with these kinds of spent batteries[61]. The discharge of these toxic chemicals into the environment is a serious concern as it can pollute the soil as well as groundwater. Taking these aspects into consideration, the alkaline spent batteries along with zinc-carbon batteries, should be collected and recycled in both environmental and economic scenarios[62].

For the recovery procedure of valuable metals from alkaline spent batteries, some mechanical pretreatments, for example, crushing, sieving, and magnetic separation, are performed to obtain different material fractions[63]. These fractions include a brass fraction, a steel scrap fraction (both these fractions can be recycled in industrial plants), and a black mass fraction (which contains mostly oxides of manganese and zinc)[64]. Recovery processes for manganese and zinc are generally considered as hydrometallurgical, pyrometallurgical, and sometimes bio-metallurgical[65], [66], [67].

In the hydrometallurgical process for the treatment of black, usually acid leaching is performed with the aim of converting manganese and zinc into soluble compounds like sulphates and nitrates[68]. After that, zinc and manganese are recovered separately with different techniques, like precipitation and electrowinning[69]. Despite a large number of investigations for the recovery of Mn and Zn, which focus on sulphate recovery through hydrometallurgical process using sulfuric acid leaching, the nitrates routes using nitric acid leaching are still unexplored[70]. These nitrates have very valuable industrial applications due to their high solubility. Due to the lack of comparative analysis of sulfates and nitrates for the recovery of Mn and Zn, it has compromised the understanding of the best recovery route for high leaching and selective efficiency with minimum chemical consumption and impurities.

This research work is a comparative study on the recovery of multiple elements like K, Mn, and Zn in the form of their nitrates and sulphates. The recovery could have a yield of marketable potassium salts (KNO_3 and K_2SO_4), along with fertilizer-grade zinc salt ($ZnSO_4$) and battery-grade manganese salt ($MnSO_4$) due to high purity and selectivity. The samples for conducting this research were provided by the COBAT industry.

3.2 Materials and Methods

3.2.1 Sample preparation

The mechanically opened alkaline spent battery scrap was crushed and subjected to ball milling to achieve a homogeneous black mass consisting of oxides of elements like Mn, Zn, K, and electrolyte. A fine fraction was obtained by sieving the sample (with <100µm sieve), dried overnight at 65°C, and stored in airtight container for further use.

3.2.2 Chemicals and Standards

All the chemicals used for this work were of analytical grade. H_2SO_4 (95-98%) for solution preparations of concentration of 1-2 M, while HNO_3 (65-69%) for solution concentration of 1-3 M was used for the leaching process. KOH and NaOH were used for adjusting pH, and $KMnO_4$ was used for precipitation. All the solutions were prepared using distilled water, and certified multi-standards for the calibration of ICP were used.

3.2.3 Apparatus and Equipment

The experimental work was carried out in clean glassware with continuous stirring and heating. A pH meter with the probe inside the reactor and a vacuum filtration system was used, with filters of size 0.50µm. An oven was used for drying the sample, and a characterization technique (ICP-OES) for the concentration of metal content in the solution.

3.2.4 Leaching and Precipitation

The measured volumes of sulfuric and nitric acids with different concentrations ranging from 1-2 M and 1-3 M were carefully used. The leaching was performed with different reaction conditions, time (1-3 h), temperature (25-80°C), and solid-to-liquid ratio (10-20%). Some elements were precipitated out with varying pH values using KOH, and for some others using different stoichiometric values of $KMnO_4$. The precipitated crystals were dried in the oven for further analysis.

3.2.5 Environmental and Safety Measurements

All the solution preparations and leaching experiments were performed with controlled conditions under the fume hood with proper PPE measures. The residual metals from the waste

solution were fully precipitated, and the acidic waste was neutralized within the pH range of 6-8 before discarding. All the solid residues were disposed of as hazardous materials according to the institutional regulations.

3.3 Results and Discussion

3.3.1 Selective Recovery Of Elements From ASB As KNO_3, $Zn(NO_3)_2$ and $Mn(NO_3)_2$ Using Nitric Acid

The different elements present in alkaline batteries (K, Zn, Mn) can be recovered from the black mass in the form of nitrates. These nitrates are very useful industrial and fertilizer compounds due to their high solubility. They could be used as precursor chemicals for many industrial syntheses, like ceramics, solution processing, and purifications. The other unique benefit of nitrates is their property to convert into pure metal oxide after thermal decomposition. These metal oxides are very useful for further chemical synthesis, like pigments, catalysts, and mordants in textiles. The following work was done to recover these nitrates from the black mass of spent alkaline batteries:

3.3.1.1 Characterization of Black mass

Three samples of as-received black mass were dissolved in aqua regia to determine the content of Mn, Zn, and K. The results are presented in Table 1.

Table 1. Chemical attack results from the black mass

Run	Mn (%)	Zn (%)	K (%)
1	30.55	22.84	4.65
2	30.21	23.92	4.73
3	30.94	21.27	5.06
Average	30.57	22.68	4.81

3.3.1.2 Water leaching experiment

In processing the black mass of alkaline batteries, it is necessary to perform a water leaching to remove potassium hydroxide before acid leaching. Otherwise, acid consumption will be increased. A water leaching experiment was performed at room temperature and pulp density of 20% for 1 hour. Results are presented in Table 2. Potassium removal percentages were calculated by measuring the potassium concentration in the washing solution using ICP and performing a mass balance on the initial weight of the solid and its potassium content, as shown in Table 1.

Table 2. Neutral leaching conditions and results for potassium removal

Pulp density (%)	Temperature (°C)	Time (h)	V initial (ml)	V final (ml)	% K	pH of the final solution
20	25	1	50	85	61.08	10.88

As can be seen, only about 61% of the total potassium is soluble in water, and the remaining value appears to be in the form of water-insoluble compounds. It should be noted that the solid residue after leaching was washed using some water during filtration. So, the final volume of the solution increased to 85 ml.

The final solid residue was dried at 50 °C for a day. The weight loss result of the dried filter cake after water leaching is shown in Table 3. It should be noted that the total weight loss is the sum of the moisture content of the as-received black mass (before leaching) and the amount of KOH removed during leaching. So, considering 61% removal of K as KOH, the weight of KOH is calculated, and the net weight loss due to KOH removal is determined. Consequently, the total moisture content of as-received black mass could be calculated, considering total weight loss and the net weight loss due to KOH removal (Table 3).

Table 3. Weight loss results for water leaching and mass balance

Initial weight (g)	Final weight (g)	Weight loss (%)	Net weight loss due to KOH removal (calculated)	Moisture content
10.007	8.920	10.86	4.21	6.65

3.3.1.3 Nitrate production of different elements

In this section, two strategies can be considered for producing potassium, zinc, and manganese nitrates, using nitric acid:

- Producing relatively pure nitrates of K, Zn, and Mn
- Producing a mixture of nitrates of K, Zn, and Mn

In the following, one strategy is investigated, starting with the first one, which is a more complicated process than the second one. It is obvious that the first strategy could be considered more valuable due to the production of pure nitrates.

3.3.1.4 Producing pure nitrates of K, Zn, and Mn

In this section, a process is developed for producing pure nitrates of K, Zn, and Mn. The proposed process is illustrated in Fig. 1. Therefore, the various stages of this process are examined in the following sections.

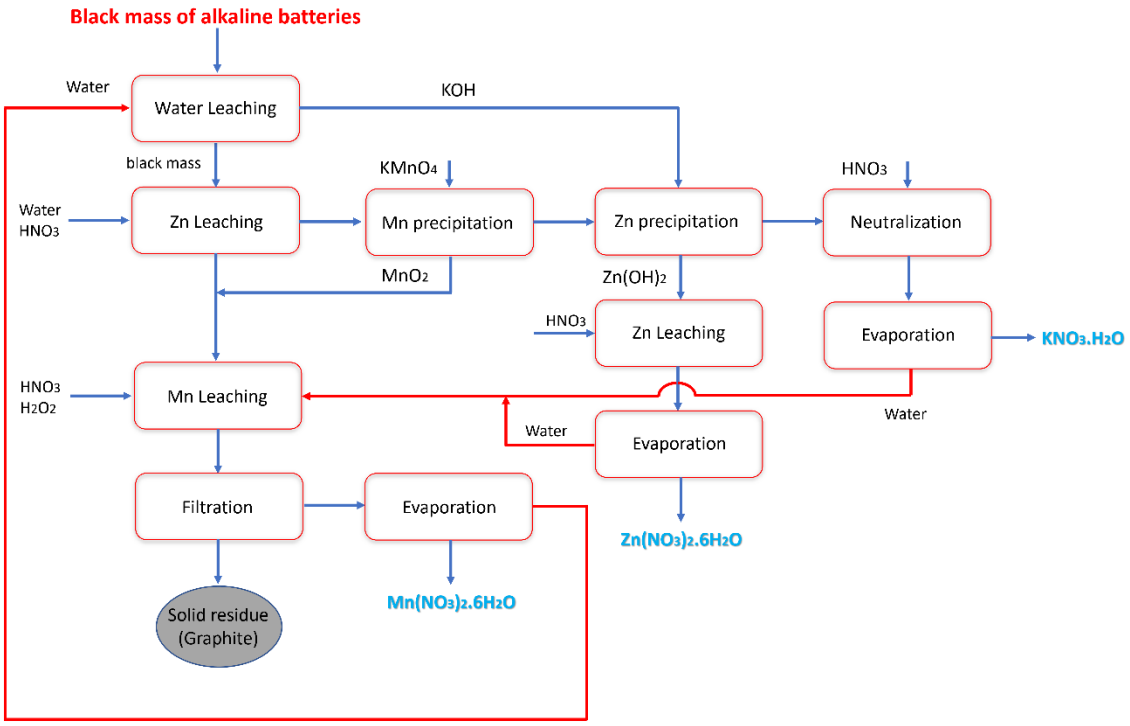

Fig. 1. Proposed process diagram for production of pure K, Zn, and Mn nitrates.

3.3.1.4.1 Selective leaching of Zn

Zinc oxide in the black mass can be dissolved in nitric acid according to the following equation:

$$ZnO + 2HNO_3 \rightarrow Zn(NO_3)_2 + H_2O \qquad \Delta G_{25°C} = -44\ kJ \qquad (1)$$

In addition, some manganese of the black mass can also be dissolved according to the following reactions:

$$MnO + 2HNO_3 \rightarrow Mn(NO_3)_2 + H_2O \qquad \Delta G_{25°C} = -89\ kJ \qquad (2)$$

$$Mn_3O_4 + 4HNO_3 \rightarrow 2Mn(NO_3)_2 + MnO_2 + 2H_2O \qquad \Delta G_{25°C} = -88\ kJ \qquad (3)$$

$$Mn_2O_3 + 2HNO_3 \rightarrow Mn(NO_3)_2 + MnO_2 + H_2O \qquad \Delta G_{25°C} = -38\ kJ \qquad (4)$$

According to the above equations, it can be seen that Mn_2O_3 and Mn_3O_4 are partially dissolved due to the formation of MnO_2 (equations 3 and 4), which is not soluble in nitric acid. Therefore,

it is possible to dissolve most of the Zn and only a portion of the Mn in one leaching step. For this purpose, several leaching experiments were conducted at different acid concentrations and temperatures for one hour. Pulp density and mixing speed were kept constant in all experiments at 20% (wt./v) and 250 rpm, respectively. It should be noted that in all experiments, the initial black mass underwent neutral leaching first, as outlined in Table 2. The remaining solid was then subjected to zinc-selective leaching. The nitric acid leaching conditions for the experiments are presented in Table 4.

Table 4. Leaching conditions for Zn selective leaching experiments

Test	HNO_3 Conc. (M)	Temperature (°C)	Time (h)	Pulp density (%wt./v)	Mixing speed (rpm)
1-25	1	25	1	20	250
1.25-25	1.25	25	1	20	250
1.5-25	1.5	25	1	20	250
2-25	2	25	1	20	250
2-80	2	80	1	20	250
2.75-25	2.75	25	1	20	250
2.75-80	2.75	80	1	20	250

Table 5 and Table 6 show the results for the above experiments. As can be seen, for an effective leaching of zinc from the black mass with a pulp density of 20% (wt./v) and leaching duration of 1 hour, nitric acid concentration should be more than 2 M, or temperature should be increased (Table 6). It is also possible to have high leaching efficiency of Zn in room temperature, but in nitric acid concentration as high as 2.75 M. Increasing temperature in 2.75M acid concentration is ineffective for Zn leaching but increases Mn dissolution from 33% to 39%. Table 6 shows that about 30% of K is dissolved in this leaching stage. Considering 61% of potassium dissolution in neutral leaching stage, about 90% of potassium is dissolved after neutral and selective acid leaching stages.

Table 5. Metal concentration for selective Zn leaching experiments at different conditions

Test	Solution	Volume (ml)	Concentration (mg/l)		
			Zn	Mn	K
1-25	Leaching liquor	49	21291	5619	2232
	Washing water	28	4539	1187	571

1.25-25	Leaching liquor	49	24403	7448	2248
	Washing water	18	7929	2325	847
1.5-25	Leaching liquor	50	22449	9835	244
	Washing water	30	6035	2027	580
2-25	Leaching liquor	48	34569	16046	2695
	Washing water	26	8268	3715	725
2-80	Leaching liquor	54	32633	15408	2633
	Washing water	24	7934	3609	624
2.75-25	Leaching liquor	49	37586	18649	2705
	Washing water	25	8199	4330	684
2.75-80	Leaching liquor	52	35779	21237	2583
	Washing water	30	6611	3629	437

Table 6. Leaching results for selective Zn leaching at different conditions

Test	**Leaching efficiency (%)**			**Initial weight (g)**	**Final weight (g)**	**Weight loss (%)**
	Zn	Mn	K			
1-25	51.61	10.10	26.05	10.018	6.754	32.58
1.25-25	59.03	13.31	26.06	10.006	6.246	37.58
1.5-25	57.48	18.08	29.00	10.006	5.783	42.20
2-25	82.66	28.36	30.80	10.011	4.885	51.20
2-80	86.11	30.06	32.65	10.022	4.812	51.99
2.75-25	90.26	33.44	31.10	10.003	4.541	54.60
2.75-80	90.80	39.69	30.63	10.007	4.305	56.98

Table 6 also shows the results of weight loss for all experiments. It is evident that weight loss is increased by higher acid concentration and temperature, due to the higher leaching efficiency of Zn and Mn, as indicated by the leaching results. The remaining solid is a mixture of undissolved manganese oxides and graphite, which is treated through a reductive leaching for Mn recovery.

3.3.1.4.2 Mn precipitation

The leaching solution from the previous stage contains most of the zinc from the black mass, but it also includes some manganese, which should be removed to produce pure nitrate

solutions of zinc and potassium. Manganese can be precipitated using a strong oxidising agent. Potassium permanganate is a suitable agent for this purpose. Mn (II) ions can be precipitated according to the following reaction:

$$2KMnO_4 + 3Mn(NO_3)_2 + 2H_2O \rightarrow 5MnO_2 + 2KNO_3 + 4HNO_3 \quad \Delta G_{25^\circ C} = -370\ kJ \quad (5)$$

For these experiments, the leaching liquor and washing water from tests 2-80 were mixed and treated with potassium permanganate. The pH value of the mixed solution was 2.38. Different concentrations of KMnO4 were added to 10 mL of the mixed solution and were mixed at room temperature for 30 minutes. The added value of $KMnO_4$ was selected at 0.95, 1, and 1.05 stoichiometric values, according to Equation 5. Table 7 shows the precipitation results.

Table 7. Precipitation results for different values of potassium permanganate

		Test Number			
		Mix solution	**1**	**2**	**3**
Added value of $KMnO_4$ (Respect to stoichiometric value)		-	0.95	1	1.05
Mass of $KMnO_4$ (mg)		-	215	225	236
Volume (ml)		10	26	24.5	30.5
Concentration (mg/l)	**Mn**	13820	465	288	30
	Zn	24508	8721	8947	7241
	K	1734	2506	2615	2283
Mass (mg)	**Mn**	138.2	12.08	7.06	0.91
	Zn	245.08	226.76	219.20	220.84
	K	17.34	65.14	64.06	69.67
Precipitation (%)	**Mn**	-	91.26	94.89	99.34
	Zn	-	7.48	10.56	9.89

In this table, the initial concentration of elements in the mixed solution and the final concentration after adding KMnO4 are represented for tests No. 1-3, and the initial mass of elements in the mixed solution and after precipitation (tests No. 1-3) are also represented.

As can be seen, the Mn concentration decreases from 13820 mg/L to 30 mg/L in Test No. 3, which is equivalent to 99.3% of Mn precipitation. Therefore, $KMnO_4$ addition should be a little more than the required stoichiometric value, according to equation 5. In this condition, about 10% of zinc is co-precipitated.

It should be noted that some value of potassium is inserted into the solution by adding $KMnO_4$, and this is the reason for the increment of potassium mass in tests No. 1-3 with respect to the initial mixed solution. Therefore, the final solution after Mn precipitation contains significant values of zinc and potassium nitrates, which should be separated in the next stages of the process.

Final solid of precipitated Mn as MnO_2 was filtered, dried, and kept aside to add to the solid residue of Zn selective leaching, for the next reductive leaching stage of manganese dissolution.

3.3.1.4.3 Zn precipitation

As stated above, the final solution of previous Mn precipitation contains Zn and K which should be separated. Zinc can be precipitated easily by increasing pH to an adequate value. Hence, in this section some experiments are performed to find suitable pH for complete Zn precipitation, leaving behind potassium in the solution. The previous test 3 from Mn precipitation section was selected for these experiments (initial pH of 0.7). In each test, 10 ml of solution was taken, and pH adjustment was performed by adding 20 ml of KOH solution obtained from initial neutral leaching (with pH of 10.8). Also, some excess KOH added to the solution for pH adjustment, using a 5M KOH solution. Solutions were mixed for about 15 minutes at room temperature after adding KOH. Then precipitated $Zn(OH)_2$ was filtered and washed using some washing water. The results are presented in Table 8.

Table 8. Zinc precipitation results by pH adjustment

		pH adjustment			
		Initial solution	**1**	**2**	**3**
Adjusted pH		0.7	10.06	11.97	13.23
Final pH after filtration and washing		-	9.82	10.93	12.7
Final volume (ml)		10	59	55	45
Concentration (mg/l)	**Mn**	30	0.06	0.24	0.21
	Zn	7241	0.17	0.55	143
	K	2283	2829	3945	10535
Mass (mg)	**Mn**	0.3	0	0.01	0.01
	Zn	72.41	0.01	0.03	6.46

	K	22.83	167	217	474
Precipitation (%)	**Mn**	-	98.82	95.58	96.84
	Zn	-	99.99	99.96	91.08

Table 8 shows that adjusting pH to 10 is suitable for precipitation of almost all of Zn, and increasing pH value to higher levels is not needed and even reduces Zn precipitation efficiency. It should be noted that Mn precipitation is almost completely done in this step, but the initial concentration of Mn is very low, about 30 mg/l in comparison with Zn (7241 mg/l).

3.3.1.5 Neutralization (potassium nitrate production)

According to Table 8, final solution after Zn precipitation contains only potassium in the form of KOH (with a low value of Zn only in test No. 3). So, these solutions can be turned to potassium nitrate solutions by neutralizing with HNO_3. Therefore, the last three solutions in previous section were neutralized by adding nitric acid. For the first and second solutions (pH of 10 and 12), neutralization performed very quickly, without any precipitation or change in the solution, by adding a few amounts of nitric acid. But, for the third solution (pH of 13.23), some precipitates formed during pH reduction. So, this solution was filtered and analyzed by ICP. The results are presented in Table 9. It is obvious that Zn concentration is decreased due to precipitations formed during the neutralization and reducing pH to 7 (Table 9). So, it is concluded that the precipitates should be zinc hydroxide. Finally, these three solutions are relatively high purity potassium sulfate solutions, which can be evaporated for crystallization of the salt.

Table 9. Analysis of solution of test 3 (pH 13.23) before and after neutralization

	Element	**Test 3 before pH adjustment (pH = 12.7)**	**Test 3 after pH adjustment (pH = 7.06)**
Concentration (mg/l)	**Mn**	0.21	0
	Zn	143	2.39
	K	10535	10187

3.3.1.6 Zn leaching (zinc nitrate production)

The obtained zinc hydroxide precipitates from Zn precipitation stage can be turned into zinc nitrates, easily. For this purpose, three precipitates obtained after pH adjustment (Table 8) were dissolved in 25 ml of 2M nitric acid solution. The precipitate of test 1 (pH of 10) was dissolved totally, without any solid residue, but the dissolution process of precipitates of test 2 and 3 was incomplete and some light brown solid residues were remained. The solutions were filtered and analyzed by ICP. Table 10 shows the results for the obtained zinc nitrate solutions.

Table 10. Analysis of zinc nitrate solutions (dissolving obtained zinc hydroxides in 25ml of 2M nitric *acid solution)*

Initial pH adjustment		**Precipitates**		
		1	**2**	**3**
		10.06	11.97	13.23
Concentration (mg/l)	**Mn**	11.48	9.33	5.09
	Zn	2771	2897.45	2334
	K	68.97	18.45	0.28
Mass (mg)	**Mn**	0.29	0.23	0.13
	Zn	70.66	72.44	58.34
	K	1.76	0.46	0.007
Purity of zinc in solution (%)		97.18	99.05	99.77

As can be seen, potassium concentration and zinc content of the precipitates are reduced by increasing pH, especially in test No. 3 (Table 10). Considering the brown solid residue after nitric acid leaching, it seems the solid residue is a complex compound of potassium and zinc. So, increasing pH in precipitation step is not suggested, because it leads to wasting some potassium and Zn by complex formation.

3.3.1.7 Mn leaching (manganese nitrate production)

As stated before, the solid residue after selective Zn leaching contains different manganese oxide, which need a suitable reducing agent for leaching. In addition, the precipitated MnO_2 after Mn precipitation stage, also added to this solid.

It is well known that Mn_2O_3 and Mn_3O_4 are partially dissolved due to the formation of MnO_2 (equations 3 and 4) which is not soluble in nitric acid, necessitates using a reducing agent for

the reduction of Mn (IV) to the soluble form of Mn (II). Accordingly, hydrogen peroxide can be used as an adequate reducing agent without inserting any impurities to the solutions. So, Nitric acid leaching reactions for different manganese oxides present in the black mass can be written in presence of hydrogen peroxide as follows:

$$Mn_2O_3 + 4HNO_3 + H_2O_2 \rightarrow 2Mn(NO_3)_2 + 3H_2O + O_2 \qquad \Delta G_{25°C} = -140\ kJ \qquad (6)$$

$$Mn_3O_4 + 6HNO_3 + H_2O_2 \rightarrow 3Mn(NO_3)_2 + 4H_2O + O_2 \qquad \Delta G_{25°C} = -190\ kJ \qquad (7)$$

$$MnO_2 + 2HNO_3 + H_2O_2 \rightarrow Mn(NO_3)_2 + 2H_2O + O_2 \qquad \Delta G_{25°C} = -101\ kJ \qquad (8)$$

It should be noted that some of Mn_2O_3 and Mn_3O_4 may dissolve in previous Zn leaching process partially, according to equation 3 and 4, which produces MnO_2. In this case the remaining MnO_2 can be dissolved according to equation 8. The solid residue and the added MnO_2 from Mn precipitation stage (Test 3) went through a reductive leaching according to the conditions in Table 11. The leaching results are presented in Table 12.

Table 11. Reductive leaching conditions for manganese oxides in black mass

M Solid residue (g)	**M precipitated MnO_2 in Test 3 (g)**	**V water (ml)**	**V HNO_3 (ml)**	**V H_2O_2 (ml)**	**Temp (°C)**	**Time (h)**	**Mixing speed (rpm)**	**Final solid weight (g)**
4.8	0.403	26	7	7	25	1	250	0.537

Table 12. Reductive leaching results for manganese oxides dissolution

	Volume (ml)	**Concentration (mg/l)**			**Mass (mg)**		
		Mn	**Zn**	**K**	**Mn**	**Zn**	**K**
Leaching liquor	**40.5**	55003	3986	497	2227.64	161	20.13
Washing water	**36**	8298	603	81	299	21.69	2.92
Total mass in solution		-	-	-	2528.17	184.57	23.28

Table 12 shows that the main element present in the solution is Mn. Some lower values of Zn and K also exist in the solution. It is obvious that by increasing leaching efficiency in the first

Zn selective leaching, the Zn concentration in this last solution will be decreased. So, relatively pure solution of manganese sulfate obtained in this way.

Finally, the solid residue was dissolved in aqua regia to determine the remaining values of Mn, Zn, and K in the solid phase. Table 13 shows the results. As can be seen, the remaining values of these elements are very low, and almost all these elements are dissolved in the two leaching stages process.

Table 13. Chemical analysis of final solid residue after Mn oxides leaching

Mass (mg)	**Volume (ml)**	**Concentration (mg/l)**			**Mass (mg)**		
		Mn	**Zn**	**K**	**Mn**	**Zn**	**K**
62	50	4.16	3.36	0.51	0.208	0.168	0.025
Mass in the whole solid residue (0.537 g)					1.80	1.45	0.22

3.3.2 Recovery Of Elements As K_2SO_4, $ZnSO_4$, And $MnSO_4$ Solutions From Alkaline Spent Batteries Using Sulfuric Acid

In this section, an optimization approach was considered to recover potassium, zinc, and manganese sulfate solutions separately. An optimization process was performed mainly on the zinc selective leaching and manganese reductive leaching stages. Some modifications were also made to the process to improve the purity of the products. The modified process compared to nitric acid is illustrated in Fig. 2, which is followed in this section.

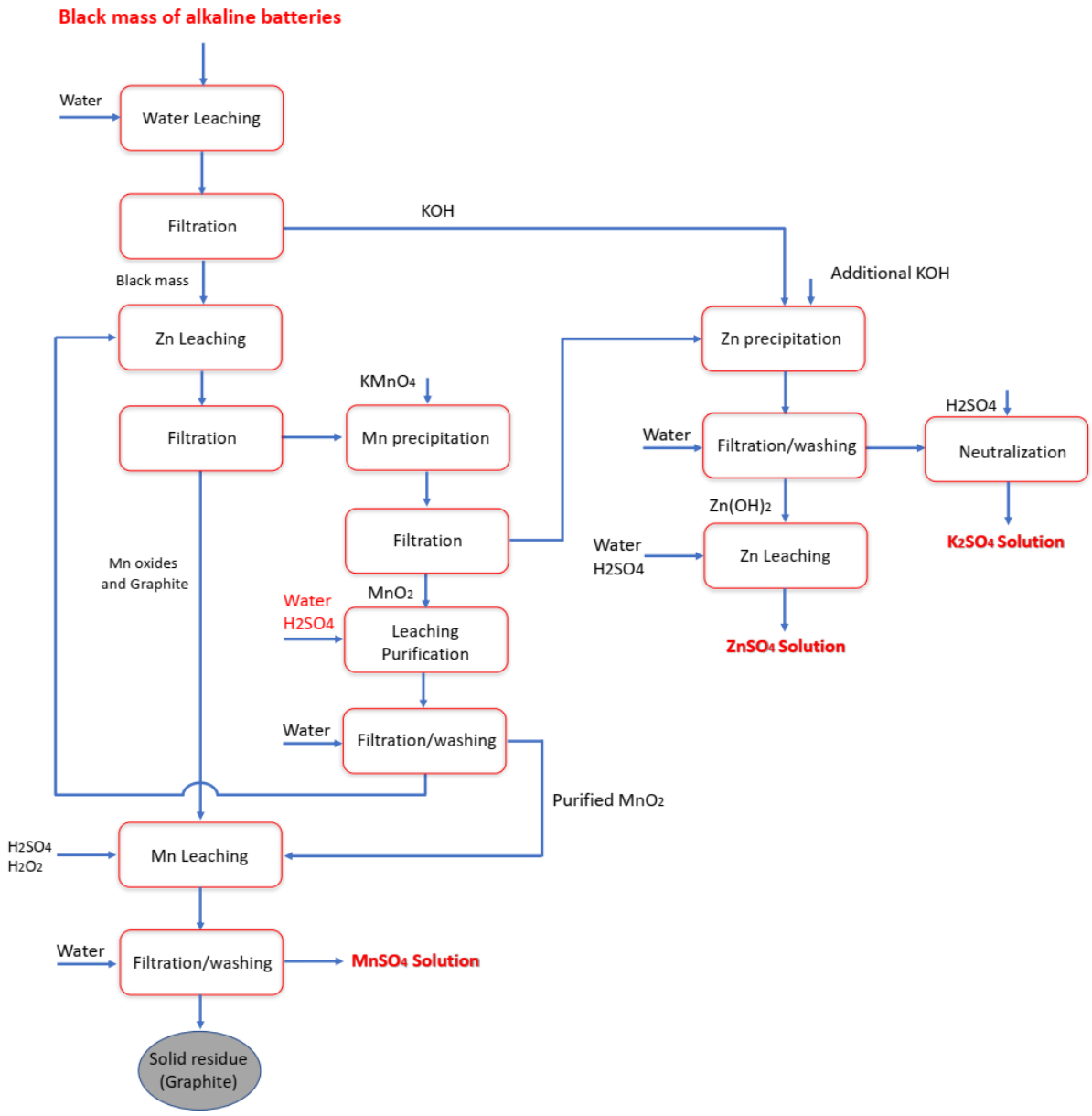

Fig. 2 The modified process for the treatment of alkaline spent batteries to recover K_2SO_4, $ZnSO_4$, and $MnSO_4$ solutions.

3.3.2.1 Zn selective leaching

Some experiments were performed to reduce acid concentration in this stage. First the black mass was washed with water for 1 hour at room temperature with a pulp density of 20%, to remove KOH (in section 3.1.2). Then the effect of sulfuric acid concentration and leaching time was evaluated on the leaching efficiency of Zn.

Table 2 shows the leaching conditions. It should be noted that according to the previous study, about 10% weight loss occurred after water leaching and drying. Accordingly, the initial solid

weight was selected 10% more (before water leaching) to have around 20% pulp density in the Zn leaching stage.

Table 14. Leaching conditions for Zn leaching optimization (effect of sulfuric acid concentration)

Test	m (g)	H_2SO_4 (M)	H_2SO_4 (%V/V)	T (°C)	t (h)	V final (ml)	pH final	m final (g)	Weight loss (%)
1	11.019	1	5.6	25	1	49	3.24	5.914	46.32
2	11.02	1.5	8.3	25	1	66	1.4	5.187	52.93
3	11.062	1.65	9.2	25	1	64	1.2	5.202	52.97

As can be seen, the effect of sulfuric acid concentration has been evaluated. The weight loss results showed that a 1.5 M solution of sulfuric acid (equal to 8.3% v/v) is enough to have suitable leaching efficiency (test 2).

In the next step the effect of leaching time (30-60 min) and lower values of sulfuric acid (7-8% v/v) is investigated. Table 3 shows the leaching conditions. As can be seen, the best result is obtained in test 6 with 8% v/v sulfuric acid in 1 hour of leaching time.

Accordingly, a higher mass of BM washed in 500 ml of water to remove KOH (final volume of 480 ml with pH of 10). Then the filter cake was leached in the optimized condition for the next steps (the last row in the Table 15). Table 16 demonstrates the leaching results of the above experiments (Table 14-15).

Table 15. Leaching conditions for Zn leaching optimization (effect of leaching time)

Test	m (g)	H_2SO_4 (M)	H_2SO_4 (%V/V)	T (°C)	t (h)	V final (ml)	pH final	m final (g)	Weigh t loss (%)
4	2.205	1.26	7	25	1	17	1.98	1.089	50.61
5	2.202	1.26	7	25	0.5	19.5	1.85	1.122	49.04
6	2.204	1.44	8	25	1	21	1.6	1.04	52.81
7	2.203	1.44	8	25	0.5	19	1.55	1.099	50.11

Optimized test at high volume	110.128	1.44	8	25	1	607	1.35	53.361	51.55

Table 16. Leaching results for Zn leaching optimization (experiments in Table 14-15)

Test	**H_2SO_4 (M)**	**H_2SO_4 (%V/V)**	**t (h)**	**V final (ml)**	**Concentration (mg/l)**			**Leaching efficiency (%)**		
					Mn	**Zn**	**K**	**Mn**	**Zn**	**K**
1	1	5.6	1	49	15548	40298	4528	22.62	79.02	41.82
2	1.5	8.3	1	66	16730	34848	3030	32.78	92.03	37.70
3	1.65	9.2	1	64	16942	36081	3004	32.06	92.05	36.11
4	1.26	7	1	17	11410	24855	2417	28.78	84.50	38.71
5	1.26	7	0.5	19.5	9524	23089	2183	27.59	90.17	40.16
6	1.44	8	1	21	9867	22605	1974	30.76	94.98	39.07
7	1.44	8	0.5	19	10018	23584	2158	28.26	89.70	38.67
Optimized test at high volume	1.44	8	1	607	19789	40075	4816	35.68	97.40	55.14
KOH solution (water leaching)	-	-	1	480	0.63	0.78	5917	0	0	53.57

Table 16 shows that about half of the potassium is removed by water leaching (last row in the Table). As can be seen about 35% of Mn, 97% of Zn, and the remaining value of K (55%) is leached after selective leaching of Zn in the final optimized test in high volume. According to the results the recovery efficiency of K is more than 100% after two steps of leaching, which is obviously due to the error in the calibration of ICP and measurement of K in the solutions.

3.3.2.2 Mn precipitation

The obtained solution after Zn leaching and filtration was subjected to Mn precipitation by $KMnO_4$. Different values of $KMnO_4$, according to the stoichiometric value, were added to the solution at 70 °C for 30 minutes. It is better to use high temperatures as high as 70 °C to prevent agglomeration of $KMnO_4$ during addition, and to have a complete reaction. Table 5 shows the results.

Table 17. Mn precipitation experiments

Test	$KMnO_4$ (mg)	Respect to stoi. value	V initial (ml)	V final (ml)	Concentration (mg/l)		Precipitation value (%)	
					Mn	Zn	Mn	Zn
Initial Solution	0	0	10	10	18238	39648	0	0
Mn prec. 1	250	0.66	10	24	2055	16863	72.94	0
Mn prec. 2	300	0.80	10	29	820	13642	86.94	0.21
Mn prec. 3	360	0.95	10	27.5	0.59	12242	99.99	15.08
Mn prec. 4	400	1.05	10	27	0.4	13147	99.99	10.46

Considering the results in Table 17, the remaining volume of the solution (542 ml) was subjected to Mn precipitation according to precipitation test 3 (Table 17) by adding 19.5 g of $KMnO_4$ and mixing for 30 minutes at 70 °C. Final slurry was filtered and washed. The results are presented in Table 18.

Table 18. Mn precipitation of the total solution

Test	$KMnO_4$ (g)	Respect to stoi. value	V initial (ml)	V final (ml)	Mass of precipitated MnO_2	Concentration (mg/l)		Precipitation value (%)	
						Mn	Zn	Mn	Zn
Total solution	19.512	0.95	542	654	34.522	8.64	30635	99.94	6.76

As can be seen about 6.76% of the Zn is co-precipitated with MnO_2, which needs to be removed in order to achieve pure manganese sulfate solution at the end of process. Therefore, some purification tests were performed in the following section.

3.3.2.2.1 Purification of MnO_2

The purification experiments were performed at different sulfuric acid concentrations, at 50 °C for 2 hours. The results are shown in Table 19.

Table 19. MnO_2 purification tests

Test	Mass of MnO_2 (g)	H2SO4 (%v/v)	T (°C)	t (h)	V_i (ml)	V_f (ml)	Concentration (mg/l)			Dissolution value (%)		
							Mn	Zn	K	Mn	Zn	K
1	0.575	0.42	50	2	10	25	0.91	308.4	210	0	31.82	-
2	0.575	5	50	2	10	27	7.78	733.2	250	0	81.71	-
3	0.575	10	50	2	10	28	32.28	948.2	300	0	100	-

According to Table 19 it is possible to dissolved co-precipitated Zn from MnO_2, but the dissolution efficiency depends on the acid concentration. So, the total amount of MnO_2 was leached according to the conditions like the test 3 of the above table. The results are presented in Table 20.

Table 20. Purification of total MnO_2

Test	Mass of MnO_2 (g)	H2SO4 (%v/v)	T (°C)	t (h)	V initial (ml)	V final (ml)	m final (g)	Concentration (mg/l)			Dissolution value (%)		
								Mn	Zn	K	Mn	Zn	K
1	34.43	10	50	2	150	343	31.57	106	3934	283	0	92.88	-

The results show that most of co-precipitated Zn can be recovered in this way. Therefore, it is suggested that this solution goes for the initial Zn leaching using a counter current stream, which has been considered in the block diagram (Fig. 2).

3.3.2.3 Zn precipitation

The recovered solution after Mn precipitation (Table 18) was subjected to Zn precipitation. The initial washing water solution (480 ml) which contains KOH, and additional KOH (using a 5M solution) was added to the solution to increase pH to around 8.5. All the Zn was precipitated at this pH value. The results are shown in Table 21.

Table 20. Zn precipitation conditions and results

V initial solution (ml)	V initial wash water solution (ml)	Mass of additional KOH (5M) (g)	pH final	pH after washing and filtration	V final (ml)	Concentration (mg/l)			Precipitation value (%)		
						Mn	Zn	K	Mn	Zn	K
641	480	59.24	8.5	7	1067	0.97	15	33546	-	99.76	-

In the above experiment the filtration efficiency was not good, due to the high volume of Zn precipitates. Therefore, a small value of precipitate (which contains 3 g zinc) was dissolved in a sulfuric acid solution to measure potassium content in the precipitate. The results are shown ion Table 10.

Table 21. Initial test of Zn (OH)2 dissolution

Initial Zn content in the precipitate (g)	V Water (ml)	V H_2SO_4 (ml)	V Final (ml)	Concentration (mg/l)			mass (mg)		
				Mn	Zn	K	Mn	Zn	K
3	30	2.5	67	6.87	44691	10570	0.46	2995	708

As can be seen in Table 21, the final volume of the solution is almost twice the initial volume of the solution, which means high volume of solution (rich in potassium) is remained in the precipitates due to not efficient filtration which leads to bring potassium as impurity to the precipitates. Table 21 shows that about 708 mg of K exist per each 3 g of Zn in the precipitates. Therefore, a water leaching stage is needed for purification of Zn $(OH)_2$.

3.3.2.3.1 Purification of Zn $(OH)_2$ and dissolving in sulfuric acid

Zinc precipitates were washed in 300 ml of water for 1 hour. Afterwards, the slurry was filtered, and the solution was analyzed for determining metal content. Finally, the washed Zn $(OH)_2$ was dissolved in sulfuric acid solution. Results are presented in Table 22.

Table 22. Purification of Zn (OH)2 precipitates, and dissolving in sulfuric acid

	V Water (ml)	V H_2SO_4 (ml)	V Final (ml)	Concentration (mg/l)			mass (mg)		
				Mn	Zn	K	Mn	Zn	K
Solution after washing Zn $(OH)_2$	300	0	745	2.22	160	9445	1.6	119	7038
Zn $(OH)_2$ dissolution in H_2SO_4	50	18	128	20.44	125271	4465	2.6	16034	571

Table 22 shows that the solution after washing Zn $(OH)_2$ contains 9.5 g/l of potassium and very low amounts of Mn and Zn. Accordingly, this solution was mixed with the solution after precipitation of Zn $(OH)_2$ (Table 20).

3.3.2.4 Mn reductive leaching

Solid residue after Zn leaching (Table 16) and precipitated MnO_2 after purification (Table 19), were mixed to prepare the solid for reductive leaching experiments.

The above mixture was leached at different conditions to optimize H_2SO_4 and H_2O_2 values. All experiments were carried out at a pulp density of 20%, room temperature, and 1 hour of reaction time. All solid residues were dissolved in aqua regia to determine the remaining values of metals in the solid and calculating leaching efficiency. Table 23 illustrates the leaching results in a fixed value of H_2SO_4 and different values of H_2O_2.

Table 23. Reductive leaching results in a fixed value of H2SO4 and different values of H_2O_2.

Test	m (g)	V (ml)	H_2SO_4 (%v/v)	H_2O_2 (%v/v)	V final (ml)	Leaching Efficiency (%)		
						Mn	Zn	K
1	2.003	10	20	10	39	60.37	88.64	63.66
2	2	10	20	15	41	89.49	92.56	91.85
3	2.001	10	20	20	52.5	99.93	92.24	98.89
4	2.003	10	20	25	49	99.91	99.52	99.03
Chemical Attack results								
						Mass (mg)		

Test	V final (ml)	Mn	Zn	K
Solid residue of test 1	50	398	5	8
Solid residue of test 2	50	102	2	1.86
Solid residue of test 3	50	0.637	2	0.258
Solid residue of test 4	50	0.868	0.14	0.236

According to the results of Table 23, 20%v/v of H_2O_2 is sufficient to dissolve all Mn in 1 hour. So, this value is considered constant for the next experiments of optimization of H_2SO_4 value.

All solid residues were dissolved in aqua regia to determine the remaining values of metals in the solid and calculating leaching efficiency. Table 24 demonstrates the leaching results in a fixed value of H_2O_2 (20%v/v) and different values of H_2SO_4.

Table 24. Reductive leaching results in a fixed value of H2O2 and different values of H_2SO_4.

Test	m (g)	V (ml)	H_2SO_4 (%v/v)	H_2O_2 (%v/v)	V final (ml)	Leaching Efficiency (%)		
						Mn	Zn	K
5	2	10	10	20	40	90.85	72.19	93
6	2.003	10	15	20	48	99.90	99.31	99.10
7 (Repetition of test 3)	2.005	10	20	20	50	99.95	99.52	99.22

Chemical attack results				
		Mass (mg)		
Test	V final (ml)	Mn	Zn	K
Solid residue of test 5	50	88	5	1.401
Solid residue of test 6	50	0.859	0.17	0.213
Solid residue of test 7	50	0.485	0.124	0.1865

Results show that 15%v/v of H_2SO_4 is necessary for complete dissolution of Mn in 1 hour. Therefore, the optimum values of H_2SO_4 and H_2O_2 were determined as 15%v/v and 20%v/v,

respectively. Therefore, total solid was dissolved at these conditions and results are presented in Table 25. Finally, 2 samples of the solid residue was dissolved in aqua regia to determine the remaining metals in the graphite (Table 25).

Table 25. Reductive leaching results of Mn at the optimum conditions of H_2O_2 and H_2SO_4.

m (g)	V (ml)	H_2SO_4 (%v/v)	H_2O_2 (%v/v)	V final (ml)	m final (g)	Leaching Efficiency (%)		
						Mn	Zn	K
70.835	355	15	20	762	5.19	99.98	99.63	99.35
Chemical attack results								
						Mass (mg)		
	Repetition			m (g)	V final (ml)	Mn	Zn	K
	1			0.198	50	0.279	0.1215	0.227
	2			0.116	50	0.148	0.0735	0.142

Finally, three solutions of K_2SO_4, $ZnSO_4$, and $MnSO_4$ were analyzed to determine metals concentrations. It should be noted that the volume of $ZnSO_4$ solution was increased to 200 ml before analysis. Table 26 illustrates the chemical composition of the three solutions.

Table 26. Chemical composition of final sulfate solutions

Solution	V (ml)	Conc. (g/l)			Percentage in the solution (%)		
		Mn	Zn	K	Mn	Zn	K
K_2SO_4	1800	0.001	0.062	22.41	0.006	0.28	99.72
$ZnSO_4$	200	0.009	74.31	2.095	0.012	97.25	2.74
$MnSO_4$	762	47.82	1.14	1.19	95.35	2.28	2.37

3.4 Mass balance

According to the results obtained in this study, a rough mass balance was performed to treat 1000 kg of the black mass. The results are reported in Table 27.

Table 27. Mass balance for treating 1000 kg of black mass

Reagents	Amount (ton)	Products	Amount (ton)
Black Mass	1	**$K_2SO_4.H_2O$**	1.23
H_2SO_4 (95%)	2.290	**$ZnSO_4.7H_2O$**	1.06
$KMnO_4$ (99.5%)	0.23	**$MnSO_4.H_2O$**	1.26
KOH (100%)	0.57		
H_2O_2 (30%)	1.070		
Water	16.33		

3.5 Process simulation

Process simulation was performed with HSC sim software, according to the data obtained in this study. Fig. 3 illustrates the PFD of the simulated process. The composition of output streams is reported in Table 28.

Table 28. Simulated results for the composition of output streams for treating 1000 kg of black mass

Stream	Mass (ton)	Volume (m^3)	Density (kg/m^3)	pH	K (g/l)	Zn (g/l)	Mn (g/l)
K_2SO_4 solution	11.9	11.07	1073.93	7	45.19	0	0
$ZnSO_4$ solution	2.97	2.41	1233.41	7.01	0.23	100	0
$MnSO_4$ solution	6.51	4.69	1334.49	-0.38	1.92	1.37	88.22
Solid residue (graphite)	0.069	0.04	1724.89	1.14	0.06	0.04	2.69

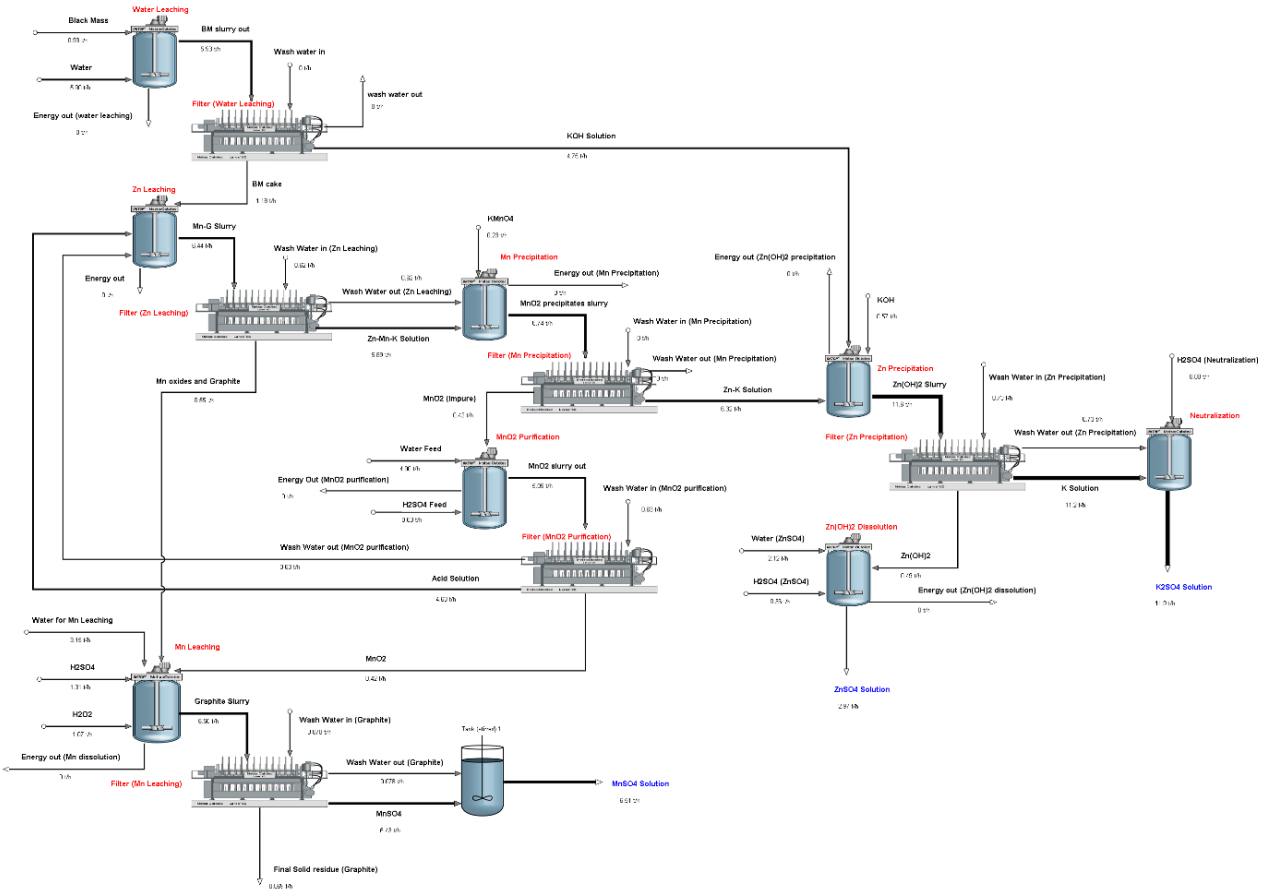

Fig. 3 Process flow diagram of the simulated process

3.6 Conclusions and Suggestions

This study shows a comparative analysis with technical feasibility of two processes for the recovery of elements in the form of nitrates and sulphates from the alkaline spent batteries, and understanding of parameters which are useful for high purity yield with minimal chemical composition. Some important findings and suggestions are as follows:

- The nitrate route can be chosen when the yield is needed to have maximum stability and direct generation of oxides through cleaner thermal decomposition. This could also be a good choice to get nitrate precursors for the applications in advanced materials supply, for example, catalysts, ceramics, or nano oxides.
- The sulphate route is chosen when high-purity manganese sulfate ($MnSO_4$) is needed for the fertilizer market or battery-grade materials. It also benefits in reducing the gas formation during the hydrometallurgical process.

- Purity of $ZnSO_4$ solution was observed to be limited due to co-precipitation and can be improved by an enhanced filtration-washing process to remove potassium from $Zn(OH)_2$ precipitate.
- Purity of $MnSO_4$ solution can be improved if the initial leaching is performed at higher temperatures to remove zinc and potassium more effectively, as it improves the dissolution kinetics of manganese, and a cleaner Mn^{+2} solution, which can crystallize to high-purity, fertilizer or battery grade manganese sulphate.
- There is also a possibility of decreasing H_2SO_4 and H_2O_2 consumption in the reductive leaching of manganese by increasing leaching time and using higher temperatures. This step could be more aligned with sustainable chemical engineering principles, with minimum reagent consumption and no effect on the recovery yield.

The future perspective of this study could be a circular economy while recovering useful elements from the hazardous battery waste, along with environmental sustainability while lowering the battery waste and minimizing chemical consumption, and a global push towards the greener materials supply chain.

CHAPTER 4

A Study on Selective Separation of Elements from Ground Cathode-Anode Mixtures of End-of-Life Li-ion Batteries (NMC-Type)

4.1 Introduction

The increasing use of lithium-ion batteries (LIBs) in portable devices, electric vehicles, and renewable energy storage systems has led to significant environmental and resource challenges[71], [72]. Moreover, disposing of spent LIBs generates not only hazardous waste but also contains valuable metals such as copper, iron, aluminum, manganese, cobalt, nickel, and lithium[73]. As a result, recycling the spent LIBs and recovering these valuable metals can help to lessen the environmental impacts and reduce reliance on mining, which depletes natural resources and causes ecological harm[74], [75]. Due to the limited availability of precious metals such as Co and Li, there is a high demand for recovering these metals[76], [77]. This approach supports the global circular economy efforts and provides economic benefits.

The first step in recycling spend LIBs involves collecting, sorting, and dismantling, followed by specialized processes tailored to specific battery types[78]. For instance, lead-acid batteries are processed through pyrometallurgy, while other batteries utilize hydrometallurgical techniques and hybrid methods[79]. In hydrometallurgical processes, batteries are crushed and subjected to leaching using organic or mineral acids or bioleaching. Metals are then separated through solvent extraction, precipitation, or electrochemical methods [80].

However, previous studies indicate that metals from LIBs can be recovered using various methods, including pyrometallurgy, hydrometallurgy, and direct recycling[81], [82]. However, these approaches frequently result in incomplete recovery and inefficient resource utilization. Pyrometallurgy extracts metals at high temperatures, leading to substantial energy consumption, air pollution, and lithium loss[83]. In contrast, hydrometallurgy combines chemical or bioleaching with solvent extraction or precipitation to achieve high selectivity and efficiency at lower temperatures[84]. However, its reliance on acid leaching presents environmental risks and often results in low lithium recovery rates. Along with this method, direct recycling simplifies the material recovery process and enhances recovery rates[85]; while, it encounters strict regulatory challenges that limit its commercial viability.

To address these issues, researchers are exploring the combination of hydrometallurgical and pyrometallurgical techniques[86]. For instance, pairing leaching with high-temperature

pretreatment can improve recovery rates while also reducing the usage of chemicals and energy. Liu et al.[79] proposed a mild recovery process that integrates both hydrometallurgy and pyrometallurgy to extract valuable materials from spent lithium-ion batteries (LIBs), resulting in lower energy consumption and reduced use of chemical reagents.

Recently, numerous methods for extracting precious metals from spent LIBs have been developed. Among them, solvent extraction is frequently employed due to its exceptional efficacy, capability to yield high-purity products, and cost-effectiveness relative to conventional separation techniques[87]. A number of studies have been carried out to develop an efficient solvent extraction method for the separation of Co, Ni, and Li utilizing Cyanex 272 (bis(2,4,4-trimethylpentyl) phosphinic acid), D2EHPA (di-(2-ethylhexyl) phosphoric acid), and 2-ethylhexyl phosphonic acid mono-2-ethylhexyl ester (PC-88A) as extractants[88]. Most of the process used D2EHPA or Cyanex 272 as extractants to separate Mn, Ni and Co from the pregnant leach solution (PLS), which contained a high concentration of Co, Ni, Mn, Li and a low concentration of Cu, Al, and Fe. Among separation processes, Mn as a critical metal can be efficiently separated using D2EHPA, a method extensively studied by researchers due to the rising global demand driven by the expanding market for lithium-ion batteries[89].

The current study focuses on the efficient recovery of these critical metals, particularly Mn, with minimal loss of metals with relatively high-purity output from a ground mixture of cathode and anodes of spent LiBs. This study investigates the leaching of cathode active material derived from NMC (Nickel Manganese Cobalt) batteries; a category of LIBs batteries utilized in vehicles. The subsequent phase will involve the formulation of an innovative strategy for the separation of Co, Ni, Mn, and Li from the PLS through a combination of precipitation (PPT) and solvent extraction (SX) aimed at reducing the loss of battery metals and eliminating impurities in the final products. It starts with Cu recovery through cementation, followed by Fe and Al precipitation using NaOH. Mn is extracted with D2EHPA diluted in n-heptane with pH optimization. Co and Ni are separated using Cyanex 272, leaving Li in the solution for further recovery.

The novelties introduced in the literature through this study are several and of strategic relevance. Although many articles analyze different leaching systems of the considered metals, the number of articles that study an integrated process (leaching and subsequent recovery) is minimal. Furthermore, articles that analyze and optimize integrated processes very often refer to a particular component of the batteries (anode or cathode materials). These aspects greatly

limit the potential of any recovery processes on an industrial scale as it would imply the need to introduce a double treatment line, each for the recycling of one of the materials of the exhausted batteries. The process proposed in this work allows the treatment of a mix of anodic and cathodic material and selectively recovers all the metals of interest by combining different operations, such as cementation and solvent extraction. This research seeks to improve scalability and sustainability in LIB recycling thanks to all these aspects.

The study contributes to LIB recycling and resource recovery by improving multi-step processes and combining techniques to address technical and environmental challenges. It aims to balance efficiency, cost, and ecological impact while advancing sustainable recycling practices for LIBs and other materials. The samples for conducting this research were provided by the COBAT industry.

4.2 Materials and Methods

4.2.1 Materials

The ground battery mixture of the NMC batteries was obtained from automotive waste. In order to remove most of aluminum and copper foils and achieve a more concentrated black mass the ground mixture was subjected to sieving. Following the sieving process, a sample with a sieve size of less than 250 μm was selected as the starting materials for our investigations. This sample, along with the initial ground mixture, was analyzed by dissolving it in aqua regia and performing ICP analysis (ICP-OES; Agilent Technologies 5100). Table 1 presents the chemical composition of the sample. Mass balance calculations indicated that approximately 60% of the cathode active material was recovered through the simple sieving step, with about 30% aluminum and less than 10% of the total copper present as impurities.

Analytical-grade sulfuric acid and hydrogen peroxide (VWR Chemicals) were employed for acid-leaching. Iron powder from CARLO ERBA reagent, and sodium hydroxide from VWR Chemicals were used in cementation and precipitation experiments, respectively.

In the context of solvent extraction, di-(2-ethylhexyl) phosphoric acid (D2EHPA) was sourced from PanReac AppliChem, while bis(2,4,4-trimethylpentyl) phosphinic acid (Cyanex272) was obtained from Cytec. The diluent, 99% n-Heptane was supplied from PanReac AppliChem.

Table 1. Chemical composition corresponding to the obtained cathode active material after sieving.

Element	Li	Co	Ni	Mn	Cu	Al
Weight percentage (%)	3.20	7.10	8.63	7.15	1.57	2.16

4.2.2 Leaching

Sulfuric acid was chosen as the lixiviant due to its ability to achieve relatively high metal recovery yields and its economic potential for extracting valuable metals. The sieved powder was leached using a 1M sulfuric acid solution containing 10% (v/v) H_2O_2 (using a 30% solution), with a pulp density of 50 g/L, at 250 rpm in a borosilicate glass reactor at room temperature for 2 hours. After leaching, the slurry was filtered through a vacuum filter with a pore size of 0.45 µm. The leaching efficiency was assessed by analyzing the metal concentrations in the filtrate via ICP, following appropriate dilution with an acidic solution.

4.2.3 Cementation

Cementation experiments were performed for the Cu extraction using the Iron powder. All the experiments were performed at room temperature for 1 hour and continuous stirring at 250 rpm. The amount of iron powder was estimated through stochiometric calculations.

4.2.4 Precipitation

Iron and aluminum precipitation experiments were conducted in a borosilicate glass reactor at room temperature for 1 hour. The pH was incrementally increased utilizing a 10% NaOH solution.

4.2.5 Solvent Extraction

In this study, D2EHPA was utilized for selective manganese separation, while Cyanex 272 was used to separate cobalt from nickel and lithium. The pH adjustment of the pregnant leach solution (PLS) was conducted by adding NaOH solution. The organic phases at two different stages of extraction comprised an extractant solution containing D2EHPA and Cyanex 272. To address the high viscosity, n-heptane (99.9%) was added to lower the organic phase's viscosity and density. The extractant to dilutant ratio of 20:80, and the O/A ratio of 1:1 were kept constant for all the extraction experiments. The organic phases were subsequently stripped with sulfuric acid solution, and all extraction and stripping experiments were conducted at room temperature for 10 minutes.

The pH isotherms were established by combining the organic-aqueous dispersion (phase ratio O/A = 1:1) in a container until the mixture reached equilibrium (constant pH value). A NaOH

solution was used to adjust the equilibrium pH during the extraction process, followed by the sampling of the aqueous phase at each test.

Saponification experiments were conducted by adding varying amounts of NaOH (as a 30% solution) to the organic phase and mixing for 10 minutes at room temperature. Additionally, the effects of acid concentration and the O/A ratio on Mn stripping during the stripping stage of D2EHPA were investigated.

4.3 Results and discussion

4.3.1 Characterization of the Initial Sample

The sample received was characterized and the results are presented in four main sections. First, the sample was analyzed by sieving using standard sieve series to determine particle size distribution of the as-received sample. Then, the LOI of different fractions were determined by heating the samples at 600 °C for 1 hour. XRF investigations were performed on the different size fractions before and after heat treatment and the results are presented in the third section. Chemical composition of the samples was also analyzed by chemical attack treatment and ICP measurement in the fourth section.

4.3.2 Size distribution

The quartering method was applied to 30 kg of the as received samples to obtain 2.5 kg of sample for experimental analysis. A visual representation of the received sample is presented in Fig. 1.

Fig. 1 A view of the as-received sample.

The 2.5 kg sample was sieved using a 5600 mm sieve size. The ASTM sieves are used for granulometric classification. About 2201.5g or 88.06% of the sample remained above the sieve, and 298.5g or 11.94 % passed through the sieve (Fig. 2). This 298.5 g sample was separated into different particle sizes using various sieves. The resulting particle size distribution is shown in Table 2.

Fig. 2 A view of the mass above and under the sieve 5600 mm.

Size µm	Weight (g)	Wt. %	Cumulative (%)
< 125	2.37	0.09	0.09
125 - 500	100.37	4.01	4.11
500 - 1000	49.47	1.98	6.09
1000 - 2000	51.02	2.04	8.13
2000 - 5600	95.22	3.81	11.94
> 5600	2201.55	88.06	100.00

Table 2. The results of the sieve analysis of 2500 g of the as-received sample

Regarding the above results, most of the particles (88% by weight) are above 5.6 mm. According to the visual evaluation, it mainly consists of membrane separators, aluminum and copper foils with the cathode active material and graphite attached to their surfaces (Fig. 4).

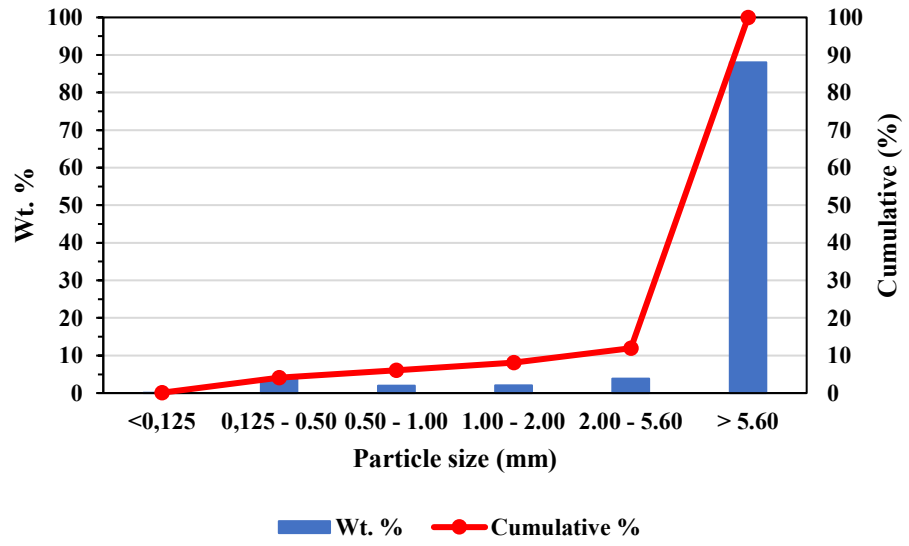

Fig. 4 Particle size distribution of the as-received sample.

Different fractions were analyzed in more detail by thermal treatment, XRF and chemical attack, to determine the composition of each fraction. The results are represented in the following sections.

4.3.3 Loss on Ignition (LOI)

In this section LOI was measured for the samples before and after water washing, which was performed to remove the electrolyte. Different size fractions were heated at 600 °C for 1 hour in a muffle furnace to determine loss on ignition. The weight of samples subjected in the furnace was carefully noted before and after the ignition to measure the weight loss.

4.3.3.1 Loss on Ignition without washing

Table 3 shows the weight loss and LOI results for the different size fractions without washing. The samples were heated at 600°C for one hour.

Table 3. The results of LOI for different size fractions without washing (heating at 600 °C for 1 hour)

Size (mm)	Name	Initial weight (g)	Final weight (g)	Weight loss (g)	Loss on Ignition (%)
d < 125	A	2.1	0.96	1.13	54.10
125 < d < 500	B	5.01	1.45	3.56	71.05
500 < d < 1000	C	5.01	2.94	2.07	41.30
1000 < d < 2000	D	5.06	2.88	2.18	43.08

2000 < d < 5600	E	5.00	3.60	1.41	28.14
> 5600	F	5.00	3.83	1.17	23.40
Initial sample (as received)	G	5.00	3.26	1.74	34.80

4.3.3.2 Loss on Ignition after washing

In this section, different size fractions were washed with water before thermal treatment. Table 4 shows the weight loss results after washing followed by drying at 110 °C for 24 hours. Table 5 represents the weight loss and LOI results for the different size fractions of the dried samples after thermal treatment at 600 °C for 1 hour.

Table 4. Weight loss results for different size fractions after washing and followed by drying at 110 °C for 24 hours

Size (mm)	Name	Initial weight (g)	Final weight (g)	Weight loss (g)	Weight loss (%)
d < 125	A	0.897	0.862	0.035	3.91
125 < d < 500	B	5.377	5.221	0.157	2.90
500 < d < 1000	C	4.033	3.918	0.115	2.85
1000 < d < 2000	D	5.641	5.483	0.158	2.80
2000 < d < 5600	E	7.322	6.507	0.815	11.13
> 5600	F	8.993	7.369	1.624	18.05
Initial sample (as received)	G	8.429	5.431	2.998	35.56

Table 5. The results of LOI for the dried samples of different size fractions after water washing (heating at 600 °C for 1 hour)

Size (mm)	Name	Initial weight (g)	Final weight (g)	Weight loss (g)	Loss on Ignition (%)
d < 125	A	0.862	0.240	0.586	67.98
125 < d < 500	B	5.221	1.673	3.541	67.95
500 < d < 1000	C	3.918	2.230	1.688	43.08
1000 < d < 2000	D	5.483	2.911	2.572	46.90
2000 < d < 5600	E	6.507	3.375	3.132	48.13
> 5600	F	7.369	3.551	3.818	51.81

Initial sample (as received)	G	5.431	3.291	2.140	39.41

4.3.4 XRF Analysis

XRF analysis was performed for different size fractions, without washing, before and after thermal treatment to determine the elemental percentage associated with each particle size class. It should be noted that for the larger fraction sizes the samples were milled manually before XRF analysis to obtain a semi-homogeneous sample for the analysis.

4.3.4.1 XRF analysis before thermal treatment

Table 6 illustrates the XRF results for different size fractions, without washing, before thermal treatment. The main elements detected in XRF analysis are Co, Ni, and Mn, which belong to the cathode active material. It is well known that Cu and Al are anode and cathode collectors, respectively.

Table 6. XRF results for different size fractions before thermal treatment

Size (mm)	Fe (%)	Co (%)	Ni (%)	Cu (%)	Al (%)	Mn (%)
d < 125	0.094	0.761	2.546	1.712	0.002	0.951
125 < d < 500	0.071	0.698	2.454	2.255	0.002	0.845
500 < d < 1000	0.020	0.608	2.584	6.001	0.002	1.002
1000 < d < 2000	0.010	0.635	2.857	8.125	0.002	1.111
2000 < d < 5600	0.688	0.807	3.065	2.928	0.002	1.381
> 5600	0.018	2.651	9.255	0.374	0.002	1.106

As can be seen, the distribution of Ni, Co, and Mn are somehow the same in the fraction sizes below 5600 mm, which means a similar distribution of cathode active materials in all fraction sizes below 5600 mm. The copper content, on the other hand, is increased by increasing sieve sizes up to 2000 mm which demonstrate the higher value of anode collectors in these size fractions. Nickel and cobalt content are increased for the size fractions above 2000 mm which means most of the cathode active material presents in higher size fractions more than 5600 mm, attached to the large aluminum foils.

The metal content of each size fraction and chemical composition of the 2500 g sample was calculated according to the data in Table 6 and the results are shown in Table 7. As can be seen, the as-received sample contains 2.42% Co, 8.48% Ni, 1.10% Mn, and 0.82% Cu which is lower

than the expected value of Cu in lithium batteries. It should be mentioned that XRF is a semi-quantitative analysis method which is not able to determine the accurate metal contents, especially for the light elements.

Table 7. Metal content of each size fraction and chemical composition of the sample

Size (mm)	Fe (g)	Co (g)	Ni (g)	Cu (g)	Al (g)	Mn (g)
d < 125	0.0022	0.0180	0.0603	0.0406	0.0001	0.0225
125 < d < 500	0.0713	0.7006	2.4631	2.2633	0.0020	0.8481
500 < d < 1000	0.01	0.3008	1.2783	2.9687	0.001	0.4957
1000 < d < 2000	0.005	0.324	1.4576	4.1454	0.0010	0.5668
2000 < d < 5600	0.6551	0.7684	2.9185	2.7880	0.002	1.315
> 5600	0.3963	58.3631	203.7534	8.2338	0.0440	24.3491
Sum	1.1399	60.4749	211.9313	20.4398	0.05	27.5973
Chemical composition of the sample (%)	0.0456	2.419	8.4772	0.8176	0.002	1.1039

Considering the XRF results (Table 6 and Table 7), it is possible to calculate metal distribution in each size fraction. Table 8 and Fig. 5 illustrate metal distribution for different size fractions. Fig. 6 shows that almost all cathode active material (Co, Ni, and Mn) is distributed above 5600 mm, and Cu is distributed in all size fractions, but more than half above 2000 mm.

Table 8. Metal distribution for different size fractions

Size (mm)	Fe (%)	Co (%)	Ni (%)	Cu (%)	Al (%)	Mn (%)
d < 125	0.20	0.03	0.03	0.20	0.09	0.08
125 < d < 500	6.25	1.16	1.16	11.07	4.01	3.07
500 < d < 1000	0.87	0.50	0.60	14.52	1.98	1.80
1000 < d < 2000	0.45	0.54	0.69	20.28	2.04	2.05
2000 < d < 5600	57.47	1.27	1.38	13.64	3.81	4.76
> 5600	34.77	96.51	96.14	40.28	88.06	88.23
Sum	100	100	100	100	100	100

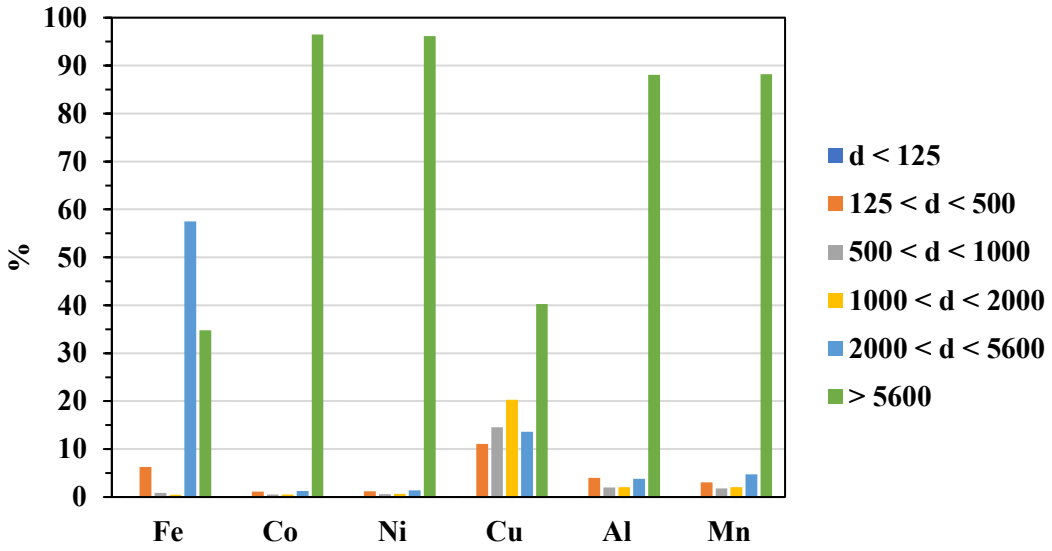

Fig. 5 Graphical representation of metal distribution in different size fractions.

4.3.4.2 XRF analysis after thermal treatment

Table 9 illustrates the XRF results for different size fractions, without washing, after thermal treatment at 600 °C for 1 hour.

Table 9. XRF results for different size fractions after thermal treatment

Size (mm)	Fe (%)	Co (%)	Ni (%)	Cu (%)	Al (%)	Mn (%)
d < 125	0.4382	1.972	8.052	5.499	0.002	2.975
125 < d < 500	0.102	1.415	6.006	6.931	0.002	2.361
500 < d < 1000	0.0767	1.037	4.307	9.867	0.002	1.715
1000 < d < 2000	0.0571	0.7724	3.516	11.97	1.532	1.428
2000 < d < 5600	0.0096	0.8577	2.693	0.9643	0.002	1.272
> 5600	0.1697	2.631	10.32	2.827	0.002	4.44

As can be seen, the content of Ni, Co, and Mn has increased due to the weight loss after thermal treatment. Table 9 shows that there is no meaningful trend in these results. It seems there is an error for Al for the fraction size of 1000-2000 mm, which is very high in comparison with the other fraction sizes and the XRF results before thermal treatment.

The metal content of each size fraction was calculated according to the data in Table 9, and the results are shown in Table 10. As stated before, XRF is a semi-quantitative analysis method that cannot determine the accurate metal contents. So, it is necessary to do a chemical attack to determine metal contents accurately.

Table 10. Metal content of each size fraction after thermal treatment

Size (mm)	Fe (g)	Co (g)	Ni (g)	Cu (g)	Al (g)	Mn (g)
d < 125	0.0104	0.0467	0.1908	0.1303	0	0.0705
125 < d < 500	0.1024	1.4202	6.0282	6.9566	0.0020	2.3697
500 < d < 1000	0.0379	0.5130	2.1307	4.8812	0.001	0.8484
1000 < d < 2000	0.0291	0.3941	1.7939	6.1071	0.7816	0.7285
2000 < d < 5600	0.0091	0.8167	2.5642	0.9182	0.0019	1.2112
> 5600	3.7360	57.9228	227.2	62.2378	0.0440	97.7488
Sum	3.9250	61.1135	239.9078	81.2312	0.8306	102.9772

Considering the XRF results (Table 9 and Table 10), it is possible to calculate metal distribution in each size fraction. Table 11 and Fig. 6 illustrate metal distribution for different size fractions. Fig. 6 shows that almost all cathode active material (Co, Ni, and Mn) is distributed above 5600 mm. As mentioned above, there is an error for Al for the fraction size of 1000-2000 mm.

Table 11. Metal distribution for different size fractions after thermal treatment

Size (mm)	Fe (%)	Co (%)	Ni (%)	Cu (%)	Al (%)	Mn (%)
d < 125	0.26	0.08	0.08	0.16	0.01	0.07
125 < d < 500	2.61	2.32	2.51	8.56	0.24	2.30
500 < d < 1000	0.97	0.84	0.89	6.01	0.12	0.82
1000 < d < 2000	0.74	0.64	0.75	7.52	94.10	0.71
2000 < d < 5600	0.23	1.34	1.07	1.13	0.23	1.18
> 5600	95.19	94.78	94.70	76.62	5.30	94.92
Sum	100	100	100	100	100	100

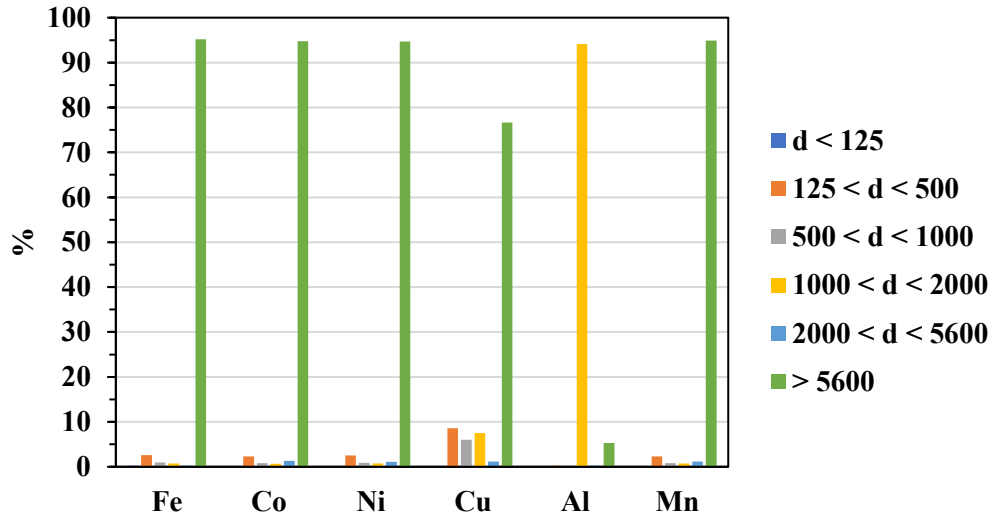

Fig. 6 Graphical representation of metal distribution in different size fractions after thermal treatment.

4.3.5 Estimation of Chemical Composition of the Material by Chemical Attack

In this section chemical composition of the samples was determined by chemical attack. A small amount of different size fractions was dissolved in aqua regia, and the solutions were analyzed by ICP. These investigations were performed for the different size fractions before and after thermal treatment, which are presented in the following. It should be noted that for the larger fraction sizes, the samples were milled before chemical attack to obtain a homogeneous sample for the analysis.

4.3.5.1 Chemical composition before thermal treatment

Different-sized fractions before thermal treatment were dissolved in aqua regia to determine the chemical composition of the samples. The results are shown in Table 12. As can be seen, the initial sample contains 2.56% Li, 3.41% Co, 11.79% Ni, 4.13% Mn, 6.21% Cu, and 10.93% Al.

Table 12. Chemical composition of the different size fractions before thermal treatment (chemical attack results)

Size (mm)	Li (%)	Fe (%)	Co (%)	Ni (%)	Cu (%)	Al (%)	Mn (%)
d < 125	1.11	0.50	1.41	5.03	3.98	0.52	1.75
125 < d < 500	1.24	0.21	1.64	5.84	4.42	0.48	2.00
500 < d < 1000	1.85	0.44	2.34	8.22	12.12	1.24	2.81
1000 < d < 2000	2.44	1.23	3.03	10.67	16.02	2.72	3.63

2000 < d < 5600	2.62	0.25	3.71	13.26	15.34	3.07	4.52
> 5600	3.72	0.33	4.98	17.53	7.30	4.11	5.88
Initial sample_1	2.63	0.14	3.48	11.76	5.67	8.26	4.26
Initial sample_2	2.53	0.18	3.42	12.01	5.76	11.82	4.16
Initial sample_3	2.52	0.17	3.32	11.59	7.21	12.71	3.98
Initial sample (average)	2.56	0.16	3.41	11.79	6.21	10.93	4.13

Regarding the chemical attack results, metals distribution in different size fractions was calculated, and the results are presented in Table 13 and Fig. 7. Table 13 shows that about 93% of cathode active material (Co, Ni, Mn, and Li) is present in the size fraction of > 5600 mm.

Table 13. Metal distribution for different size fractions before thermal treatment (chemical attack results)

Size (mm)	Li (%)	Fe (%)	Co (%)	Ni (%)	Cu (%)	Al (%)	Mn (%)
d < 125	0.03	0.14	0.03	0.03	0.05	0.01	0.03
125 < d < 500	1.42	2.43	1.40	1.42	2.29	0.50	1.45
500 < d < 1000	1.04	2.56	0.98	0.98	3.09	0.64	1.00
1000 < d < 2000	1.42	7.40	1.31	1.31	4.21	1.45	1.33
2000 < d < 5600	2.84	2.81	3.01	3.05	7.53	3.04	3.09
> 5600	93.25	84.66	93.26	93.21	82.84	94.36	93.10
Sum	100	100	100	100	100	100	100

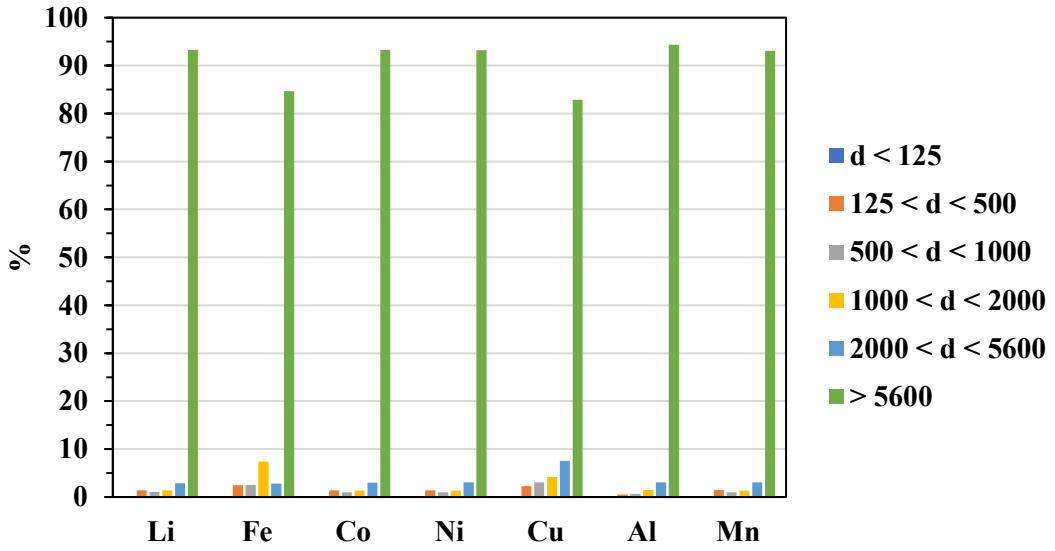

Fig. 7 Graphical representation of metal distribution in different size fractions before thermal treatment (chemical attack results).

4.3.5.2 Chemical composition after thermal treatment

Different size fractions after thermal treatment at 600 °C for 1 hour were dissolved in aqua regia to determine chemical composition of the samples. The results are shown in Table 14. As expected, metal content has been increased for different size fractions due to weight loss after thermal treatment.

Table 14. Chemical composition of the different size fractions after thermal treatment (chemical attack results)

Size (mm)	Li (%)	Fe (%)	Co (%)	Ni (%)	Cu (%)	Al (%)	Mn (%)
d < 125	2.27	1.34	3.12	11.32	8.97	0.90	3.85
125 < d < 500	4.23	0.76	5.75	20.23	12.68	1.23	7.06
500 < d < 1000	2.80	0.18	3.91	13.90	20.51	1.78	4.84
1000 < d < 2000	3.21	0.20	4.65	16.46	26.58	3.27	5.69
2000 < d < 5600	3.61	0.15	5.26	18.63	19.08	3.07	6.40
> 5600	3.85	0.43	5.65	20.16	17.15	1.23	6.82
Initial sample	3.21	0.08	4.58	16.05	19.42	5.53	5.53

Regarding the chemical attack results, metals distribution in different size fractions were calculated and the results are presented in Table 15 and Fig. 8. Table 15 shows that about 89%

of cathode active material (Co, Ni, Mn, and Li) presents in size fraction of > 5600 mm after thermal treatment.

Table 15. Metal distribution for different size fractions after thermal treatment (chemical attack results)

Size (mm)	Li (%)	Fe (%)	Co (%)	Ni (%)	Cu (%)	Al (%)	Mn (%)
d < 125	0.06	0.30	0.05	0.05	0.05	0.06	0.05
125 < d < 500	4.45	7.14	4.14	4.08	2.94	3.67	4.20
500 < d < 1000	1.45	0.82	1.39	1.38	2.35	2.60	1.42
1000 < d < 2000	1.71	0.94	1.70	1.69	3.14	4.94	1.72
2000 < d < 5600	3.60	1.33	3.59	3.57	4.20	8.66	3.61
> 5600	88.74	89.48	89.13	89.22	87.32	80.06	88.99
Sum	100	100	100	100	100	100	100

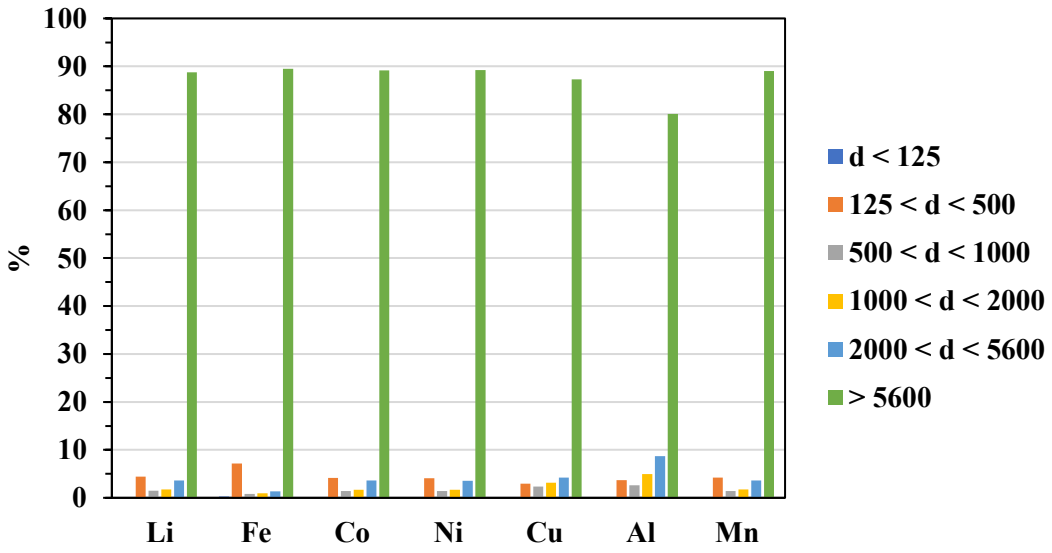

Fig. 8 Graphical representation of metal distribution in different size fractions after thermal treatment (chemical attack results).

4.4 Leaching of Black Mass

Table 16 presents the leaching efficiency of the elements in the sieved sample (<250 µm). As shown, the leaching process achieved efficiencies of over 80% for all elements. Several steps were implemented to enhance the recovery of critical metals from the leaching solution. The initial step involved the removal of Cu through a cementation process, utilizing Fe powder as a reducing agent. The effects of various stoichiometric ratios of Fe to Cu were studied to

determine the optimal conditions for achieving maximum extraction efficiency. In the second step, the removal of Fe and Al through precipitation was investigated at various pH levels to determine the optimal conditions for selective and efficient removal. Along with these processes, the selective extraction efficiency of Mn was also assessed concerning equilibrium pH, employing solvent extraction with D2EHPA and n-heptane as dilutant. Furthermore, the effect of the saponification values was evaluated in the organic phase using NaOH solution. The same approach was followed for the selective separation of Co from the leaching solution using Cyanex 272 and n-heptane as dilutant. For each parameter, a thorough investigation was conducted to understand how extraction efficiencies vary under different conditions, focusing on identifying the optimal conditions for the selective extraction of each element while minimizing co-extraction of the other elements.

Table 16. Leaching efficiency of the elements present in the sieved sample.

Element	Li	Co	Ni	Mn	Cu	Al
Leaching efficiency (%)	97.36	82.53	84.52	80.28	80.86	95.04

4.5 Copper recovery via cementation

The recovery of Cu from the PLS through cementation was studied using Fe powder to optimize the stoichiometric ratio of Fe to Cu in the reaction process. The reaction equation is as follows:

$$Cu^{2+} + Fe \rightarrow Fe^{2+} + Cu \quad (1)$$

This study explored different ratios of 0.9 to 1.2 relative to the stoichiometric value to evaluate their effects on removal efficiency of copper, as detailed in Figure 9. At the 0.9 ratio, it was noted that the recovery efficiency of Cu was incomplete due to the insufficient availability of Fe to sustain the redox reaction, resulting in low removal efficiency of about 75%. At a stoichiometric ratio of 1.2, near-complete recovery of Cu was achieved, with an efficiency of approximately 85%, resulting in a Cu concentration of less than 70 mg/L in the solution. The trend of the fitted curve indicates that the curve approaches a horizontal asymptote at higher iron amount, revealing that adding more iron has minimal effect on Cu removal. These results suggest optimal conditions, as they provide sufficient Fe to sustain the reaction while minimizing reagent wastage. However, excess Fe led to higher residual iron in the solution, which could subsequently increase downstream processing costs and intensify environmental concerns. The reaction of copper cementation by iron powder is primarily controlled by boundary layer diffusion[90], [91]. Increasing the temperature can enhance the reaction,

resulting in higher Cu removal efficiencies. However, this approach also increases process costs and causes excessive dissolution of iron powder.

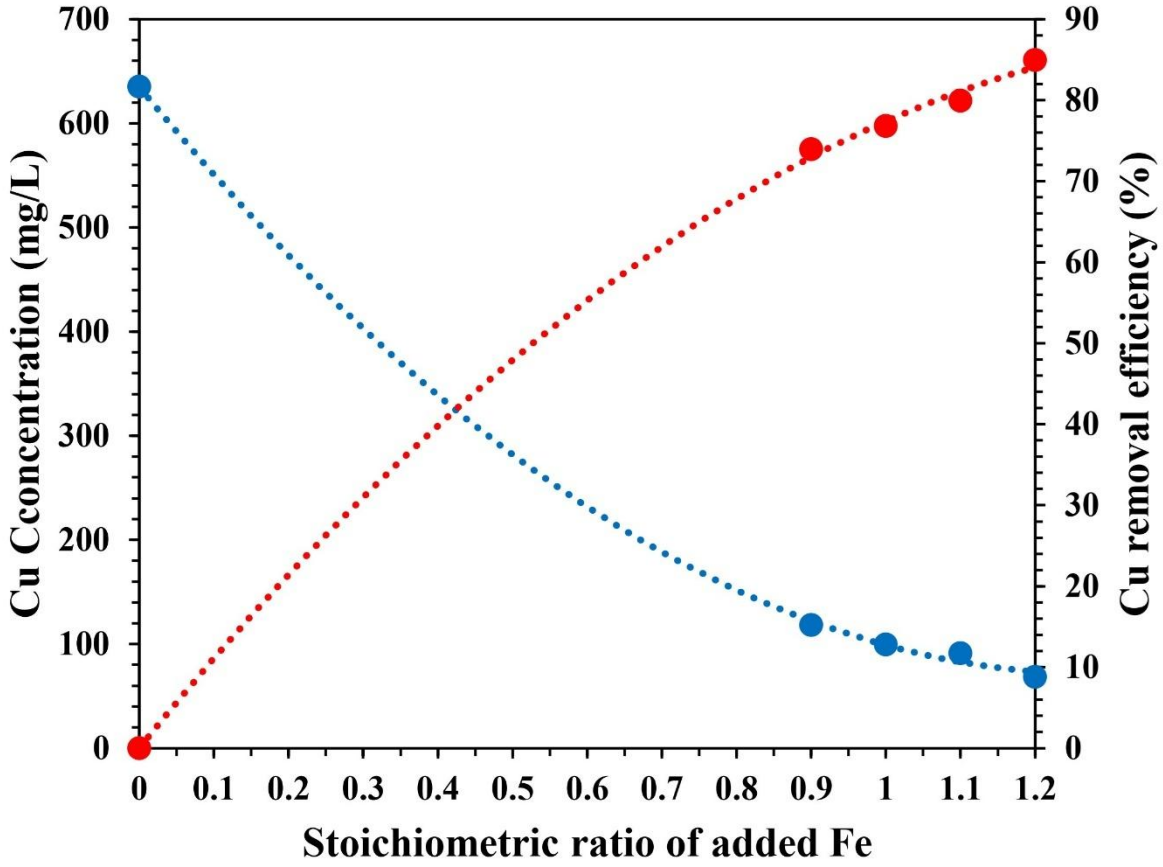

Fig. 9 Cu removal through cementation, where red dots indicate the removal efficiency of Cu and blue dots indicate the final concentration of Cu in the solution

4.6 Fe and Al precipitation

The precipitation of Fe and Al from the leaching solution, following Cu recovery, was systematically studied by adjusting the solution's pH. The aim was to determine the optimal pH for maximum removal efficiency of Al and Fe while minimizing the co-precipitation of critical elements present in the solution. Figure 10 indicates that precipitation efficiency was strongly dependent on pH, directly affecting metal hydroxides' formation and solubility. Figure 10 shows that at low pH values (pH ~ 4.5), both Fe and Al remained primarily soluble, with minimal precipitation due to the lower hydroxide formation under acidic conditions. As the pH increased to a moderate range (pH 5–6), iron hydroxide precipitated significantly, increasing efficiency steadily. At the same time, Al precipitation commenced at slightly higher pH values, reflecting its higher solubility. At higher pH values (pH > 6), near-complete precipitation was

observed for both Fe and Al, with optimal pH ranges determined to be approximately 6.0 for Fe and 6.5 for Al. Beyond these values, precipitation efficiency plateaued, indicating that further increases in pH offered no additional benefit and could lead to unnecessary reagent use. A study by Meshram et al. [92] demonstrated that Fe can be completely precipitated at a pH of approximately 4.5, while Al can be entirely removed at a pH range of 7–8, indicating lower pH levels for complete removal of both elements. Another study reported the same pH value for iron removal but found that complete aluminum removal occurred at a pH of approximately 6 [90].

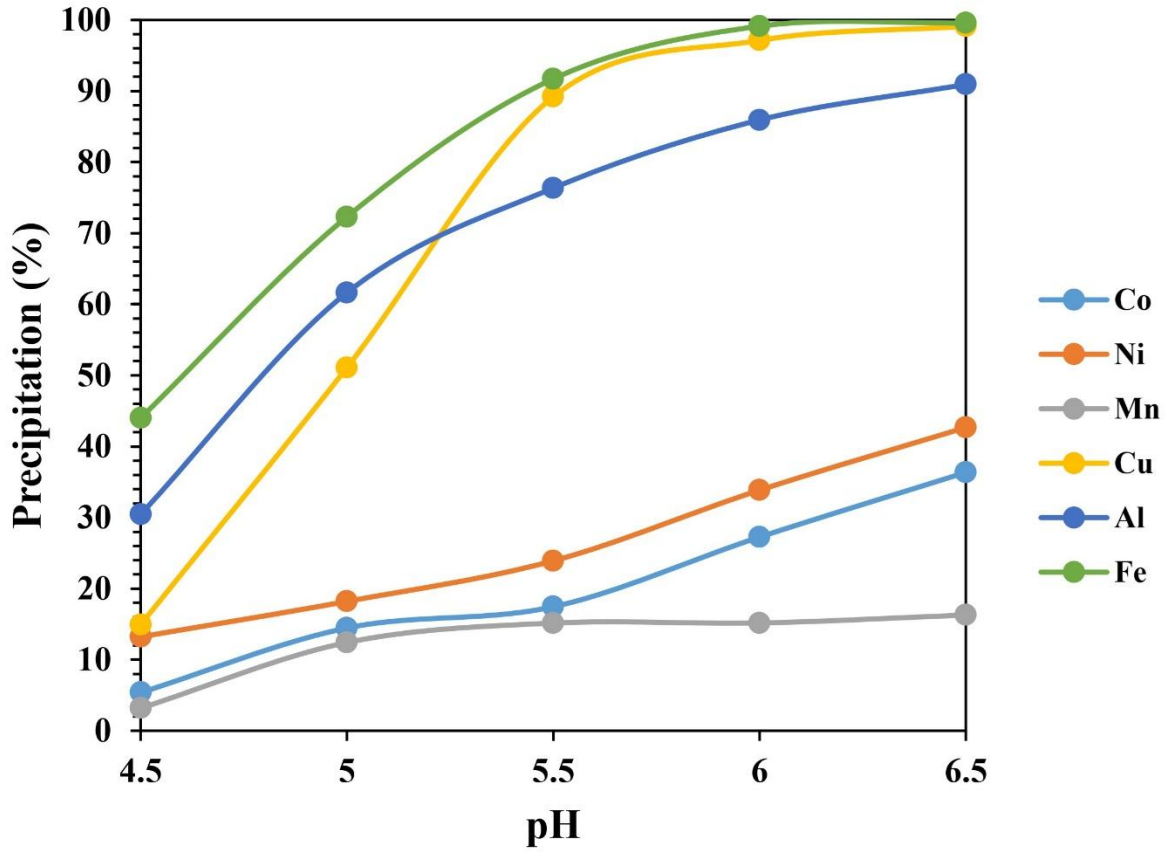

Figure. 10 Precipitation efficiency of the elements in the leaching solution versus pH

4.7 Manganese separation using D2EHPA

The recovery of manganese from the PLS after removing the Cu, Fe, and Al was studied through solvent extraction using D2EHPA diluted in n-heptane by varying the equilibrium pH from 2 – 6 as shown in Figure 11. The data reveal a clear trend where the extraction efficiency of Mn increases with an increase in pH from approximately 50% at pH of 2 to about 99% at pH>4 to onward pH value. As the pH increased from 2 to 3, Mn recovery improved

significantly, reaching maximum efficiency in the higher pH range. This increase is attributed to the enhanced availability of negatively charged D2EHPA ligands capable of forming stable complexes with Mn. Moreover, the increase in pH not only facilitated the Mn extraction but also helped to promote the co-extraction of other elements, particularly Co, Ni, and somehow Li, as shown in Figure 11. The effect of this co-extraction became more pronounced as the pH values increased. The co-extraction of Co and Ni occurs due to the similar chemical behavior of these metals in the presence of D2EHPA, especially under conditions where sufficient ligands and higher pH favor the formation of their respective metal complexes. As a result, the selectivity for Mn recovery was significantly reduced at elevated pH values, posing challenges for achieving pure Mn extraction. The overlapping extraction efficiency trends for Mn, Co, and Ni at higher pH highlighted the need for careful optimization of pH to balance Mn recovery with minimal co-extraction of other elements. The optimal pH range for selective Mn recovery is determined as a balance between maximizing Mn extraction and minimizing the co-extraction of Co and Ni, which is placed below a pH of 3.

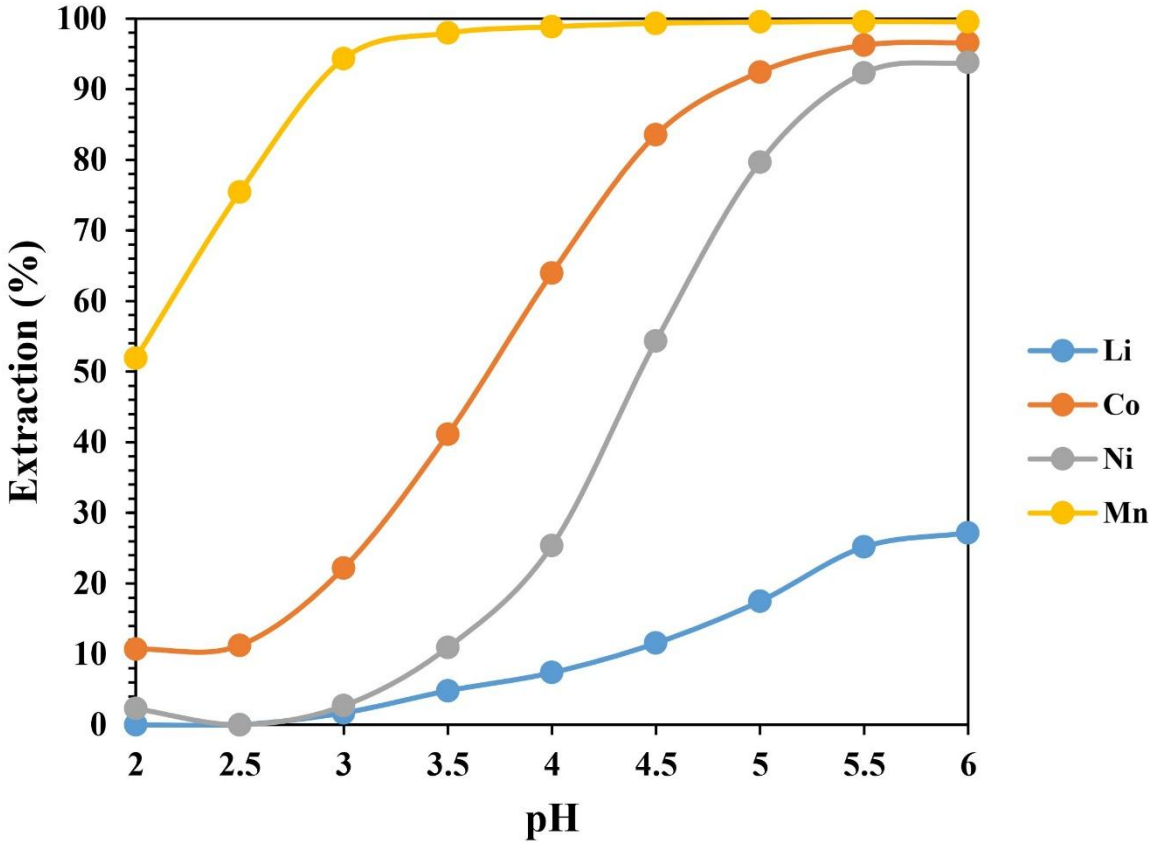

Figure. 11 Extraction efficiency (D2EPHA versus pH) of the different elements, specifically Mn and co-extraction of other elements from the leaching solution

4.8 D2EHPA Saponification experiments

After investigating the influence of equilibrium pH on the extraction efficiency of Mn, the saponification of the organic phase using a 30% NaOH solution was also investigated. This approach involves neutralizing the acidic extractant by converting it into its sodium salt, replacing specific protons in its structure with sodium ions. This process, referred to as saponification, which helps to maintain a good pH control over the extraction reaction, can be represented as follows[93], [94]:

$$Na^{+}_{(aq)} + \frac{1}{2}(HA)_{2_{(org)}} \leftrightarrow NaA_{(org)} + H^{+}_{(aq)} \quad (2)$$

Experimental data presented in Figure 12 indicates that as the saponification value of the organic phase increased, the extraction efficiency of Mn improved significantly up to 15%. However, at higher saponification values, along with the higher extraction efficiency of Mn, there was also an increase in the co-extraction of Co and Ni. As the saponification level rose, extensive deprotonation of D2EHPA is performed due to higher equilibrium pH, which improves the extraction efficiency of Co and Ni and compromised the selectivity for Mn recovery. It was noted that the optimal saponification was achieved at 15 %, with about 92% Mn extraction efficiency while limiting the co-extraction of Co and Ni. The equilibrium pH values indicated on the dots in Figure 12 closely align with the results shown in Figure 11, demonstrating that adjusting the saponification values allows for effective control over the equilibrium pH and the extraction efficiency of the elements.

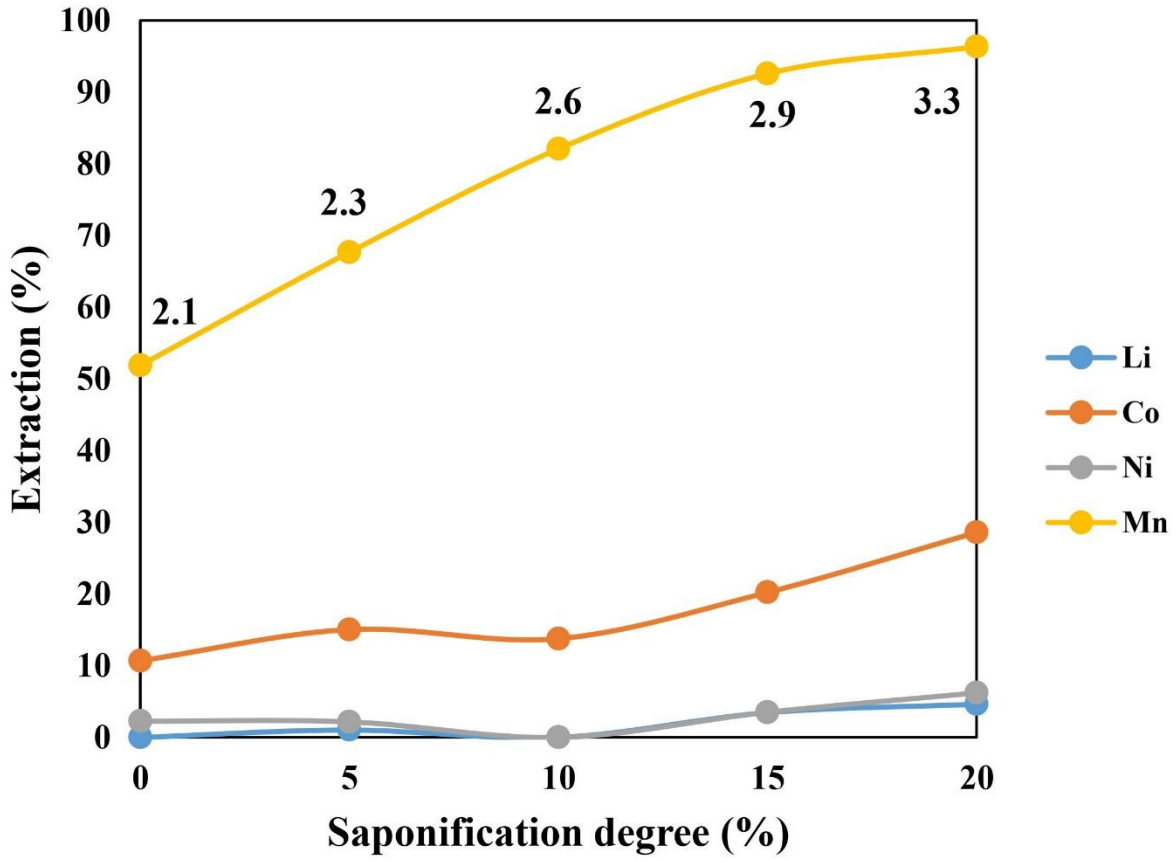

Figure. 12 Effect of saponification degree on the extraction efficiency of the elements using D2EHPA as extractant. The values on the dots represent the equilibrium pH.

4.9 Manganese stripping experiments

The efficiency of stripping the organic phase following Mn extraction using a 15% saponified D2EHPA was examined with different concentrations of H_2SO_4 as the stripping agent, ranging from 0.1 M to 0.5 M. Figure 13 presents the stripping efficiencies for Mn, Co, Ni, and Li with H_2SO_4 concentration. The maximum stripping efficiency for all elements was observed at 0.2 M. Further increases in H_2SO_4 concentration beyond this level did not significantly enhance stripping efficiency, suggesting that the process had attained its optimal efficiency. The stripping efficiency for Mn increased significantly with H_2SO_4 concentrations up to 0.2 M, achieving approximately 92%. This behavior indicates the efficient disruption of metal-ligand complexes in the organic phase at this concentration, facilitating optimal Mn recovery. Cobalt attained a stripping efficiency of approximately 65% at 0.2 M H_2SO_4, after which the efficiency stabilized. Lithium and nickel exhibited lower stripping efficiencies, stabilizing at around 41% and 37%, respectively, beyond 0.2 M H_2SO_4. The absence of enhancement in stripping efficiency beyond 0.2 M suggests that the system has attained saturation, with the acid

concentration being adequate to protonate the ligand and facilitate the release of metals effectively. Increasing the acid concentration further offers no additional advantage while potentially increasing operational costs and the risk of equipment corrosion, underscoring the cost-effectiveness of using 0.2 M H_2SO_4 for optimal stripping.

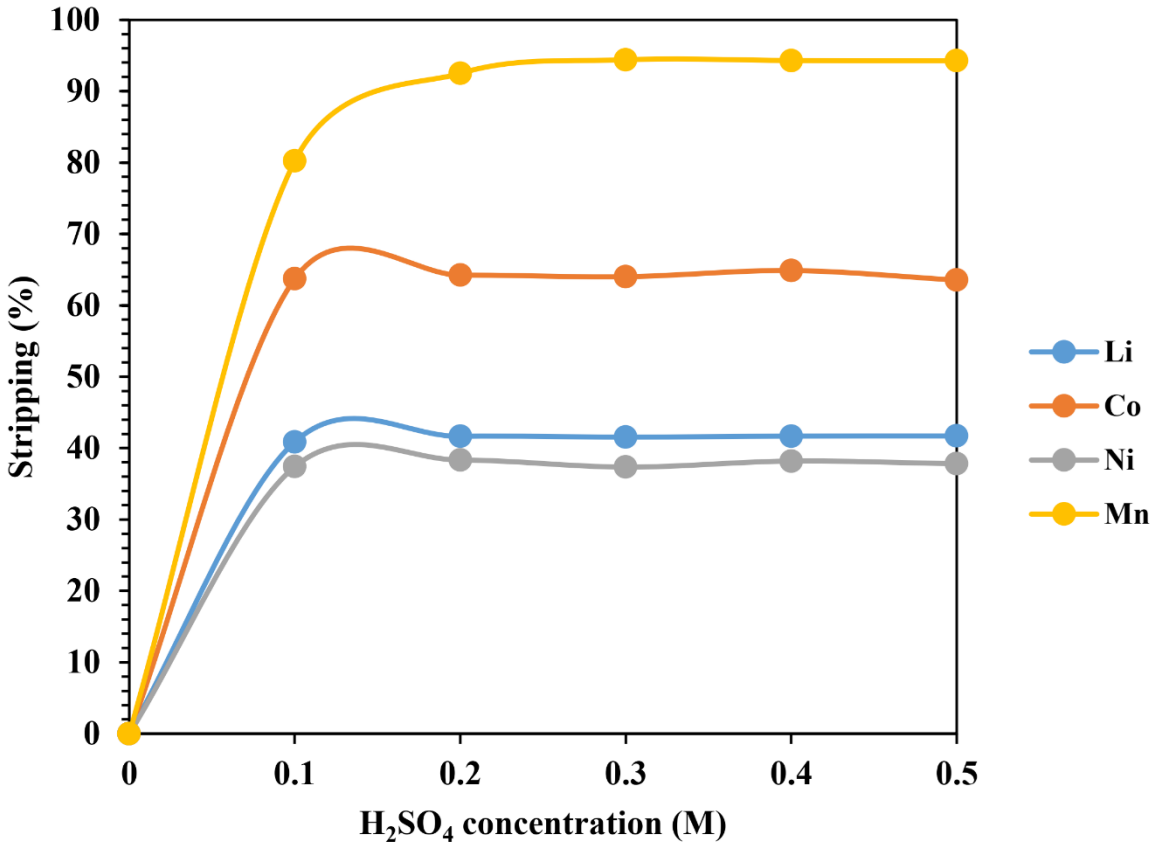

Figure 13. Effect of H_2SO_4 concentration on the stripping efficiency of Mn and co-extracted elements with O/A ratio of 1, after extraction by a 15% saponified D2EHPA.

Subsequently, 0.2 M sulfuric acid was employed as the stripping agent to evaluate the effect of O/A ratio on the concentration of metals in the final aqueous solution. The tested ratios were 1:1, 2:1, 4:1, 6:1, and 8:1. The results presented in Figure 14 show a linear trend up to a ratio of 6:1, which indicates that effective stripping of Mn and other elements from the organic phase was achieved. This finding indicates that a higher proportion of the organic phase does not impede stripping efficiency, thereby enhancing the scalability and cost-effectiveness of the process.

However, the concentration of Mn in the aqueous phase increased significantly with higher O/A ratios, reaching approximately 12,000 mg/L at a 6:1 ratio. This trend illustrates that sulfuric acid at 0.2 M is sufficient to maintain high stripping efficiency even with an excess of

organic phase. For Co, Ni, and Li, the concentrations in the aqueous phase also increased slightly with higher O/A ratios, though their overall concentrations remained much lower compared to Mn. This reflects the low co-extraction efficiency of these elements with Mn, using a 15% saponified D2EHPA under the tested conditions.

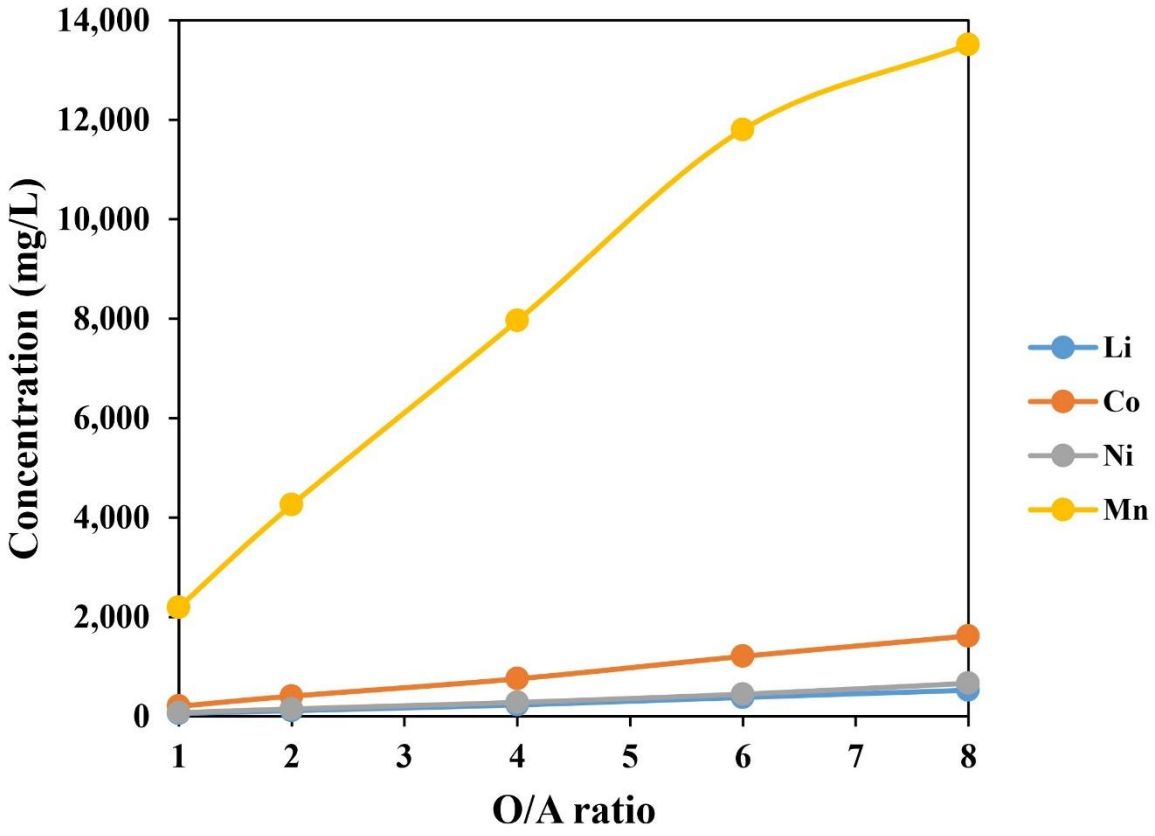

Figure 14. Effect of O/A ratio on the concentration of Mn and co-extracted elements in the final aqueous phase after stripping from a 15% saponified D2EHPA, using a 0.2 M H2SO4 solution.

4.10 Cobalt separation using Cyanex 272

Following the recovery of Mn with D2EHPA, the selective extraction of Co from the raffinate was conducted using Cyanex 272 and n-heptane as a dilutant. To determine the optimal conditions for the selective extraction of Co, the influence of equilibrium pH was assessed and illustrated in Figure 15. Experimental results indicated that approximately 90% extraction efficiency of Co was achieved at a pH of around 4.5. At this pH, minimal co-extraction of other elements, such as Ni and Li, was achieved, ensuring high selectivity. The selective behavior observed at this pH results from the preferential binding of Cyanex 272 to Co ions, leading to the formation of stable complexes.

As the pH increased beyond 4.5, the extraction efficiency of Co continued to rise; however, the co-extraction of other elements, such as Ni, also increased. This trend underscores a significant trade-off between extraction efficiency and selectivity. The concurrent rise in co-extraction diminishes the purity of the recovered cobalt and complicates subsequent processing. The graph demonstrates a distinct maximum in selective extraction efficiency at pH 4.5, followed by a decrease in selectivity as the curves for other elements increase. At lower pH values, the extent of deprotonation is constrained, thereby limiting extraction efficiency. With an increase in pH, deprotonation occurs, resulting in enhanced metal binding and extraction. This also facilitates the extraction of elements with analogous chemical properties to cobalt, such as nickel, which competes for binding sites. The graph also indicates that, following cobalt extraction, selective separation of Ni from Li is achievable at a pH range of 6-6.5.

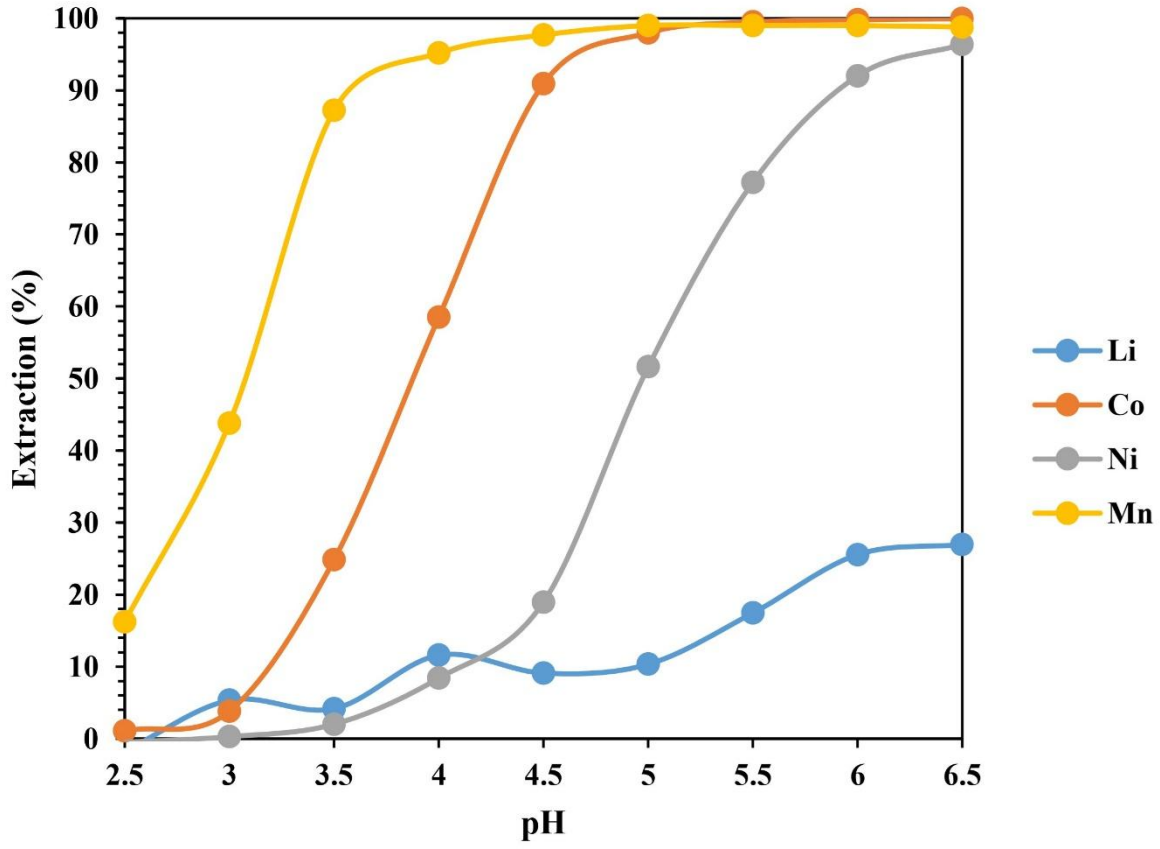

Figure 15. Extraction efficiency of the elements in the raffinate after Mn separation, using Cyanex 272 versus pH.

4.11 Cyanex 272 Saponification Experiments

The saponification effect of the organic phase, which included Cyanex 272 and n-heptane, was also investigated for Co extraction, with a 30% NaOH solution as the saponifying agent. It was

noted that saponification improves Cyanex 272 deprotonation due to higher equilibrium pH and making stable cobalt complexes more likely to form. Figure 16 shows that an increase in saponification value correlates with significantly improving Co extraction efficiency. The observed trend is associated with increased reactivity of the saponified organic phase, which allows for better Co recovery.

The findings in Figure 16 show that the optimal saponification range for selective Co extraction is 10-12%, which maximizes Co recovery to about 91% while reducing co-extraction of other elements. Similar results were reported in a recent study at a lower saponification degree of 7% [94]. The improvement in Co recovery above this range does not justify the significant increase in co-extraction, which reduces the purity of the recovered Co and complicates subsequent separation processes. Moreover, the graphical trends show a significant increase in Co extraction efficiency as saponification values rise to 15%, followed by a plateau at higher levels. The extraction efficiencies of competing elements rise simultaneously, indicating a trade-off between extraction efficiency and selectivity. The equilibrium pH values represented by the dots in Figure 16 closely correspond to the results in Figure 15, illustrating that modifying the saponification values enables precise control over the equilibrium pH and the extraction efficiency of the elements.

Following the selective recovery of Co using 12% saponified Cyanex 272, 96% of Ni was extracted using 26% saponified Cyanex 272, achieving an equilibrium pH of 6.5 with minimal co-extraction of Li (26%). Finally, both organic phases after cobalt and nickel extraction were successfully stripped using a 0.2M H_2SO_4 solution. Approximately 92% of cobalt and 21% of nickel were stripped after cobalt extraction, while about 98% of nickel and 99% of cobalt were stripped from the nickel-loaded organic phase.

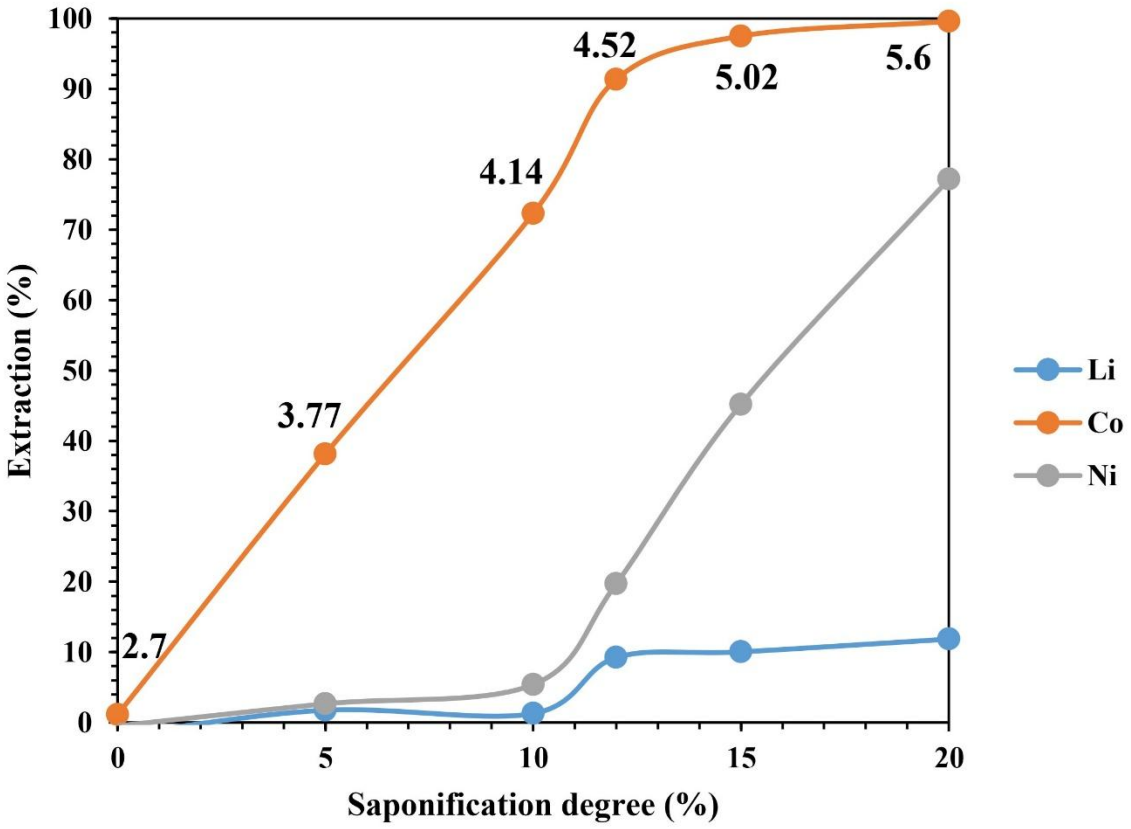

Figure 16. Effect of saponification degree on the extraction efficiency of the elements using Cyanex 272 as extractant.

4.12 Mathematical Model and Slope Analysis

Considering the equilibrium state after extraction process, the following equations can be written for all three divalent elements that are extracted by D2EHPA or Cyanex 272:

$$M^{+2}_{(aq)} + 2H_2A_{2(org)} = M(HA_2)_{2(org)} + 2H^{+}_{(aq)} \tag{3}$$

$$K = \frac{\left[M(HA_2)_{2(org)}\right].\left[H^{+}_{(aq)}\right]^2}{\left[M^{+2}_{(aq)}\right].\left[H_2A_{2(org)}\right]^2} \tag{4}$$

$$\log K = \log\frac{\left[M(HA_2)_{2(org)}\right]}{\left[M^{+2}_{(aq)}\right]} + 2\log\left[H^{+}_{(aq)}\right] - 2\log\left[H_2A_{2(org)}\right] \tag{5}$$

$$\log D = \log K + 2\log\left[H_2A_{2(org)}\right] + 2pH \tag{6}$$

Here, M represents Mn, Co, and Ni; H_2A_2 denotes the extractant; $M(HA_2)_2$ is the metal-extractant complex; K represents the equilibrium constant; and D is the distribution coefficient. Therefore, plotting log D against the equilibrium pH should theoretically result in a slope of 2 for Mn, Co, and Ni. Hence, several experiments were conducted at various equilibrium pH levels, adjusted using NaOH solution for both extractants. However, the results shown in Figure 17 reveal that, contrary to predictions, none of the lines exhibit slopes of 2; instead, most slopes are approximately 1. This is notable because Mn, Co, and Ni are well known to exist as divalent ions in this system, releasing two hydrogen ions during the complexation and extraction process. The observed slope of 1 may indicate that half of the released protons were neutralized by the added NaOH used to adjust the equilibrium pH to different values. Keller et al. [95] also reported the same slope value, suggesting that the deviation from the theoretical value of 2 is due to the presence of sulfate ions, which partially absorb the emitted protons.

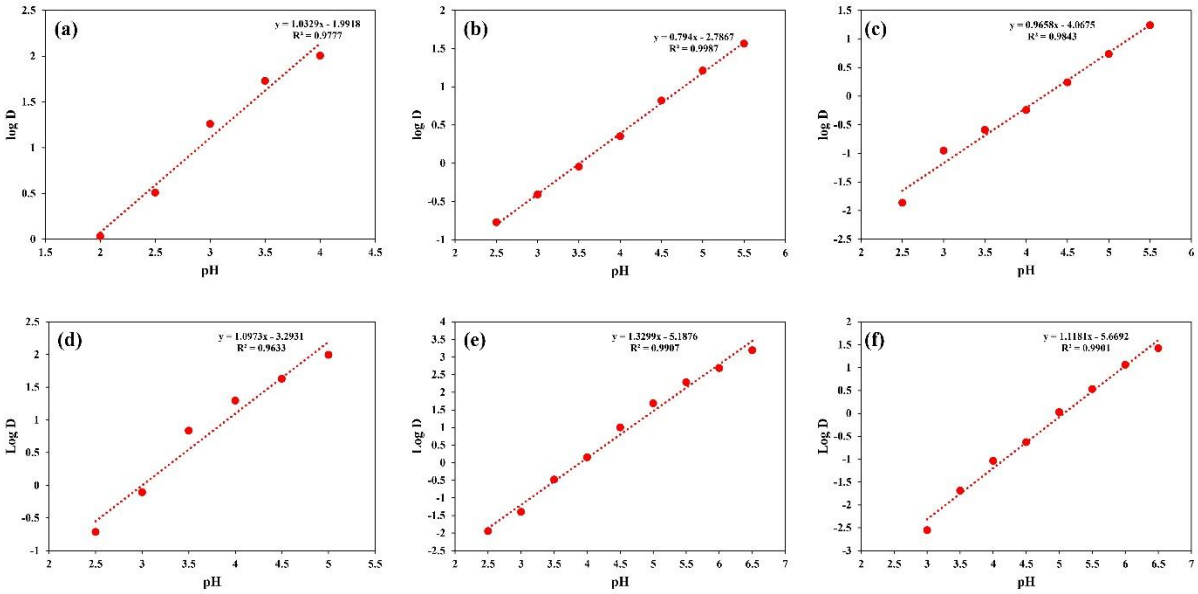

Figure 17. log D vs pH for the extraction experiments using D2EPHA: (a) Mn, (b) Co, (c) Ni, and Cyanex 272: (d) Mn, (e) Co, and (f) Ni.

4.13 Process flowsheet

Based on the results, a process flowsheet is proposed, as illustrated in Figure 18, to recover all elements of interest from the ground mixture of cathodes and anodes. The process begins with sieving, which concentrates the cathode active materials into a powder suitable for leaching. Hydrogen peroxide-assisted sulfuric acid leaching effectively dissolves most elements, transferring them from the solid phase into the solution.

In the first recovery stage, copper is efficiently recovered by adding iron powder in an amount corresponding to the appropriate stoichiometric ratio. Next, the iron and aluminum in the solution are removed by adjusting the pH to relatively high levels, up to 5.5. Subsequently, manganese is selectively recovered using D2EHPA at an optimal pH of approximately 3. Finally, cobalt and nickel are separated from lithium using Cyanex 272, with cobalt recovering at a pH of 4.5 and nickel at a pH of 6.5.

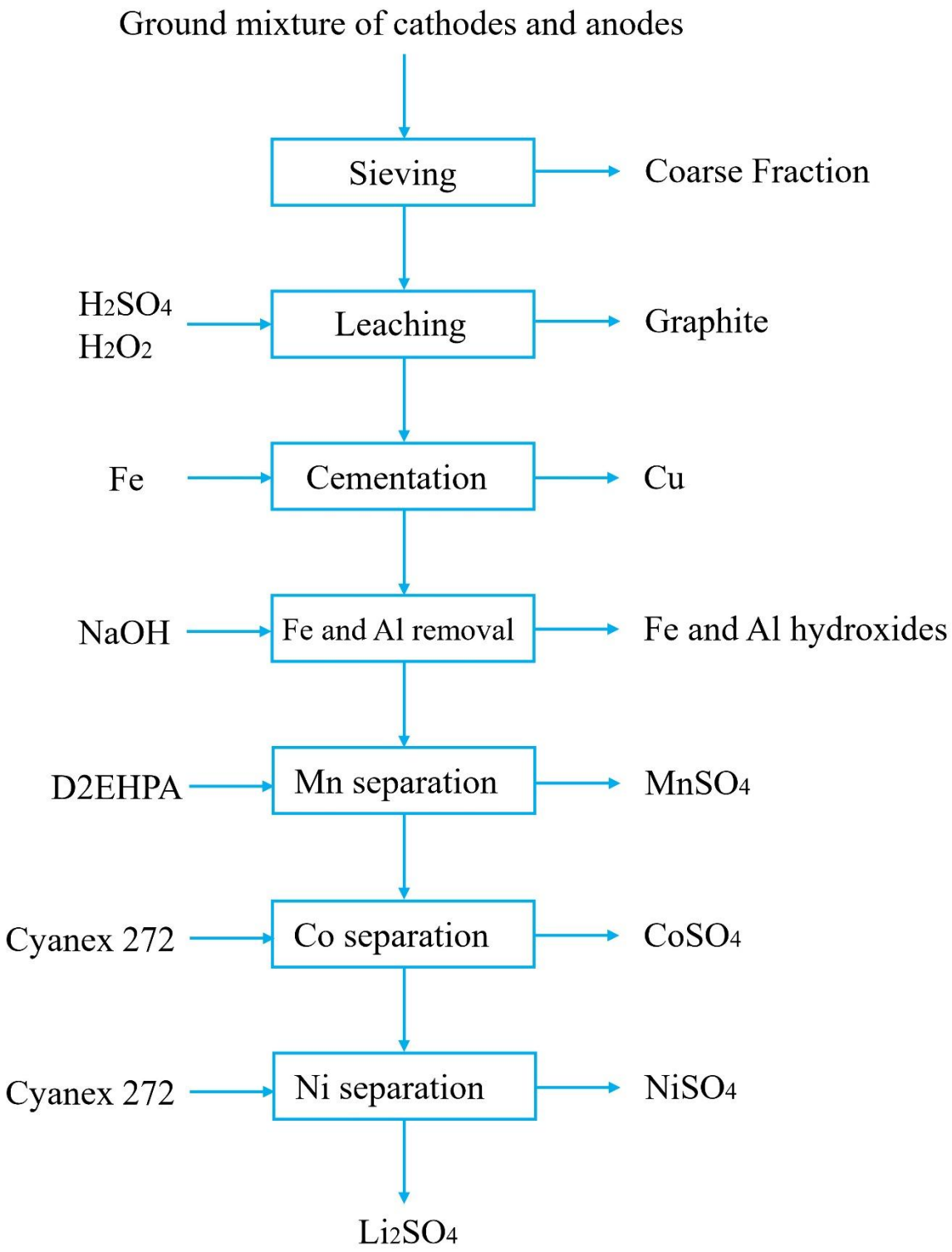

Figure 18. Process flowsheet to separate and recover the elements present in the recovered cathode active material through sieving

4.14 Conclusions

This study introduces a comprehensive and scalable approach for the selective recovery of metals from spent LIBs, tackling the technical and environmental challenges associated with LIBs recycling. By optimizing critical parameters such as pH, saponification value, and stripping conditions, an efficient extraction of the elements was achieved. Copper recovery experiments revealed that the optimal ratio of Fe-Cu of 1.2 is sufficient to achieve 85% Cu recovery. Iron and aluminum removal was conducted at pH of 5.5. The extraction of Mn using D2EHPA highlighted the significance of pH in attaining selective recovery. The ideal pH for Mn extraction was determined to be 3, resulting in an extraction efficiency of about 92%, using a 15% saponified D2EHPA diluted in n-heptane. The stripping efficiency of the manganese loaded organic phase was assessed using different concentrations of H_2SO_4 and varying organic-to-aqueous (O/A) phase ratios. A 0.2 M concentration of H_2SO_4 was identified as optimal for the extraction of Mn and other metals, attaining approximately 92% efficiency for Mn stripping.

Cyanex 272 demonstrated efficacy as an extractant for cobalt recovery, achieving approximately 91% extraction efficiency at a pH of 4.5. Exceeding this pH results in enhanced co-extraction of additional metals, such as Ni, thereby diminishing selectivity. The mathematical model evaluated the correlation between log D and equilibrium pH during the extraction process of Mn, Co, and Ni, using D2EHPA and Cyanex 272 as extractants, based on a cation exchange mechanism.

CHAPTER 5

Efficient Extraction of Li and Fe from Spent $LiFePO_4$ Cathodes Using Leaching and Selective Precipitation

5.1 Introduction

LIBs are now central to modern energy storage, powering electronic devices to electric and hybrid vehicles. Within this, lithium iron phosphate ($LiFePO_4$, LFP) batteries stand out for their safety, thermal stability, and long cycle life, which have made them a preferred choice for large-scale applications [96]. However, the rapid growth in Li demand and supply challenges has raised significant concerns about long-term supply and sustainability, placing battery recycling at the forefront of global research and policy [97], [98].

Due to its economic value and the risks of supply shortages, the European Union (EU) has recognized Li as a critical raw material. In 2019 – 2020, LIBs technologies accounted for ~65% of global Li consumption [99]. From the literature, it was revealed that most of the Li is obtained from imported minerals such as spodumene. To reduce this dependency, the EU has increased their efforts to promote Li recycling, which may help reduce it dependence on external suppliers [100], [101].

Environmental concerns are equally important in the context of LIBs [102]. These batteries use a liquid electrolyte composed of lithium hexafluorophosphate ($LiPF_6$) dissolved in organic solvents. The electrolyte is both toxic and reactive with other substances that pose serious environmental and safety risks if not properly handled. In addition, the loss of valuable metals such as Li, Fe, Al (aluminium), Cu (copper), and Co (cobalt) not only reduces available resources but also contributes to pollution [103]. Since industrial activity already accounts for nearly half of global greenhouse gas emissions and significant biodiversity loss, efficient recovery of these metals is essential. The circular economy framework provides a practical approach to reducing environmental impacts while ensuring a stable supply of critical raw materials [104].

The material composition of LFP batteries demonstrates their strong recycling potential. On average, these batteries contain 22.2% (Al), 0.4% (Li), 3.1% (Fe), 10.9% carbon (C), and 10.5% (Cu) [105]. The black mass (BM) obtained from cathodes contains even higher levels of critical elements, with approximately 2% Li, 22% Fe, and 7% Al, although the exact values may differ depending on the manufacturer [106]. Understanding this composition is important

for developing efficient recycling processes that recover these metals while reducing environmental impact [107].

Recycling methods for LIBs include both physical and chemical processes. Pyrometallurgical techniques, such as preheating, pyrolysis, and melting, are widely used for cobalt recovery. However, these processes are inefficient for lithium recovery and require high energy input, limiting their sustainability [108]. Alternatively, hydrometallurgical processes using acid leaching and precipitation are more efficient, achieving over 99% Li and Co recovery and 98% Cu recovery, depending on the conditions [109]. The most common leaching agents are H_2SO_4, HCl, and H_3PO_4, while organic acids like oxalic and citric acid offer a more environmentally friendly alternative, though they are costlier and complicate metal separation [110], [111]. Biological leaching, using microbial metabolites to dissolve metals, has also been explored but remains in the experimental stage [112].

Among hydrometallurgical techniques, inorganic acid leaching is the most widely adopted due to its ability to break down $LiFePO_4$'s crystalline structure. H_2SO_4 and HCl are particularly effective, while oxidation-assisted leaching converts Fe^{2+} to Fe^{3+}, enabling selective Li dissolution [113]. Mechanochemical leaching enhances efficiency by utilizing differences in solid-liquid phase properties [114]. Various hydrometallurgical techniques have been explored, with H_2SO_4 leaching at 60°C for 4 hours achieving 97% Li and 98% Fe recovery, yielding $FePO_4 \cdot 2H_2O$ and Li_2CO_3 [115], [116]. Similarly, HCl with H_2O_2 has shown 92.15% Li and 91.73% Fe recovery, while oxalic acid leaching at 80°C has achieved 98% Li and 92% Fe recovery [117]. Table 1 summarizes some developed leaching processes for the recovery of metals from spent LFP batteries.

***Table 1**: Hydrometallurgical process for LFP battery recycling*

Acids	Reagents	Reaction Conditions	Recovery	Reference
Inorganic Acids	Strong H_2SO_4	95°C, 3M H_2SO_4, 150 mins	Li and Fe	[118]
	H_2SO_4 + H_2O_2	80°C, 2M acid, 3% H_2O_2, 120 min	Li and Fe	[119]
	HCl	80°C, 2M HCl, 90 mins	Li and Fe	[120]
	HCl + H_2O_2	85°C, 2M acid, 5% H_2O_2, 120 min	Li and Fe	[121]
	HNO_3	95°C, 3M HNO_3, 150 mins	Li and Fe	[28]

Organic Acids	Citric acid ($C_6H_8O_7$) + H_2O_2	90 °C, 0.5M acid, 2% H_2O_2, 120 min	Li, Fe, and P	[122]
	Gluconic Acid ($C_6H_{12}O_7$) + H_2O_2	90 °C, 1M acid, 2% H_2O_2, 180 min	Li and Fe	[123]
	Lactic Acid ($C_3H_6O_3$) + H_2O_2	85 °C, 1.5M acid, 2% H_2O_2, 120 min	Li and Fe	[124]
	Oxalic Acid ($C_2H_2O_4$)	85°C, 1M acid, 180 mins	Li and Fe	[111]
	Ascorbic Acid or Vitamin C	90°C, 1M acid, 150 mins	Li and Fe	[125]

Given the increasing demand for Li, recycling is expected to play a major role in supply chain stabilization. The recovery of Li and Co from spent batteries could generate up to $22,000 per ton [126]. Li prices depend on its chemical form, with lithium hydroxide (LiOH) being more valuable than lithium carbonate (Li_2CO_3) due to its use in cathode production [127]. Market trends show slow growth between 2000 and 2015, followed by a rapid increase after 2015, with LiOH prices rising 92% and Li_2CO_3 120%. However, between 2018 and 2020, Li prices declined due to increased supply. Analysts predict 33% annual Li production growth from 2022 to 2025, stabilizing supply while increasing reliance on recycled sources [128]. Recycling LFP batteries presents an opportunity to develop a sustainable supply chain while reducing reliance on Li mining[129].

The leaching, purification, and metal recovery processes ensure high efficiency with minimal environmental risks. Compared with pyrometallurgy, hydrometallurgical methods can be conducted under mild temperature and pressure conditions, making them more suitable for LFP battery recycling [130]. Optimizing these methods is crucial in meeting the growing demand for Li while addressing environmental and economic challenges.

Therefore, this study aims to develop an efficient hydrometallurgical process for the selective recovery of Li and Fe from spent LFP batteries. This research contributes to sustainable

resource management and the circular economy by optimising leaching and selective precipitation. The findings will help reduce dependence on primary Li sources, stabilize global supply, and minimize the environmental footprint of LIBs disposal. As the demand for Li rises, improving battery recycling methods will be key to ensuring a more sustainable future.

5.2 Materials and Methods

5.2.1 Materials

The cathode sheets, which are aluminium foils coated with $LiFePO_4$ from ORIM S.P.A.'s LiBS, were used to conduct these experiments. These foils contained the active material, which was removed and then reduced in size before leaching tests. This material, called black mass, was used for further experiments. The LIB configuration consists of an assembly of Cu and Al foils, with Li primarily present in the latter, making them the focus of the study. All the reagents, including organic and inorganic acids, were of analytical grade. A pH meter, a magnetic stirrer with a heating plate, a vacuum filtration apparatus using Whatman filter papers, a drying oven, and glassware were also utilized.

5.2.2 Experimental Procedures

5.2.2.1 Characterization of Spent Batteries

To have accurate experimental analysis, it is crucial to have a complete characterization of the black mass. Usually, the process involves elemental analysis and morphology. To dissolve the metallic components, a three-time replication for acid digestion using aqua regia was performed. The obtained solutions were then analysed using Inductively Coupled Plasma Optical Emission Spectroscopy (ICP-OES), with each measurement performed in triplicate to ensure reproducibility.

5.2.2.2 Leaching Tests

Preliminary leaching experiments were conducted to identify the most effective acid for Li and Fe recovery. Various acids were tested, including 96% sulfuric acid, 65% nitric acid, 37% hydrochloric acid, oxalic acid hydrate, citric acid monohydrate, and glacial acetic acid. These experiments were carried out under controlled conditions with an acid concentration of 1 N, a 10% solid-to-liquid ratio, stirring at 250 rpm, and a reaction time of 30 minutes. After the leaching process, the mixture was centrifuged at 5000 rpm for 4 minutes, and both the solid residue and liquid phase were analysed for metal content.

Based on the results, sulfuric acid was selected for further optimization using a factorial design. A 2-level, 3-factor factorial experimental design was applied to optimize key process

parameters: varying acid concentration (ranging from 0.5 to 1.5 N), agitation speed (from 150 to 350 rpm), and the percentage of cathode material (from 5% to 15%). Central point replications were included to estimate experimental error, and the Yates method was employed to determine the significant effects on Li, Al, and Fe recovery.

5.2.2.3 Precipitation Tests

After that, the precipitation process was carried out, which aimed to selectively remove Fe from the leachate while keeping Li in solution. The variations in the amounts of the precipitating agent were also evaluated using stoichiometric calculations based on the concentration of Fe^{2+}. The solution underwent pH titration using NaOH until a pH of approximately six was reached. The solubility of Fe and Li salts was monitored as a function of pH. The samples were then collected for further analysis. Vacuum filtration was performed, and the filtrate was analyzed using ICP-OES. Different precipitation methods were tested, including hydroxide, sulfide, and oxalate precipitation. In hydroxide precipitation, sodium hydroxide (NaOH) was added to increase pH and precipitate Fe as $Fe(OH)_2$ according to the reaction:

$$Fe_2 + + NaOH \rightarrow Fe(OH)_2 + Na^+ \quad (1)$$

The solution was stirred at 150–250 rpm, and the resulting precipitate was filtered and analyzed. Sulfide precipitation utilized sodium sulfide (Na2S), which reacted with Fe2+ to form FeS. The mixture was then stirred under the same conditions before being filtered. Sodium sulfide (Na_2S) was tested as a precipitating agent due to its solubility in water and strong affinity for Fe^{2+}. The reaction followed:

$$Fe_2 + + Na_2S \rightarrow FeS + 2Na^+ \quad (2)$$

For oxalate precipitation, oxalic acid ($H_2C_2O_4 \cdot 2H_2O$) was added in different amounts (stoichiometric, +45%, +21%, -40%) to evaluate efficiency, forming FeC_2O_4, which was filtered and analyzed after 1 hour of stirring. The reaction followed:

$$Fe^{2+} + H_2C_2O_4.2H_2O \rightarrow FeC_2O_4 + 2H_3O^+ \quad (3)$$

5.2.3 Analytical Methods

During the experiments, ICP-OES was utilized to measure metal concentrations in both liquid and solid samples. XRF Spectroscopy was used for non-destructive elemental analysis of the solid phase. These techniques offered both quantitative and qualitative insights into the composition of the spent batteries and leaching residues.

5.3 Results and Discussion

5.3.1 Preliminary leaching experiments

The elemental composition of the Al foil obtained from spent $LiFePO_4$ cathodes was analyzed using ICP-OES, and the results showed that the average content of Al, Fe, and Li were 10.2%, 26.7%, and 3.8%, respectively. These values will serve as a reference for calculating leaching yields.

Preliminary leaching tests were conducted to determine the most effective acid for metal extraction. The extraction yields were calculated from initial and final metal concentrations using ICP-OES [131], as represented in the following equation.

$$\eta = \frac{mg\ (extracts)}{mg_{in}}\ 100 \tag{4}$$

Fig. 1 summarizes the leaching yield results for Li, Fe, and Al using different acids. H_2SO_4 showed the highest Li extraction (74%), with a moderate Fe yield (76.7%), while Al extraction was negligible. In contrast, the HNO_3 exhibited a slightly higher extraction of Fe (82.5%), but the recovery of Li was lower (65%). Organic acids such as oxalic, citric, and acetic acids resulted in significantly lower Li yields (4%–27%), confirming that H_2SO_4 is the most suitable leaching agent for Li recovery while minimizing Al dissolution. Additionally, precipitate formation was observed in some leaching solutions, particularly with acetic acid, sulfuric acid, hydrochloric acid, and HNO_3. XRF analysis of the solid residues revealed Fe and P content, attributed to the presence of iron phosphates in the spent cathodes, which explains the observed precipitation.

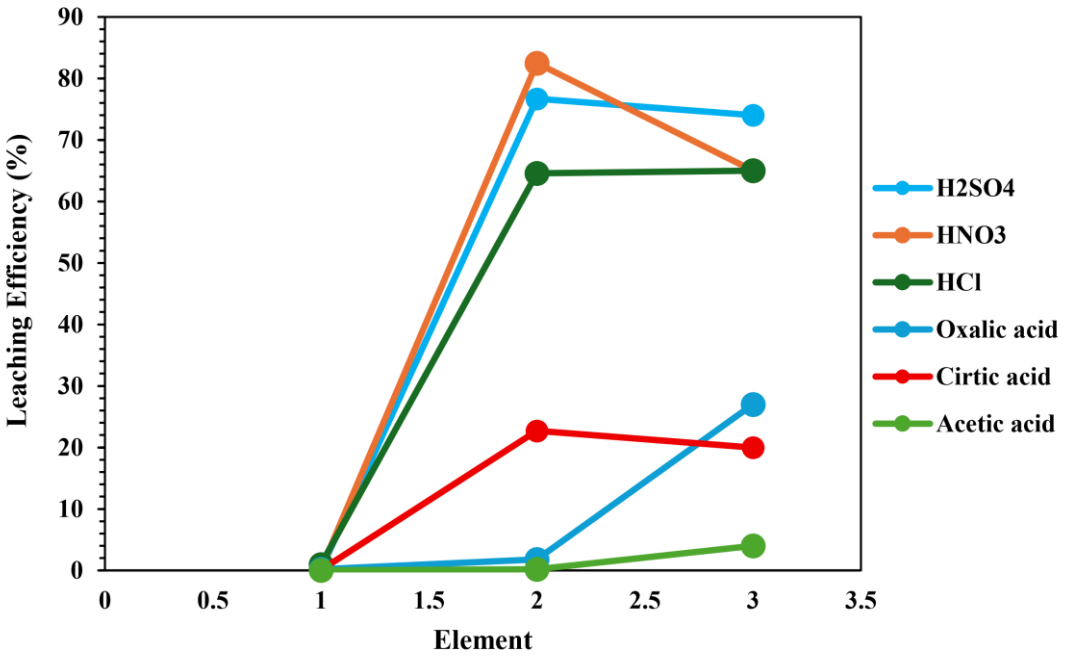

Figure 3: *Effect of different acids on the leaching yield percentage of Li, Al, and Fe*

5.3.2 Effect of different parameters on the leaching efficiency of lithium

Following the preliminary tests, a full factorial design was used to optimize the leaching conditions for Li extraction (Table 2). The effects of sulfuric acid concentration (A: 0.5–1.5 N), agitation speed (B: 150–350 rpm), and solid-to-liquid ratio (C: 5–15%) were studied using the Yates method.

Table 2: *Factors and levels for factorial planning*

FACTORS		LEVELS		
		-1	0	+1
Sulfuric acid	A	0.5 N	1 N	1.5 N
Agitation	B	150 rpm	250 rpm	350 rpm
Solid to liquid ratio	C	5 %	10%	15%

Before evaluating the effects of the studied variables, the experimental data were subjected to analysis of variance (ANOVA) to determine the statistical relevance of each factor and their interactions on Li leaching efficiency. The table below is the yield of different elements at different reaction conditions and combinations.

Table 3: *Leaching yield of Li, Fe and Al*

	A	B	C	Yield Li	Yield Al	Yield Fe
(1)	-1	-1	-1	41.77%	0.11%	0.46%
A	1	-1	-1	77.98%	0.47%	0.84%
B	-1	1	-1	58.40%	0.15%	0.68%
AB	1	1	-1	74.97%	0.43%	0.89%
C	-1	-1	1	21.76%	0.06%	0.28%
AC	1	-1	1	37.81%	0.30%	0.35%
BC	-1	1	1	22.74%	0.09%	0.22%
ABC	1	1	1	79.90%	0.28%	0.76%
Replications at the central point				4.15	0.02	4.48
I	0	0	0	73.59%	0.11%	0.77%
II	0	0	0	74.19%	0.18%	0.83%
III	0	0	0	67.84%	0.16%	0.84%

As the ANOVA is typically used to assess the significance of the model through p-values, where a value <0.05 confirms the statistical significance of a factor. Based on ANOVA results, a mathematical model can be developed to further understand leaching process behaviour under different conditions. A mathematical model can be developed using ANOVA results. This model estimates connection between dependent variable (leaching efficiency) and independent variables (Solid-to-liquid ratio, agitation speed, and acid concentration). Usually, a response surface methodology (RSM) is applied for this purpose. As shown in Table 4, this statistical study shows that all factors, including acid concentration, solid-to-liquid percentage, and agitation speed, have a significant impact on the leaching efficiency of Li. It means that the extracted Li from the material during leaching is dependent on any change in the above variables.

In RSM, a first- or second-order polynomial (linear or quadratic), shown in the following equations, is used to approximate the relationship between experimental parameters and response variables in small design spaces where a continuous and smooth response surface is expected. These models are relatively simple but chosen because it can still capture the curvature and interactions in the system within a localized experimental region.

$y = \beta_0 + \sum_{i=1}^{k} \beta_i X_i$ (first-order polynomial)

$y = \beta_0 + \sum_{i=1}^{k} \beta_i X_i + \sum_{i=1}^{k} \beta_{ii} X_i^2 + \sum_{i=1}^{k-1} \sum_{j=2}^{k} \beta_{ij} X_i X_j$ (second-order polynomial)

In such model, the independent variables are coded according to the following equation (5)

$$X = \frac{x_i - x_0}{\Delta x} \quad (5)$$

Where $i = 1,2, \ldots, k$ and X are the dimensionless value of a variable, x_i is the actual value of a variable, x_0 is the value of X at the centre point, and Δx is the step change. Using this approach a model was developed to predict Li leaching efficiency (equation 5).

The equation (6) describes the behaviour of the response, Li extraction yield, as a function of the significant factors (coded variables).

$$Li\ (\%) = 51.92 + 15.75A + 7.09B - 11.36C + 7.59ABC \quad (6)$$

The constants in the final regression model revealed a notable increase in leaching efficiency with high acid concentration and agitation speed, but a decrease in efficiency with a higher solid-to-liquid ratio. The final model confirms its reliability with $R^2 = 0.94$, which means strong predictive capability and insignificant lack of fit.

***Table 4**: Analysis of variance for Li leaching efficiency results*

Source	Sum of Squares	df	Mean Square	F-value	p-value	
Model	3880.3	4	970.08	19.98	0.0028	significant
A-Sulfuric Acid	1984.19	1	1984.19	40.86	0.0014	
B-Agitation	401.72	1	401.72	8.27	0.0347	
C-Solid to liquid	1033.08	1	1033.08	21.28	0.0058	
ABC	461.32	1	461.32	9.5	0.0274	
Curvature	868.99	1	868.99	17.9	0.0082	
Residual	242.79	5	48.56			
Lack of Fit	218.21	3	72.74	5.92	0.148	not significant
Pure Error	24.58	2	12.29			
Cor Total	4992.08	10				
			Fit Statistics			
Std. Dev.	6.97		**R^2**	0.9411		
Mean	57.36		**Adjusted R^2**	0.894		

C.V. %	12.15	**Predicted R^2**	0.6102
		Adeq Precision	10.7336

Figure 2 demonstrates the effect of different parameters on the leaching efficiency of Li. Figure 2(a) is a 3D surface plot that shows a significant increase in Li recovery with the increase in acid concentration and agitation speed. In Figure 2(b), it is confirmed from perturbation plot that by following agitation, sulfuric acid has a significant positive effect, and the solid-to-liquid percentage has a negative impact on leaching. According to Figure 2(c), the model has strong accuracy, as the data points are aligned closely to the diagonal line in the predicted vs. actual plot.

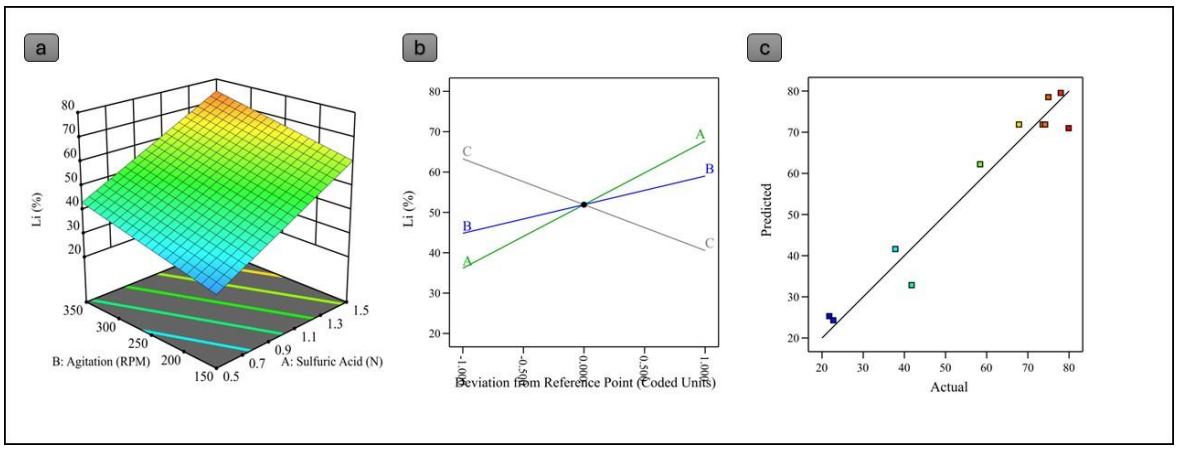

Figure 4:*(a) 3D surface plot of acid concentration and agitation speed on lithium leaching (b) the perturbation plot (c) model accuracy by predicted vs actual plot*

5.3.3 Effect of different parameters on Fe leaching efficiency

The following ANOVA analysis illustrates the impact of various parameters on Fe leaching efficiency. The sulfuric acid concentration and agitation speed have a positive effect on leaching, while an increase in the solid-to-liquid ratio lowers the leaching efficiency. The model has (R^2=0.9925) and not significant lack of fit, which confirms the accuracy of the model.

Table 5: *Analysis of variance for Fe leaching efficiency results*

Source	Sum of Squares	df	Mean Square	F-value	p-value	
Model	4889.5	5	977.9	105.24	0.0002	significant

A-Sulfuric Acid	1800	1	1800	193.72	0.0002	
B-Agitation	480.5	1	480.5	51.71	0.002	
C-Solid to liquid	1984.5	1	1984.5	213.58	0.0001	
AB	112.5	1	112.5	12.11	0.0254	
ABC	512	1	512	55.1	0.0018	
Curvature	1400.24	1	1400.24	150.7	0.0003	
Residual	37.17	4	9.29			
Lack of Fit	8.5	2	4.25	0.2965	0.7713	not significant
Pure Error	28.67	2	14.33			
Cor Total	6326.91	10				

Fit Statistics			
Std. Dev.	3.05	**R^2**	0.9925
Mean	62.91	**Adjusted R^2**	0.983
C.V. %	4.85	**Predicted R^2**	0.9593
		Adeq Precision	28.3759

The equation (7) describes the behaviour of the response, iron extraction yield, as a function of the factors.

$$Fe = 56 + 15A + 7.75\,B - 15.75C + 3.75\,AB + 8ABC \quad (7)$$

Figure 3 illustrates the effect of parameters and model fitting results on Fe leaching. In Figure 3(a), the 3D surface plot indicates a positive correlation between acid concentration and agitation speed, as well as their combined effect on leaching efficiency. The perturbation plot in Figure 3(b) shows that Fe recovery is strongly affected by both sulfuric acid concentration, solid-to-liquid ratio and agitation speed. Figure 3(c) is the predicted vs actual plot, showing a good correlation with the diagonal line and confirming predictive accuracy of the model for optimization of the process.

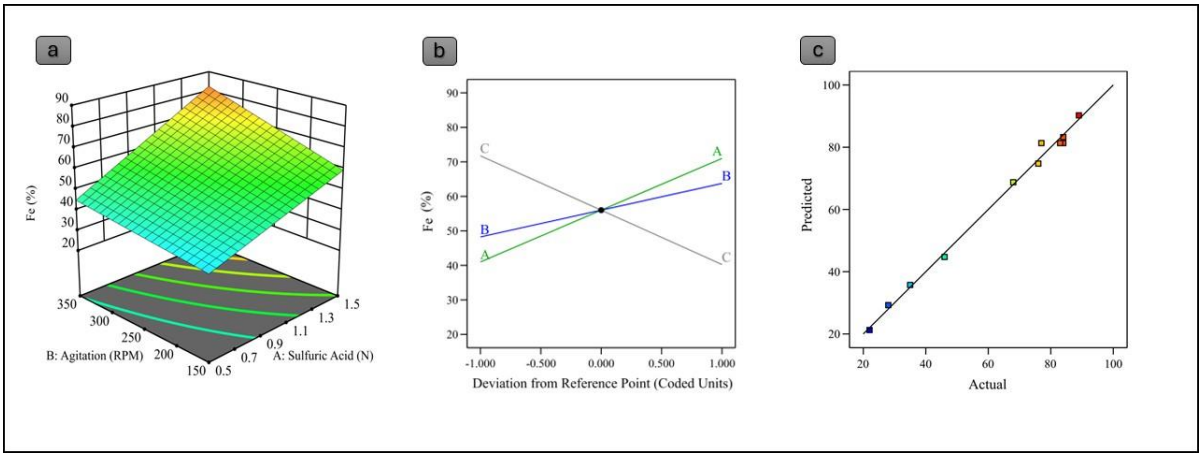

Figure 5:*(a) 3D surface plot of acid concentration and agitation speed on Fe leaching (b) the perturbation plot (c) model accuracy by predicted vs actual plot*

5.3.4 Effect of different parameters on the leaching efficiency of Aluminium

The statistical analysis reveals that the selected parameters explain the variability in response and confirm a significant model with an R^2 of 0.9725 and a low lack of fit ($p < 0.0001$) for Al leaching efficiency. It also indicates that sulfuric acid concentration is the most critical influencer for leaching efficiency, and the solid-to-liquid ratio has a negative impact.

Table 6: *Analysis of variance for Al leaching efficiency results*

Source	Sum of Squares	df	Mean Square	F-value	p-value	
Model	0.1717	3	0.0572	70.82	< 0.0001	Significant
A-Sulfuric Acid	0.1431	1	0.1431	177.05	< 0.0001	
C-Solid to liquid	0.0231	1	0.0231	28.59	0.0017	
AC	0.0055	1	0.0055	6.82	0.04	
Curvature	0.0162	1	0.0162	20.08	0.0042	
Residual	0.0049	6	0.0008			
Lack of Fit	0.0023	4	0.0006	0.4327	0.7848	not significant
Pure Error	0.0026	2	0.0013			
Cor Total	0.1928	10				
Fit Statistics						
Std. Dev.	0.0284	**R^2**		0.9725		
Mean	0.2127	**Adjusted R^2**		0.9588		

C.V. %	13.37	**Predicted**	0.9159
		R^2	
		Adeq	
		Precision	

The equation (8) describes the behaviour of the response, aluminium extraction yield, as a function of the significant factors.

$$Al = 0.236 + 0.134A - 0.054C - 0.026AC \quad (8)$$

Figure 4 illustrates the effect of parameters and statistical modelling results on aluminium leaching. The 3D surface plot in Figure 4(a) shows that the aluminium leaching efficiency increased with acid concentration, and the solid-to-liquid ratio has an interactive impact. Figure 4(b) shows the separate effects of all parameters in the perturbation plot, indicating that the solid-to-liquid ratio decreases leaching, while acid concentration has a positive impact. The reliability and accuracy of the model can be confirmed from the predicted vs. actual plot in Figure 4(c), as the data points are closely aligned along the diagonal line.

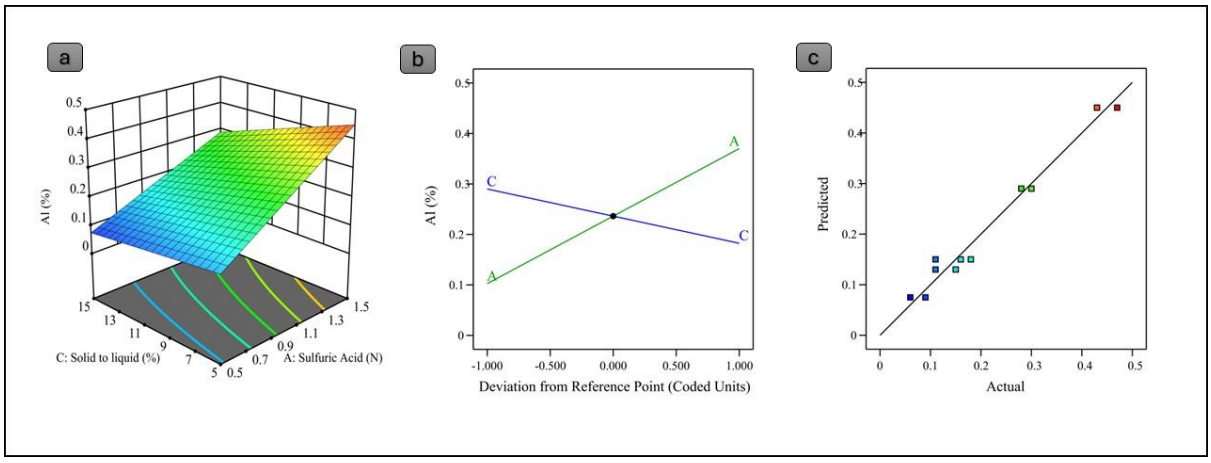

Figure 6:*(a) 3D surface plot of acid concentration and agitation speed on aluminium leaching (b) the perturbation plot (c) model accuracy by predicted vs actual plot*

5.3.5 Optimal Conditions for Leaching

The analysis of factorial design revealed the key factors for maximizing Li recovery while limiting the Al dissolution. However, there was a negative correlation between agitation speed (B = 350 rpm) and solid-liquid-ratio (C =15%) with Li extraction efficiency. Still, these parameters were retained to meet industrial scalability requirements, as they enable processing of the maximum practical volume of solid feedstock. In contrast, the regression model

determined that an H_2SO_4 concentration of 1.5 N (A) was optimal, achieving nearly complete Li recovery (≈100%) while restricting the Al dissolution below 1%. This threshold is critical for reducing downstream purification costs. For the validation of this model, A separate leaching test has been carried out in according to these conditions i.e. A = 3 N, B = 350 rpm, C = 20%, and table 7 below shows the results obtained according to the model (Model response) and those obtained experimentally by carrying out a further leaching test in the optimal conditions found (Experimental Response). The results showed excellent agreement with predictions as presented in Table 2, which confirms the effectiveness of the factorial design approach for optimizing industrial processes.

Table 7: *Comparison of Model and Experimental Response at Optimal Leaching Conditions*

Factors	**Optimized Conditions**	**Model Response**	**Experimental Response**	**Extracted Metals**
A [N]	3	99.2	90.8	Li
B[rpm]	350	0.77	2.0	Al
C [%]	20	91.8	98.0	Fe

The experimental results presented in Table 7 closely align with the model predictions, confirming that the extraction yields of Li are above 90%. However, slight deviations from the expected results may be due to process variability, or minor experimental uncertainties.

5.3.6 Precipitation Analysis

To determine the feasibility of selective precipitation of metals from the obtained leaching liquor, precipitation tests were conducted by gradually increasing the pH using NaOH as the precipitating agent, and monitoring the precipitation behaviour of Fe and Li. After the completion of precipitation tests, the yield calculations were performed using the following equation [27]:

$$\eta = \frac{C_s - C_f}{C_s} \times 100 \quad (9)$$

Where C_s and C_f represent the initial and final concentrations, respectively. The results shown in Figure 5 demonstrate that Fe completely precipitates at neutral pH, but Li also exhibited significant precipitation, indicating that NaOH is not suitable for selective precipitation.

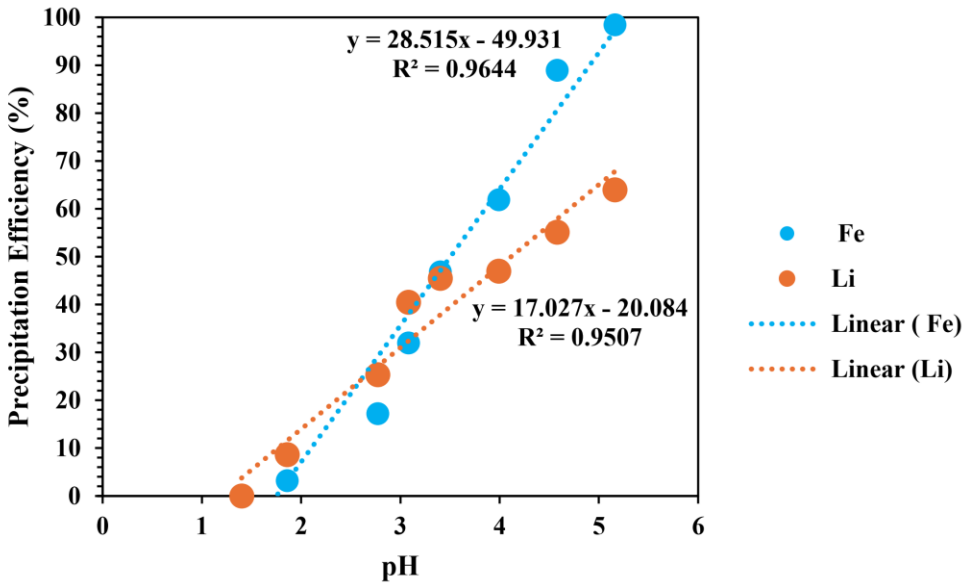

Figure 5: *Effect of varying pH with NaOH on the precipitation behaviours of Fe and Li*

Further tests with sodium sulphide were performed using three different amounts: stoichiometric, sub-stoichiometric (-20%), and highly deficient (-50%), and the results were summarized in Fig. 6.

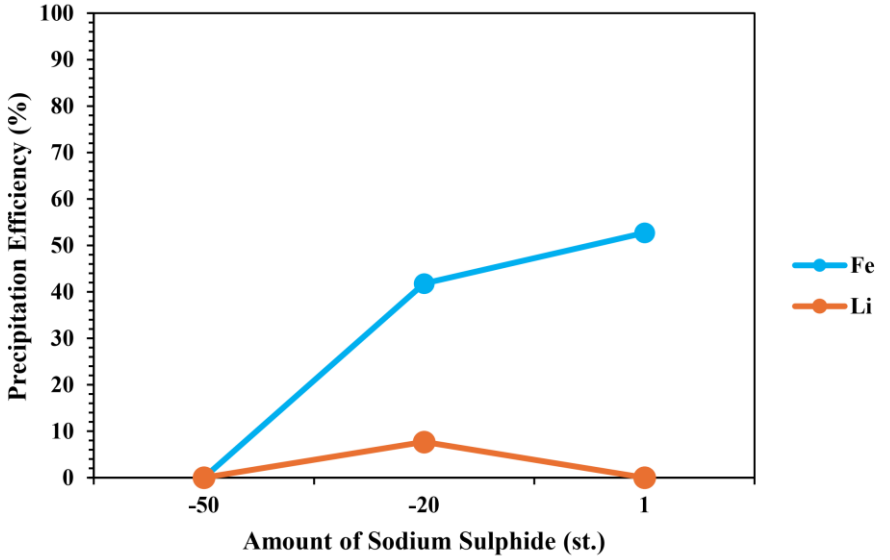

Figure 6*: Effect of sodium sulphide amount with respect to the required stoichiometric value on the precipitating behaviours of Fe and Li*

The results shown in Figure 6 revealed a strong dependency of precipitation efficiency on the amount of sodium sulphide. No precipitation occurred at -50% of the stoichiometric ratio of sodium sulphide, while increasing the sodium sulphide to -20% of the stoichiometric ratio significantly improved Fe precipitation efficiency to above 40%. Further increasing the amount to the full stoichiometric ratio resulted in a lower rate of improvement in precipitation efficiency. The results also indicated that Li precipitation was negligible, demonstrating a high selectivity for Fe precipitation over Li. The highest Fe precipitation efficiency, approximately 53%, was achieved at the maximum sodium sulphide level. This confirmed that sulphide addition does not achieve satisfactory precipitation efficiency.

Finally, precipitation using oxalic acid was tested with varying stoichiometric dosages, calculated considering dehydrated oxalic acid. After oxalic acid precipitation, the filtered solutions were analysed for Fe and Li content, and the precipitation efficiencies were calculated. The results are shown in Figure 7. As can be seen, oxalic acid precipitation demonstrated the best selectivity and efficiency simultaneously. At stoichiometric levels, Fe precipitation reached 98.1% while Li remained low (2%). Increasing or decreasing the oxalic acid concentration slightly affected Li precipitation, but Fe removal remained high in all cases.

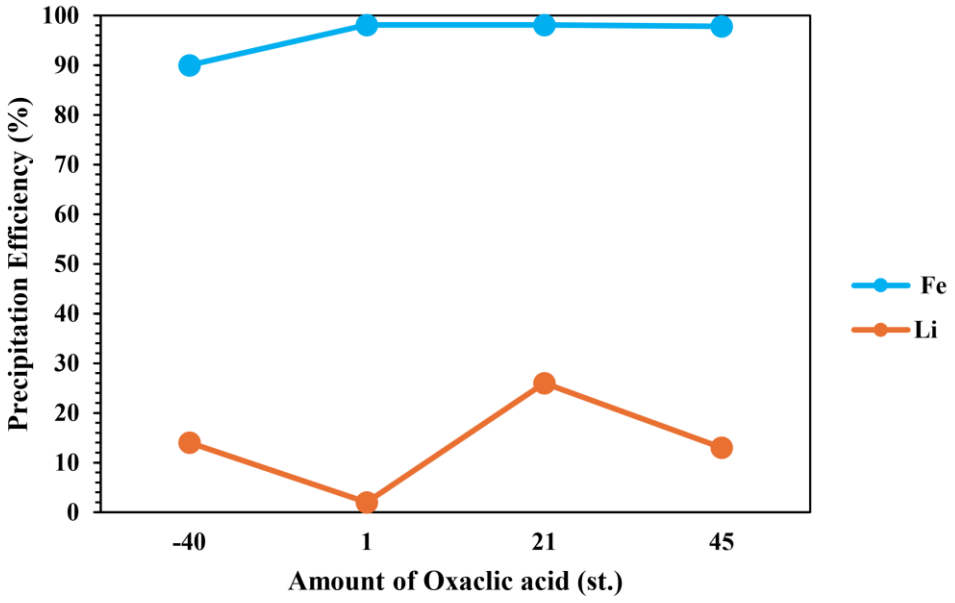

Figure 7: *Effect of oxalic acid amount with respect to the required stoichiometric value on the precipitating behaviours of Fe and Li.*

These results suggest that oxalic acid precipitation is the most promising approach for Fe separation, whereas NaOH and sulphide methods lack sufficient selectivity and efficiency for effective Fe-Li separation. A detailed mass balance was performed under the optimal conditions for oxalic acid precipitation for the evaluation of Li and Fe separation. Assuming 1000 mg of Fe is present in 1 L volume of leachate, along with 500 mg of Li. Using (1× dosage) stoichiometric oxalic acid resulted in the selective separation of Fe (98.1%) and Li (only 2%). This indicates that Fe (981 mg) and Li (10 mg) are gone in the solid phase while 19 mg of Fe and 490 mg of Li are retained in the remaining solution. The process shows a good selectivity with 49.05 Fe/Li selectivity ratio and 98% Li recovery in the liquid phase. It also confirms that the oxalic acid is suitable for removing Fe selectively and conserving Li for the recovery process.

5.4 Conclusions

In this study, the hydrometallurgical recovery of Li and Fe from spent $LiFePO_4$ batteries was successfully optimized. The process combined efficient leaching with selective precipitation to achieve high recovery rates. Preliminary leaching tests identified H_2SO_4 as the most effective leaching agent, achieving 74% Li recovery with minimal Al dissolution, making it superior to the other inorganic and organic acids evaluated. Along this, elemental analysis of the spent cathode foil showed the presence of Al (10.2%), Fe (26.7%), and Li (3.8%), which provided the basis for calculating metal extraction yields.

A factorial design approach was applied to develop a statistical model for predicting Li extraction efficiency based on key process variables. The optimized conditions, i.e., H_2SO_4 (3 N), 350 rpm agitation, and a 20% solid-to-liquid ratio, revealed a high Li recovery (~90.8%), minimal Al dissolution (2.0%), and excellent Fe recovery (98.0%). These findings highlight the effectiveness of factorial design in optimizing leaching parameters.

Selective precipitation studies were also performed to remove Fe while retaining Li in solution. NaOH and sulphide precipitation methods showed low selectivity and efficiency, whereas oxalic acid precipitation at stoichiometric levels achieved 98.1% Fe removal with only 2% Li loss. These results demonstrate that oxalic acid is the most effective reagent for Fe–Li separation, enabling high-purity recovery of both metals for potential reuse in battery production. Future research should focus on further refining selective separation techniques and assessing the economic feasibility of large-scale implementation, ensuring sustainable resource recovery for the circular economy.

CHAPTER 6

Investigation of Graphite Recovery from Black Mass of Spent Alkaline Batteries Using Hydrometallurgical Separation Processes

6.1 Introduction

The critical raw materials, also known as CRMs, are considered critical due to their supply risk or strategic characteristics and have an influence or importance on economic development. These materials can be extracted from primary sources, such as mining, and from secondary sources, like resource recovery from urban waste or waste dumps[132]. Over the last decades, intensive studies have been made to recover these CRMs from waste or e-waste, especially on spent battery recovery due to their high demand and extensive usage[133]. The black mass is the fraction of spent alkaline and Zn/C, consisting of two CRMs, including 26-45% of Mn, and 5-8% of graphite, along with base metals such as 12-28% of Zn[134].

There are three main routes for the recovery of compounds or metals from the black mass, including hydrometallurgy, pyrometallurgy, and direct recycling[135], [136], [137]. The choice of a suitable recycling technique is the key factor for the valuable or targeted material recovery during the recycling process to make it economical, optimized, and technologically feasible[138]. For example, during the pyrometallurgical recovery of Zn, graphite might be damaged or lost due to the high temperature range of 500-700°C[139].

There has been an increased interest in graphite recovery over recent years due to its wide range of current and future applications[140]. Almost 75% of natural graphite from other countries is imported by the European Union, including Madagascar (6%), Mozambique (13%), Brazil (14%), and China (41%)[141]. Natural graphite has unique properties, such as thermal and electrical conductivity, and high mechanical strength and stability, making it a good choice for a vast range of applications.

Graphite is the allotropic form of carbon, having sp^2 hybridized carbon atoms with p-electrons[142]. Graphite can be found either as natural or synthetic graphite, and the quality is based on the size and percentage of total graphitic carbon[143]. It is observed that the graphite in the residual of the recycled batteries still retains an ordered graphitic structure, and thus recycling of this graphite can lower the manufacturing cost, as no further processing is needed[144].

This chapter includes a detailed study of graphite recovery from spent alkaline batteries. This work was done under the LIFE-GRAPhiREC project, and the samples were provided by SIMA industry. In this work, the alkaline spent batteries' black mass is first converted to exhausted alkaline black mass (EABM) before the hydrometallurgical treatment.

6.2 Materials and Methods

6.2.1 Sample Collection

The sample used in this study is the black mass (BM) fraction of the spent alkaline battery scrap. This black mass was then converted to exhausted black mass after leaching and referred to as EABM. The sample was then characterized and used for further treatments to get purified graphite.

6.2.2 Chemicals and Standards

All the reagents used were of analytical grade. The chemicals used are Sulfuric acid (H_2SO_4), Citric Acid $C_6H_8O_7$, Hydrogen Peroxide (H_2O_2), and Hydrochloric Acid (HCl). The clean glassware was used to carry out all the tests. The distilled water was used to prepare all solutions and the filtration process.

6.2.3 Instruments and Analysis

A vacuum filtration system was used to filter the solutions. A pH meter with probes inside the reactors. ICP-OES was used to find the concentration of the elements in the solution. An XRD technique was applied to find the crystallinity of the impure and pure samples. Moreover, some other analytical methods, such as particle size distribution (PSD), thermogravimetric analysis (TGA), CHNS-Analysis, and X-ray fluorescence (XRF), were also used.

6.2.4 Leaching

In the first step of leaching, the black mass was converted into exhausted black mass using sulfuric acid. This step is useful to remove most of the elements like K, Mn, Zn, leaving behind more graphite in the sample. The second step of leaching is to purify the graphite from other impurities using different leaching conditions and chemical combinations.

6.2.5 Safety Measurements

All the leaching experiments and chemicals were carefully used under the fume hood with proper PPE. All the solid residues and chemical waste were carefully disposed of according to the protocols. The acid wastes were normalized to a pH of 6-8 before disposal.

6.3 Results and Discussion

6.3.1 Characterization of the Input material

In this section, the characterization of the input materials, which is exhausted alkaline black mass (EABM) and is provided by SIMA, was carried out. Various analytical techniques, including XRD, XRF, ICP, PSD, and TGA, were employed to evaluate the variability of the input materials.

6.3.1.1 Preparation of exhausted alkaline black mass (sample 1)

The chemical composition of the as-received sample, which is black mass (BM), is represented in Table 1, determined through chemical digestion in aqua regia followed by analysis using ICP-OES (Agilent Technologies 5100).

Table 1. Chemical composition of the as-received sample (BM) measured by ICP.

Element	**Mn**	**Zn**	**K**	**Na**	**Ba**	**Fe**	**Ca**
Wt. %	34.92	22.38	4.58	0.29	0.23	0.21	0.09

The initial sample received from SIMA was not an exhausted alkaline black mass (EABM), but rather black mass (BM) (1 kg). The sample (BM) was initially treated to produce EABM. To achieve this, leaching experiments were conducted using sulfuric acid solutions to remove most of the zinc, potassium, and manganese oxides. The results of these experiments are presented in Table 2. Based on the findings from Table 2, a 1.5 M sulfuric acid solution was selected for the treatment of the entire BM sample, and the results are shown in Table 3. Approximately 52% weight loss occurred following the leaching pretreatment. The resulting material is referred to as EABM-1 throughout this text.

Table 2. Leaching experiments to treat the initial sample of BM to achieve EABM-1.

Leaching conditions				**Leaching efficiency (%)**				
T (°C)	t (h)	S/L (%)	H_2SO_4 Conc. (M)	Mn	Zn	K	Na	Fe
25	2	20	1	20.73	73.88	65.58	74.33	5.30
25	2	20	1.5	26.02	85.99	70.10	52.88	25.84
25	2	20	2	24.31	80.45	66.35	67.80	42.93
25	2	20	2.5	25.79	86.00	69.59	60.33	32.31

Table 3. Weight loss after leaching of BM using 1.5M sulfuric acid solution, according to the conditions reported in Table 2.

Initial mass of BM (g)	Final mass (EABM-1) (g)	Weight loss (%)
911.08	441.20	51.57

6.3.1.2 XRD Analysis

The resulting EABM-1 sample was characterized using XRD (Philips Panalytical instrument) to identify its major phases (Figure 1). The analysis revealed that the primary constituents are graphite and MnO_2.

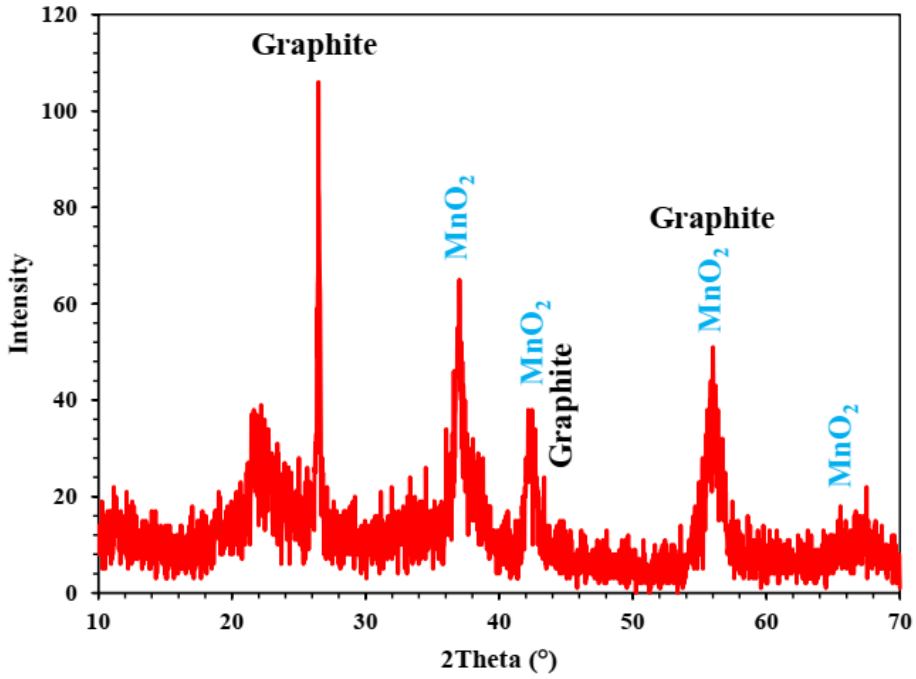

Figure 1. XRD pattern of EABM-1.

6.3.1.3 XRF Analysis

The obtained EABM-1 sample was also analysed using XRF to identify the main impurities. The results are presented in Table 4, indicating that the primary impurities include Na, Si, S, K, Ti, Mn, Fe, Zn, and Ba.

Table 4. XRF results for EABM-1.

Element	(%)	Element	(%)	Element	(%)
Na	0.441	As	0.01982	Nd	<0.00020
Mg	<0.0020	Se	<0.00005	HF	<0.00010
Al	0.03290	Br	0.00793	Ta	0.00521
Si	0.3003	Rb	<0.00005	W	<0.00010
P	<0.00030	Sr	0.01078	Hg	0.00208

S	0.7759	Y	0.00101	Tl	<0.00010
Cl	0.02584	Zr	0.00112	Pb	<0.00010
K	0.4176	Nb	<0.00010	Bi	0.00755
Ca	<0.0010	Mo	0.00025	Th	<0.00010
Ti	0.1334	Ag	0.00156	U	<0.00010
V	<0.00010	Cd	0.00008		
Cr	<0.00010	Sn	0.00612		
Mn	72.06	Sb	0.00075		
Fe	0.5544	Te	0.00172		
Co	<0.00030	I	<0.00030		
Ni	0.00769	Cs	<0.00040		
Cu	0.00307	Ba	0.5884		
Zn	1.127	La	<0.00020		
Ga	0.00395	Ce	<0.00020		
Ge	<0.00005	Pr	0.0972		

6.3.1.4 ICP Analysis and LOI (%)

To obtain more accurate impurity data, the EABM-1 sample was dissolved in aqua regia, and the resulting solution was analysed using ICP. This analysis was performed in four replicates to calculate the associated error. The results are presented in Table 5.

Table 5. Main impurities in EABM-1 determined by ICP.

Mn (%)	Zn (%)	K (%)	Na (%)	Fe (%)	Ba (%)	Ca (%)
48.22 ± 1.16	0.90 ± 0.03	0.60 ± 0.02	0.19 ± 0.002	0.40 ± 0.07	0.49 ± 0.005	0.04 ± 0.01

Table 6 presents the moisture content and loss on ignition (LOI) of the EABM-1 sample, determined by drying at 105 °C for 24 hours and heating at 600 °C for 1 hour, respectively. These measurements were also conducted in quadruplicate to assess variability and error.

Table 6. Moisture content and LOI of the EABM-1 sample.

Moisture (%)	LOI (%)
3.42 ± 0.74	21.12 ± 2.10

6.3.1.5 TGA-DTA Analysis

The EABM-1 sample was further characterized by TGA-DTA (LINSEIS STA PT 1600) to evaluate weight loss during heating. The sample was heated in air up to 1000 °C at a constant rate of 10 °C/min. The results are presented in Figure 2.

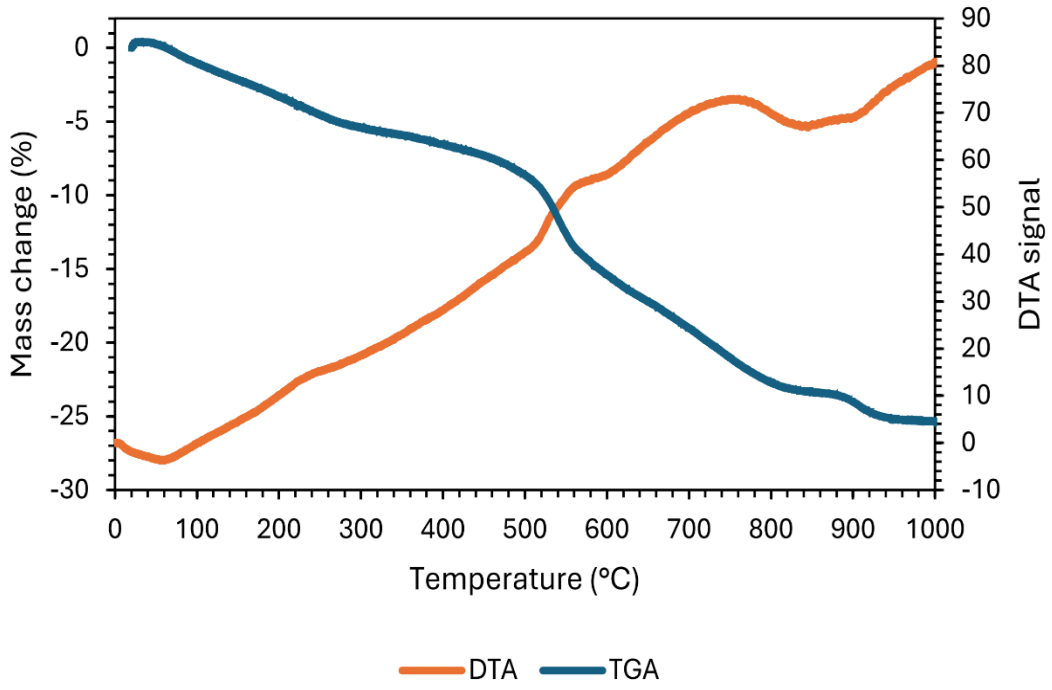

Figure 2. TGA-DTA graph of EABM-1 (heating rate of 10 °C/min in air)

6.3.1.6 CHNS analysis

CHNS analysis was conducted to determine the carbon content of the EABM-1 sample. As shown in Table 7, EABM-1 contains approximately 11% carbon.

Table 7. CHNS analysis results for EABM-1.

Run	Mass (mg)	C (%)	H (%)	N (%)	S (%)
1	3.97	11.1	0.8	0	0.79
2	1.96	10.88	0.55	0	0.7
Average		10.97	0.66	0	0.75

PSD analysis

The particle size distribution of the EABM-1 sample was analyzed using a Mastersizer 2000 (Malvern Instruments Ltd.). The results are presented in Table 8 and illustrated in Figure 3.

Table 8. PSD results for EABM-1.

	µm
D (0.1)	4.296
D (0.5)	28.817
D (0.9)	83.879

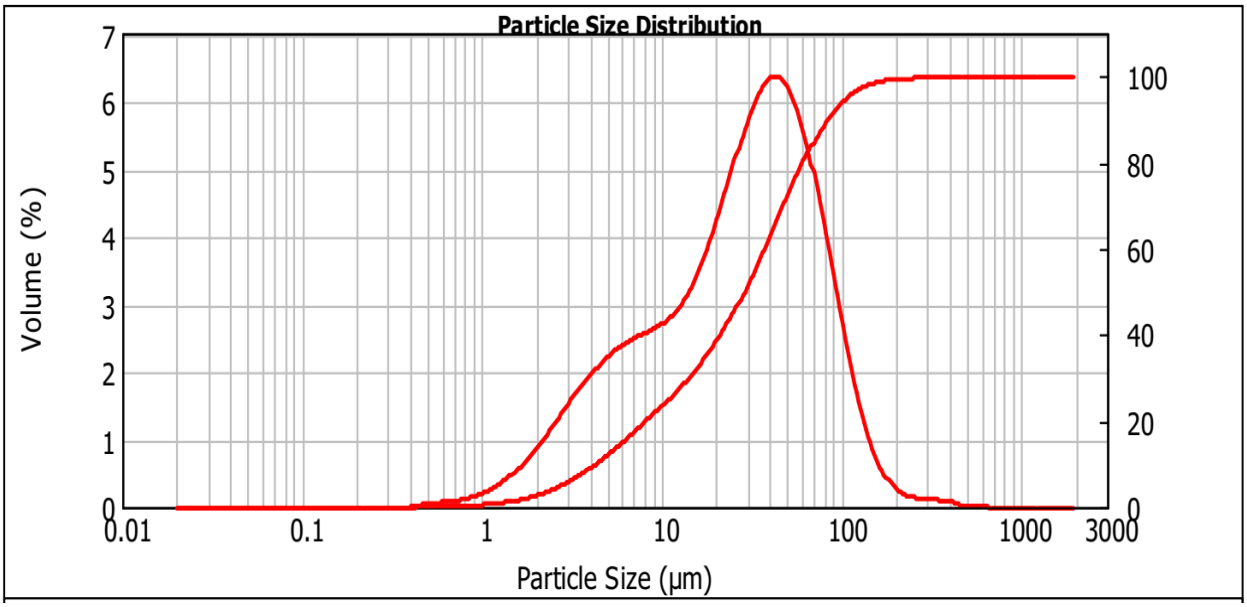

Figure 3. PSD of EABM-1.

6.3.2 Leaching purification experiments (EABM)

In this section, purification experiments were conducted to recover and purify graphite from the EABM-1 sample (Table 5), selected as a representative of the EABM group. Due to the partial dissolution of manganese oxides in sulfuric acid, a reducing agent is required to enhance the removal of manganese, particularly MnO_2, from EABM. Accordingly, binary systems comprising a strong acid (H_2SO_4 or HCl) and a reducing agent (H_2O_2 or citric acid, $C_6H_8O_7$) were evaluated as the primary purification systems.

6.3.2.1 Sulfuric acid and hydrogen peroxide system

As previously mentioned, MnO_2 is the main impurity in EABM and is insoluble in sulfuric acid alone. Therefore, a reducing agent is essential to facilitate its dissolution. Hydrogen peroxide, for instance, is an effective reducing agent for this purpose, as demonstrated by Equation 1.

$$MnO_2 + H_2SO_4 + H_2O_2 \rightarrow MnSO_4 + 2H_2O + O_2 \quad (1)$$

A series of experiments was designed using a fractional factorial design approach to assess the impact of key leaching parameters on impurity removal and graphite purification. Table 9 summarizes the parameter levels used in the leaching experiments. Each test was performed using 20 mL of solution. After leaching, all solids were dissolved in aqua regia and analysed by ICP to determine the impurity content.

Table 9. Levels of leaching parameters to recover and purify graphite in H_2SO_4 + H_2O_2 system.

Parameter	Level (-1)	Level (+1)

Temperature (°C)	30	60
Time (h)	1	3
H_2SO_4 Concentration (M)	1	2
H_2O_2 (30%) Concentration (%V/V)	5	10
S/L (%)	10	20

Table 10 and Table 11 present the conditions of purification experiments and the chemical composition of the final graphite, respectively. As shown in Table 11, the lowest impurity level was achieved in Run 7; however, a considerable amount of impurities remained. The main residual elements were Mn, Na, Fe, and Ba. Based on the initial barium content in EABM-1 (Table 5), it is likely that barium is present as barium sulfate, which is insoluble in sulfuric acid. This insolubility leads to its retention and accumulation in the final graphite product. Table 12 summarizes the leaching efficiency of each element across the 16 experiments.

Table 10. Leaching purification conditions to recover and purify graphite in H_2SO_4 + H_2O_2 system.

Run	Temperature (°C)	Time (h)	H_2SO_4 Conc. (M)	H_2O_2 (30%) Conc. (%V/V)	S/L (%)
1	60	3	2	5	10
2	30	3	1	5	10
3	30	3	2	5	20
4	60	1	2	5	20
5	60	3	1	5	20
6	30	1	1	5	20
7	60	3	1	10	10
8	60	1	1	10	20
9	30	1	1	10	10
10	30	3	2	10	10
11	60	1	2	10	10
12	60	1	1	5	10
13	30	1	2	5	10
14	30	3	1	10	20
15	30	1	2	10	20
16	60	3	2	10	20

Table 11. Chemical composition of the final graphite according to the conditions of Table 82 in H_2SO_4 + H_2O_2 system.

Run	Mn (%)	Zn (%)	K (%)	Na (%)	Fe (%)	Ba (%)	Ca (%)	Sum (%)
1	45.45	0.19	0.28	0.17	0.23	0.59	0.03	46.93
2	42.43	0.34	0.29	0.17	0.40	0.77	0.06	44.47
3	46.37	0.35	0.33	0.17	0.31	0.62	0.04	48.19
4	43.62	0.25	0.29	0.15	0.25	0.48	0.03	45.06
5	44.90	0.20	0.30	0.15	0.31	0.56	0.02	46.44
6	46.79	0.41	0.34	0.17	0.35	0.60	0.03	48.69
7	0.37	0.04	0.06	0.45	1.46	3.50	0.07	5.97
8	40.07	0.67	0.29	0.17	0.56	0.69	0.03	42.48
9	26.48	0.98	0.17	0.26	1.14	1.72	0.05	30.82
10	22.62	0.16	0.15	0.28	0.99	2.03	0.06	26.29
11	23.07	0.15	0.17	0.29	0.82	2.06	0.06	26.61
12	39.90	0.25	0.27	0.20	0.49	0.96	0.04	42.11
13	43.15	0.37	0.33	0.18	0.37	0.74	0.04	45.17
14	41.03	0.61	0.31	0.15	0.52	0.56	0.03	43.21
15	42.85	0.45	0.32	0.16	0.40	0.61	0.03	44.82
16	46.24	0.19	0.30	0.16	0.33	0.63	0.03	47.89

Table 12. Leaching efficiency of impurities in purification experiments of graphite (H2SO4 + H2O2 system).

Run	Mn (%)	Zn (%)	K (%)	Na (%)	Fe (%)	Ba (%)	Ca (%)	Weight loss (%)
1	29.51	87.47	54.07	18.97	47.53	0.08	62.31	27.5
2	48.34	81.21	63.69	32.83	23.52	0.09	49.04	43.25
3	24.45	74.33	47.14	17.40	22.89	0.05	39.64	23.125
4	18.73	80.79	47.19	13.91	32.23	0.04	43.51	19.525
5	25.22	85.61	50.14	20.54	21.44	0.04	58.11	24.05
6	20.21	60.67	38.75	14.80	10.57	0.03	44.31	24.35
7	99.89	99.44	98.19	59.64	37.12	0.19	80.72	86.35
8	56.49	66.38	68.53	40.79	0.90	0.07	64.44	49.975
9	85.24	73.78	89.23	52.73	0.91	0.15	73.68	73.45
10	89.78	96.66	92.61	58.67	35.62	0.20	78.36	77.8
11	89.00	96.75	91.50	56.85	43.49	0.23	79.55	77.2
12	59.95	88.58	71.28	39.74	25.81	0.08	70.29	52.25
13	44.05	79.23	57.14	27.49	26.54	0.09	57.42	37.6
14	52.27	66.34	64.19	38.58	0.51	0.07	60.79	46.025

15	47.25	75.75	60.31	34.27	24.16	0.06	55.84	41.625
16	47.39	89.92	63.82	35.48	41.04	0.05	53.96	44.025

All leaching data were statistically evaluated using analysis of variance (ANOVA). The ANOVA results for impurities are summarized in Table 13, where parameters with a p-value of less than 0.05 are considered significant in the leaching process. Non-significant parameters were excluded (except those required to support hierarchy); therefore, Table 13 presents only the significant parameters for impurity removal.

Table 14 presents the ANOVA fit statistics for the leaching efficiency of impurities in the purification experiments. The high R^2 values indicate a good model fit to the experimental data for each impurity element. Table 15 summarizes the final models for predicting the leaching efficiency of each element based on significant parameters.

Table 13. Analysis of variance for leaching efficiency of impurities in purification experiments of graphite (H_2SO_4 + H_2O_2 system).

Source	Sum of Squares	Degree of Freedom	Mean Square	F-Value	p-Value	
			Mn			
Model	10233.32	6	1705.55	58.37	< 0.0001	significant
A-Temperature	13.32	1	13.32	0.4558	0.5165	
C-H_2SO_4	206.32	1	206.32	7.06	0.0262	
D-H_2O_2	5507.58	1	5507.58	188.50	< 0.0001	
E-S/L	4024.27	1	4024.27	137.73	< 0.0001	
AC	198.94	1	198.94	6.81	0.0283	
DE	282.89	1	282.89	9.68	0.0125	
Residual	262.97	9	29.22			
Cor Total	10496.29	15				
			Zn			
Model	1993.35	11	181.21	108.79	0.0002	significant
A-Temperature	473.04	1	473.04	283.99	< 0.0001	
B-Time	218.02	1	218.02	130.89	0.0003	
C-H_2SO_4	216.68	1	216.68	130.08	0.0003	
D-H_2O_2	45.97	1	45.97	27.60	0.0063	
E-S/L	667.32	1	667.32	400.63	< 0.0001	
AC	52.68	1	52.68	31.63	0.0049	

BC	46.70	1	46.70	28.03	0.0061	
BD	25.88	1	25.88	15.54	0.0169	
CD	140.26	1	140.26	84.20	0.0008	
CE	38.11	1	38.11	22.88	0.0088	
DE	68.70	1	68.70	41.25	0.0030	
Residual	6.66	4	1.67			
Cor Total	2000.01	15				
			K			
Model	4614.04	3	1538.01	56.89	< 0.0001	significant
D-H_2O_2	2474.64	1	2474.64	91.54	< 0.0001	
E-S/L	1972.28	1	1972.28	72.96	< 0.0001	
DE	167.11	1	167.11	6.18	0.0286	
Residual	324.41	12	27.03			
Cor Total	4938.45	15				
			Na			
Model	3362.44	2	1681.22	61.53	< 0.0001	significant
D-H_2O_2	2287.73	1	2287.73	83.73	< 0.0001	
E-S/L	1074.72	1	1074.72	39.33	< 0.0001	
Residual	355.20	13	27.32			
Cor Total	3717.64	15				
			Fe			
Model	2879.72	4	719.93	14.98	0.0002	significant
A-Temperature	686.83	1	686.83	14.29	0.0030	
B-Time	264.47	1	264.47	5.50	0.0388	
C-H_2SO_4	1457.73	1	1457.73	30.32	0.0002	
E-S/L	470.69	1	470.69	9.79	0.0096	
Residual	528.78	11	48.07			
Cor Total	3408.50	15				
			Ba			
Model	0.0533	3	0.0178	51.02	< 0.0001	significant
D-H_2O_2	0.0172	1	0.0172	49.30	< 0.0001	
E-S/L	0.0297	1	0.0297	85.15	< 0.0001	
DE	0.0065	1	0.0065	18.61	0.0010	
Residual	0.0042	12	0.0003			
Cor Total	0.0575	15				

Ca						
Model	2538.81	8	317.35	61.12	< 0.0001	significant
A-Temperature	181.01	1	181.01	34.86	0.0006	
C-H_2SO_4	59.24	1	59.24	11.41	0.0118	
D-H_2O_2	941.23	1	941.23	181.29	< 0.0001	
E-S/L	1068.65	1	1068.65	205.83	< 0.0001	
AC	88.63	1	88.63	17.07	0.0044	
AD	71.45	1	71.45	13.76	0.0076	
CE	93.28	1	93.28	17.97	0.0038	
DE	35.31	1	35.31	6.80	0.0350	
Residual	36.34	7	5.19			
Cor Total	2575.16	15				

Table 14. Fit statistics of ANOVA for the leaching efficiency of impurities in purification experiments of graphite (H_2SO_4 + H_2O_2 system).

	Mn	**Zn**	**K**	**Na**	**Fe**	**Ba**	**Ca**
Std. Dev.	5.41	1.29	5.2	5.23	6.93	0.0187	2.28
Mean	52.36	81.43	66.11	35.17	24.64	0.0935	60.75
C. V. %	10.32	1.58	7.86	14.86	28.14	19.97	3.75
R^2	0.9749	0.9967	0.9343	0.9045	0.8449	0.9273	0.9859
Adjusted R^2	0.9582	0.9875	0.9179	0.8898	0.7885	0.9091	0.9698
Predicted R^2	0.9208	0.9467	0.8832	0.8553	0.6718	0.8708	0.9263
Adeq. Precision	23.2311	34.6917	18.1089	17.8079	13.2031	16.2492	24.7288

Table 15. Final models to predict the leaching efficiency of impurities in accordance with the significant parameters (H_2SO_4 + H_2O_2 system).

Parameters	**Coefficient**						
	Mn (%) =	Zn (%) =	K (%) =	Na (%) =	Fe (%) =	Ba (%) =	Ca (%) =
	-17.263	+63.925	+33.024	+23.884	-15.508	-0.057	-17.365
Temperature (°C)	+0.766	+0.725			+0.437		+1.118
Time (h)		+5.001			+4.066		
H_2SO_4 (M)	+13.975	-1.944			+19.090		+24.760
H_2O_2 (%V/V)	+12.467	-1.406	+8.853	+4.783		+0.037	+7.387
S/L (%)	-0.649	-0.974	-0.281	-1.639	-1.085	+0.003	+0.706
Temperature*Time							

Temperature*H_2SO_4	-0.470	-0.242			-0.314
Temperature*H_2O_2					-0.056
Temperature*S/L					
Time*H_2SO_4		-3.417			
Time*H_2O_2		+0.509			
Time*S/L					
H_2SO_4*H_2O_2		+2.369			
H_2SO_4*S/L		+0.617			-0.966
H_2O_2*S/L	-0.336	-0.166	-0.258	-0.002	-0.119

6.3.2.2 Sulfuric acid and citric acid system

6.3.2.2.1 Leaching experiments

Citric acid can also be used as a suitable reducing agent to assist the dissolution of manganese dioxide in the EABM according to Equation 2.

$$9MnO_2 + 9H_2SO_4 + C_6H_8O_7 \rightarrow 9MnSO_4 + 13H_2O + 6CO_2 \quad (2)$$

A series of experiments was designed using a fractional factorial design approach to investigate the effect of key leaching parameters on impurity removal from EABM and graphite purification, with citric acid serving as the reducing agent. Table 16 outlines the parameter levels used in the leaching experiments. Each test was conducted using 20 mL of solution. After leaching, all solids were dissolved in aqua regia and analysed by ICP to determine the impurity content.

Table 16. Levels of leaching parameters to recover and purify graphite in H_2SO_4 + $C_6H_8O_7$ system.

Parameter	Level (-1)	Level (+1)
Temperature (°C)	30	60
Time (h)	1	3
H_2SO_4 Concentration (M)	1	2
$C_6H_8O_7$ Concentration (M)	0.1	0.5
S/L (%)	10	20

Table 17 and Table 18 present the conditions of the purification experiments and the chemical composition of the final graphite, respectively. As shown in Table 18, the lowest impurity level was achieved in Run 6, although a notable amount of impurities remained. The predominant

residual elements were Mn, Na, Fe, and Ba. As previously mentioned, barium likely exists in the form of barium sulphate, which is insoluble in sulfuric acid, leading to its accumulation in the final graphite. Table 19 summarizes the leaching efficiency of each element across the 16 experiments.

Table 17. Leaching purification conditions to recover and purify graphite in H_2SO_4 + $C_6H_8O_7$ system.

Run	Temperature (°C)	Time (h)	H_2SO_4 Conc. (M)	$C_6H_8O_7$ Conc. (M)	S/L (%)
1	30	3	2	0.1	20
2	30	1	2	0.5	20
3	60	1	1	0.1	10
4	30	1	1	0.5	10
5	60	1	2	0.5	10
6	60	3	1	0.5	10
7	30	3	1	0.1	10
8	30	1	2	0.1	10
9	30	3	2	0.5	10
10	30	1	1	0.1	20
11	60	1	1	0.5	20
12	60	3	2	0.5	20
13	60	3	1	0.1	20
14	60	1	2	0.1	20
15	60	3	2	0.1	10
16	30	3	1	0.5	20

Table 18. Chemical composition of final graphite according to the conditions of Table 17 (H_2SO_4 + $C_6H_8O_7$ system).

Run	Mn (%)	Zn (%)	K (%)	Na (%)	Fe (%)	Ba (%)	Ca (%)	Sum (%)
1	43.72	0.18	0.29	0.18	0.35	0.58	0.06	45.35
2	38.79	0.13	0.24	0.19	0.47	0.80	0.04	40.67
3	39.62	0.12	0.23	0.23	0.60	1.24	0.03	42.07
4	39.90	0.14	0.25	0.21	0.44	0.87	0.04	41.87
5	2.60	0.04	0.08	0.43	1.27	3.45	0.06	7.93
6	0.44	0.04	0.07	0.43	1.39	3.40	0.08	5.85
7	42.18	0.16	0.27	0.19	0.38	0.72	0.04	43.94
8	43.38	0.19	0.28	0.17	0.30	0.48	0.03	44.83
9	17.92	0.06	0.11	0.28	1.07	2.06	0.13	21.63

10	44.76	0.21	0.30	0.19	0.33	0.65	0.03	46.47
11	37.20	0.90	0.22	0.26	0.64	1.20	0.07	40.48
12	3.38	0.27	0.09	0.36	1.40	3.08	0.17	8.74
13	41.74	0.15	0.27	0.20	0.51	0.85	0.03	43.76
14	41.74	0.14	0.27	0.22	0.38	0.92	0.03	43.71
15	24.76	0.06	0.14	0.29	0.81	2.05	0.04	28.14
16	33.16	0.24	0.22	0.24	0.60	1.34	0.04	35.84

Table 19. Leaching efficiency of impurities in purification experiments of graphite (H_2SO_4 + $C_6H_8O_7$ system).

Run	Mn (%)	Zn (%)	K (%)	Na (%)	Fe (%)	Ba (%)	Ca (%)	Weight loss (%)
1	41.29	89.34	62.78	20.17	33.47	0.12	40.35	38.22
2	62.52	94.15	77.23	38.90	33.48	0.03	52.94	54.75
3	70.79	96.02	83.34	44.60	34.29	0.03	79.10	64.85
4	58.51	93.30	72.58	28.75	32.97	0.04	67.59	50.85
5	99.27	99.43	97.78	61.16	46.07	0.41	82.59	86
6	99.88	99.47	97.91	61.23	41.46	7.76	73.29	86.4
7	48.92	91.41	67.00	21.25	33.17	0.03	45.64	43.45
8	39.10	87.92	57.56	12.23	34.95	0.04	49.87	33.75
9	92.68	98.99	95.25	62.04	39.17	3.13	52.89	80.45
10	31.47	85.99	55.23	11.27	26.20	0.02	41.43	29.47
11	68.03	63.75	81.61	37.02	17.28	0.04	36.18	58.47
12	99.00	96.46	97.87	65.87	38.60	0.11	48.32	85.87
13	50.89	92.45	69.26	27.32	7.35	0.02	51.48	45.65
14	54.94	93.17	72.76	29.14	41.48	0.41	58.25	48.57
15	88.52	98.86	93.06	55.64	48.52	0.45	84.65	76.8
16	76.96	92.43	84.84	46.87	33.34	0.02	54.92	66.6

All leaching data were statistically analysed using analysis of variance (ANOVA). The ANOVA results for impurity removal are summarized in Table 20, where parameters with a p-value less than 0.1 are considered statistically significant in the leaching process. Non-significant parameters were excluded (except those required to support hierarchy); therefore, Table 20 includes only the significant factors influencing impurity removal.

Table 21 presents the ANOVA fit statistics for the leaching efficiency of impurities in the purification experiments. The high R^2 values indicate a strong model fit to the experimental

data for each impurity element, with the exception of barium (Ba). Table 22 summarizes the final predictive models for leaching efficiency, based on the significant parameters identified for each element.

Table 20. Analysis of variance for leaching efficiency of impurities in purification experiments of graphite (H_2SO_4 + $C_6H_8O_7$ system).

Source	Sum of Squares	Degree of Freedom	Mean Square	F-Value	p-Value	
Mn						
Model	7275.59	5	1455.12	23.21	< 0.0001	significant
A-Temperature	2022.33	1	2022.33	32.26	0.0002	
B-time	805.02	1	805.02	12.84	0.0050	
C-H_2SO_4	322.93	1	322.93	5.15	0.0466	
D-$C_6H_8O_7$	3333.29	1	3333.29	53.17	< 0.0001	
E-S/L	792.02	1	792.02	12.63	0.0052	
Residual	626.86	10	62.69			
Cor Total	7902.45	15				
Zn						
Model	1106.36	13	85.10	60.38	0.0164	significant
B-time	130.38	1	130.38	92.50	0.0106	
C-H_2SO_4	118.24	1	118.24	83.88	0.0117	
E-S/L	207.68	1	207.68	147.34	0.0067	
AB	36.22	1	36.22	25.70	0.0368	
AC	52.42	1	52.42	37.19	0.0259	
AD	130.01	1	130.01	92.24	0.0107	
AE	91.36	1	91.36	64.82	0.0151	
BC	48.01	1	48.01	34.06	0.0281	
BD	48.20	1	48.20	34.20	0.0280	
BE	29.00	1	29.00	20.57	0.0453	
CD	83.97	1	83.97	59.57	0.0164	
CE	70.22	1	70.22	49.81	0.0195	
DE	60.65	1	60.65	43.03	0.0225	
Residual	2.82	2	1.41			
Cor Total	1109.18	15				
K						

Model	3172.41	5	634.48	18.91	< 0.0001	significant
A-Temperature	1026.62	1	1026.62	30.60	0.0003	
B-time	369.80	1	369.80	11.02	0.0077	
C-H_2SO_4	153.46	1	153.46	4.57	0.0582	
D-$C_6H_8O_7$	1427.47	1	1427.47	42.55	< 0.0001	
E-S/L	195.06	1	195.06	5.81	0.0366	
Residual	335.48	10	33.55			
Cor Total	3507.88	15				
			Na			
Model	4980.24	9	553.36	26.39	0.0004	significant
A-Temperature	1233.52	1	1233.52	58.83	0.0003	
B-time	591.81	1	591.81	28.22	0.0018	
C-H_2SO_4	279.17	1	279.17	13.31	0.0107	
D-$C_6H_8O_7$	2030.34	1	2030.34	96.83	< 0.0001	
E-S/L	309.29	1	309.29	14.75	0.0086	
AD	115.86	1	115.86	5.53	0.0570	
AE	197.49	1	197.49	9.42	0.0220	
BD	115.77	1	115.77	5.52	0.0571	
CD	107.00	1	107.00	5.10	0.0646	
Residual	125.81	6	20.97			
Cor Total	5106.05	15				
			Fe			
Model	1529.73	10	152.97	19.23	0.0022	significant
A-Temperature	4.32	1	4.32	0.5428	0.4944	
B-time	4.37	1	4.37	0.5497	0.4918	
C-H_2SO_4	502.41	1	502.41	63.14	0.0005	
D-$C_6H_8O_7$	32.88	1	32.88	4.13	0.0978	
E-S/L	393.94	1	393.94	49.51	0.0009	
AC	216.66	1	216.66	27.23	0.0034	
AE	168.14	1	168.14	21.13	0.0059	
BD	86.32	1	86.32	10.85	0.0216	
CD	39.53	1	39.53	4.97	0.0763	
CE	81.16	1	81.16	10.20	0.0242	
Residual	39.78	5	7.96			
Cor Total	1569.52	15				

Ba						
Model	52.40	9	5.82	4.26	0.0458	significant
A-Temperature	2.10	1	2.10	1.54	0.2616	
B-time	7.04	1	7.04	5.15	0.0636	
C-H_2SO_4	0.6678	1	0.6678	0.4889	0.5106	
D-$C_6H_8O_7$	6.79	1	6.79	4.97	0.0673	
E-S/L	7.73	1	7.73	5.66	0.0549	
AC	5.89	1	5.89	4.31	0.0832	
BD	6.74	1	6.74	4.94	0.0680	
BE	7.67	1	7.67	5.61	0.0556	
DE	7.78	1	7.78	5.70	0.0542	
Residual	8.20	6	1.37			
Cor Total	60.60	15				
Ca						
Model	3482.21	9	386.91	29.71	0.0003	significant
A-Temperature	732.23	1	732.23	56.23	0.0003	
B-time	16.83	1	16.83	1.29	0.2990	
C-H_2SO_4	25.54	1	25.54	1.96	0.2109	
D-$C_6H_8O_7$	20.13	1	20.13	1.55	0.2602	
E-S/L	1439.42	1	1439.42	110.53	< 0.0001	
AC	139.94	1	139.94	10.75	0.0169	
AD	442.59	1	442.59	33.99	0.0011	
AE	613.18	1	613.18	47.09	0.0005	
BE	52.35	1	52.35	4.02	0.0918	
Residual	78.14	6	13.02			
Cor Total	3560.35	15				

Table 21. Fit statistics of ANOVA for leaching efficiency of impurities in purification experiments of graphite (H_2SO_4 + $C_6H_8O_7$ system).

	Mn	**Zn**	**K**	**Na**	**Fe**	**Ba**	**Ca**
Std. Dev.	7.92	1.19	5.79	4.58	2.82	1.17	3.61
Mean	67.67	92.07	79.57	38.97	33.86	0.7921	57.47
C. V. %	11.70	1.29	7.28	11.75	8.33	147.55	6.28
R^2	0.9207	0.9975	0.9044	0.9754	0.9747	0.8647	0.9781
Adjusted R^2	0.8810	0.9809	0.8565	0.9384	0.9240	0.6619	0.9451

Predicted R^2	0.7969	0.8373	0.7552	0.8248	0.7404	0.0382	0.8439
Adeq. Precision	16.4198	32.4159	14.5225	15.4349	16.2974	7.0810	16.1300

Table 22. Final models to predict leaching efficiency of impurities in accordance with the significant parameters (H_2SO_4 + $C_6H_8O_7$ system).

Parameters	**Coefficient**						
	Mn (%) =	Zn (%) =	K (%) =	Na (%) =	Fe (%) =	Ba (%) =	Ca (%) =
	+5.739	+116.047	+32.939	-39.798	+51.291	-10.703	+20.29
Temperature (°C)	+0.750		+0.534	+1.557	-0.053	+0.145	+1.624
Time (h)	+7.093	-4.133	+4.808	+2.047	-2.961	+1.766	-6.452
H_2SO_4 (M)	+8.985	-21.022	+6.194	+0.596	-19.670	+3.230	-15.217
$C_6H_8O_7$ (M)	+72.168		+47.227	+30.998	+7.516	+7.228	+84.500
S/L (%)	-1.407	-0.807	-0.698	+1.229	-0.399	+0.347	+1.094
Temperature*Time		+0.115					
Temperature*H_2SO_4		+0.287			+0.491	-0.081	+0.394
Temperature* $C_6H_8O_7$		-0.777		-0.897			-1.753
Temperature*S/L		-0.027		-0.047	-0.043		-0.083
Time*H_2SO_4		-3.464					
Time* $C_6H_8O_7$		+9.840		+13.450	+11.614	+3.246	
Time*S/L		+0.270				-0.138	+0.362
H_2SO_4* $C_6H_8O_7$		+26.393		+25.860	-15.718		
H_2SO_4*S/L		+0.838			+0.901		
$C_6H_8O_7$*S/L		-1.599				-0.698	

6.3.2.2.2 XRD and XRF analysis of the final graphite (H_2SO_4 + $C_6H_8O_7$ system)

The graphite obtained in Run 6 (corresponding to Run 6 in Table 17) of the H_2SO_4 + $C_6H_8O_7$ system was analysed using XRF and XRD to identify residual impurities. As shown in Figure 4, quartz, barite, and anatase were detected in the graphite sample. Table 23 presents the XRF results for this sample, while Table 24 reports the major impurities, estimated in the form of oxides and sulphates.

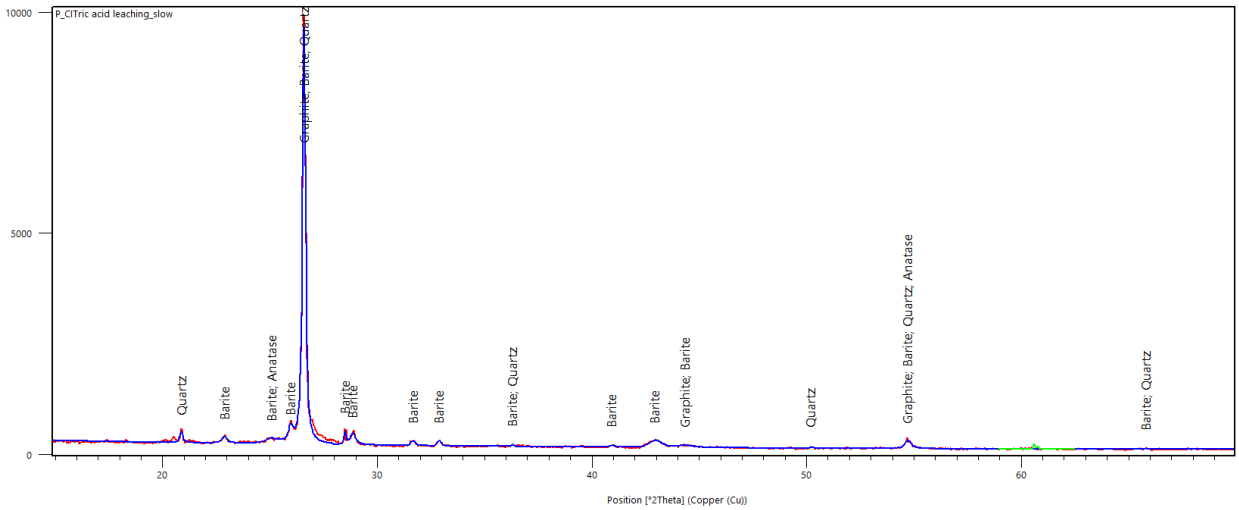

Figure 4. XRD pattern of the final graphite obtained in run 6 (H_2SO_4 + $C_6H_8O_7$ system).

Table 23. XRF analysis of the final graphite obtained in run 6 (H_2SO_4 + $C_6H_8O_7$ system).

Element	(%)	Element	(%)	Element	(%)
Na		As	0.00232	Nd	0.0887
Mg	<0.0020	Se	0.00039	HF	<0.00010
Al	<0.0020	Br	0.00097	Ta	<0.00010
Si	1.519	Rb	0.00032	W	<0.00010
P	<0.00030	Sr	0.06565	Hg	0.00202
S	1.392	Y	<0.00005	Tl	0.00016
Cl	0.1738	Zr	<0.00010	Pb	0.2873
K	0.1527	Nb	<0.00010	Bi	0.00555
Ca	0.03687	Mo	0.00030	Th	<0.00010
Ti	0.4704	Ag	0.00257	U	0.00016
V	0.01506	Cd	0.00062		
Cr	0.01201	Sn	<0.00030		
Mn	0.2666	Sb	0.00001		
Fe	1.829	Te	0.00246		
Co	<0.00030	I	<0.00030		
Ni	0.01253	Cs	<0.00040		
Cu	0.00310	Ba	3.838		
Zn	0.03269	La	<0.00020		
Ga	<0.00005	Ce	<0.00020		
Ge	<0.00005	Pr	0.0238		

Table 24. Estimated major impurities in the final graphite obtained in run 6 (H_2SO_4 + $C_6H_8O_7$ system).

Impurity	SiO_2	TiO_2	Fe_2O_3	$BaSO_4$	$PbSO_4$	$SrSO_4$	Sum
Wt. %	3.19	0.78	2.6	6.52	0.42	0.14	13.65

6.3.3 Evaluation of other systems (Further Purification: step 1)

The results of the previously investigated systems indicated that none of them could remove all impurities. Significant amounts of barium and iron remained in the final graphite product after purification. Consequently, additional systems were evaluated in an effort to enhance graphite purification, with a particular focus on the removal of Ba and Fe.

As a starting point, EABM-1 (Table 5) was leached under the optimal conditions previously determined for the H_2SO_4 + citric acid system. This involved leaching in a solution containing 1 M H_2SO_4 and 0.5 M citric acid for 3 hours at 60°C, using a solid-to-liquid ratio of 10% (corresponding to Run 6 in Table 17). The graphite obtained from this treatment was subsequently used in further experiments. Table 25 presents the main impurities in the obtained graphite, determined by dissolving a portion of the solid in aqua regia and analysing it using ICP.

It is worth noting that lead (Pb) and strontium (Sr) were also analysed in this sample. The results revealed that following the initial purification step using the H_2SO_4 + citric acid system, which is primarily effective in removing manganese, Pb and Sr became significantly concentrated and enriched in the resulting graphite.

Table 25. Main impurities in the obtained graphite (after leaching in H_2SO_4 + citric acid system), determined by ICP.

	Mn (%)	Zn (%)	K (%)	Na (%)	Fe (%)	Ba (%)	Ca (%)	Pb (%)	Sr (%)
1	0.2553	0.0436	0.0936	0.4766	1.6362	3.8074	0.2660	0.2074	0.0532
2	0.2657	0.0543	0.0981	0.4276	1.5657	3.7933	0.3838	0.2152	0.0543
Average	0.2605	0.0489	0.0959	0.4521	1.6009	3.8004	0.3249	0.2113	0.0537

Table 26 presents seven different systems that were evaluated for their effectiveness in further purifying the graphite. The experimental conditions were as follows:

- Test 1: High-concentration HCl solution.
- Test 2: High-concentration acetic acid solution.

- Test 3: A mixture of high-concentration HCl and H_2O_2.
- Test 4: A mixture of high-concentration acetic acid and H_2O_2.
- Test 5: A combination of high-concentration HCl, acetic acid, and H_2O_2.
- Test 6: EDTA solution at pH 12.
- Test 7: NaOH solution at pH 12.

All experiments were conducted at 60°C for 3 hours, with a solid-to-liquid ratio of 2.5% and mixing speed of 250 rpm. The experimental conditions are detailed in Table 26, while Table 27 summarizes the leaching results. Table 28 presents the final purity levels of the treated graphite determined by dissolving a portion of the solid in aqua regia and analysing it using ICP.

Table 26. The experimental conditions of the 7 different systems.

Test	HCl (37%) (%v/v)	H_2O_2 (30%) (%v/v)	Acetic acid (%v/v)	HCl (M)	H_2O_2 (M)	Acetic acid (M)	Na_2EDTA (M)	pH	Temperature (°C)	time (h)	S/L (%)
1	50	-	-	6	-	-	-	-	60	3	2.5
2	-	-	50	-	-	8.7	-	-	60	3	2.5
3	25	25	-	3	2.4	-	-	-	60	3	2.5
4	-	25	25	-	2.4	4.3	-	-	60	3	2.5
5	25	25	25	3	2.4	4.3	-	-	60	3	2.5
6	-	-	-	-	-	-	0.2	12	60	3	2.5
7	-	-	-	-	-	-	-	12	60	3	2.5

Table 27. Leaching results of the 7 different systems.

	Leaching results								
Test	Mn (%)	Zn (%)	K (%)	Na (%)	Fe (%)	Ba (%)	Ca (%)	Pb (%)	Sr (%)
1	96.44	76.71	54.83	21.42	98.50	11.65	29.53	54.72	46.52
2	66.31	22.80	11.28	3.11	1.03	1.09	11.62	5.67	6.57
3	95.13	64.64	51.90	8.62	71.64	7.46	25.53	71.36	63.15
4	78.92	32.40	15.46	3.54	2.46	1.60	13.45	7.49	9.81
5	97.11	75.03	52.18	7.36	92.03	4.61	33.09	62.90	56.89
6	55.74	33.11	87.93	99.48	1.58	97.73	36.34	98.03	96.64
7	7.78	3.21	21.58	70.83	0.20	1.34	5.94	2.53	2.77

Table 28. Final purity levels of the treated graphite with the 7 different systems.

	Impurities in the purified graphite								
Test	Mn (%)	Zn (%)	K (%)	Na (%)	Fe (%)	Ba (%)	Ca (%)	Pb (%)	Sr (%)
1	0.0094	0.0089	0.0225	0.1798	0.0254	3.2789	0.0648	0.1014	0.0300
2	0.0883	0.0317	0.0630	0.3613	1.5230	3.6504	0.0687	0.1987	0.0509
3	0.0127	0.0153	0.0318	0.3356	0.4623	3.4555	0.0703	0.0619	0.0203
4	0.0544	0.0249	0.0502	0.3498	1.4637	3.6414	0.0532	0.1996	0.0473
5	0.0078	0.0111	0.0288	0.2971	0.1473	3.1679	0.0486	0.0802	0.0226
6	0.1177	0.0274	0.0316	0.5684	1.6288	0.0921	0.0507	0.0042	0.0019
7	0.2358	0.0399	0.0619	0.4546	1.5147	3.8060	0.0720	0.2119	0.0532

6.3.4 EDTA and HCl system (Further Purification: step 2)

As shown in Table 28, the lowest concentration of Fe impurity was achieved in Test 1 using a high-concentration HCl solution, while the lowest levels of Ba, Pb, and Sr were observed in Test 6, which used an EDTA solution at pH 12. These findings suggest that combining the two approaches in sequential leaching steps could result in more effective impurity removal. Therefore, two methods were evaluated:

- HCl leaching followed by EDTA leaching (Test 1 followed by Test 6)
- EDTA leaching followed by HCl leaching (Test 6 followed by Test 1)

These tests were performed under the same conditions as Tests 1 and 6 in Table 26, with each leaching step conducted for 3 hours at 60°C, resulting in a total leaching time of 6 hours. Table 29 and Table 30 present the purity levels of the treated graphite after the first and second leaching purification steps for the two methods described above. The purity was determined by dissolving a portion of the solid in aqua regia and analysing it using ICP.

Table 29. Final purity levels of the treated graphite in HCl leaching, followed by EDTA leaching.

	Impurities in the purified graphite									
	Mn (%)	Zn (%)	K (%)	Na (%)	Fe (%)	Ba (%)	Ca (%)	Pb (%)	Sr (%)	Sum (%)
After HCl leaching	0.0454	0.0193	0.0878	0.3253	0.0763	3.6452	0.0678	0.0909	0.0270	4.3849
After HCl, followed by EDTA leaching	0.0194	0.0106	0.0531	0.5527	0.0683	0.3187	0.0403	0.0083	0.0032	1.0746

Table 30. Final purity levels of the treated graphite in EDTA leaching, followed by HCl leaching.

	Impurities in the purified graphite									
	Mn (%)	Zn (%)	K (%)	Na (%)	Fe (%)	Ba (%)	Ca (%)	Pb (%)	Sr (%)	Sum (%)
After EDTA leaching	0.0978	0.0217	0.1263	0.7889	1.3938	0.3019	0.0383	0.0068	0.0019	2.7774
After EDTA, followed by HCl leaching	0.0457	0.0115	0.0455	0.0821	0.0651	0.0630	0.0456	0.0021	0.0010	0.3615

As shown, the second method, EDTA leaching followed by HCl leaching, resulted in more effective impurity removal, particularly for K, Na, Fe, Ba, Pb, and Sr. This led to a lower overall concentration of total impurities (0.3668 %), as indicated in Table 30.

To validate these results, the second method was repeated under the same conditions. The outcomes, presented in Table 31, closely match those in Table 30, especially for Ba, Pb, and Sr. This consistency confirms the effectiveness of the proposed method for purifying graphite following the initial leaching with the H_2SO_4 + citric acid system.

Table 31. Final purity levels of the treated graphite in EDTA leaching followed by HCl leaching (replication of the second method).

	Impurities in the purified graphite									
	Mn (%)	Zn (%)	K (%)	Na (%)	Fe (%)	Ba (%)	Ca (%)	Pb (%)	Sr (%)	Sum (%)
After EDTA leaching	0.0951	0.0235	0.2154	0.6641	1.3932	0.3060	0.0803	0.0205	0.0026	2.8007
After EDTA, followed by HCl leaching	0.0150	0.0104	0.0473	0.0310	0.1153	0.0460	0.0185	0.0024	0.0010	0.2868

6.3.5 Characterization of the purified graphite (EDTA and HCl system)

To characterize the purified sample following the above treatment, a larger quantity of purified graphite was required. For this purpose, 120 g of EABM-1 (Table 5) was initially subjected to a leaching stage under the optimal conditions previously established for the H_2SO_4 + H_2O_2 system. This involved leaching in a solution containing 1 M H_2SO_4 and 10 vol% H_2O_2 (30%) for 3 hours at 60°C, with a solid-to-liquid ratio of 10% (corresponding to Run 7 in Table 10).

The H_2SO_4 + H_2O_2 system was selected to allow for comparison of the first-stage leaching results with those obtained using the previously investigated H_2SO_4+ citric acid system, prior to applying the second purification method (EDTA leaching followed by HCl leaching).

Following the initial leaching with the H_2SO_4 + H_2O_2 system, the pulp was filtered, washed, and dried, yielding 14.69 g of impure graphite from the initial 120 g of EABM-1.

Table 32 presents the impurity levels in the graphite obtained after treatment with the H_2SO_4 + H_2O_2 system. The results are consistent with those of the H_2SO_4 + citric acid system (Table 25), indicating that both systems effectively remove the majority of manganese. However, the resulting graphite still contains significant levels of other impurities, requiring further purification through EDTA leaching followed by HCl leaching.

The obtained graphite (Table 32) was then treated using the second method, EDTA leaching followed by HCl leaching, to further reduce impurity levels. The pulp was filtered, washed, and dried, yielding 12.51 g of the purified graphite from the initial 120 g of EABM-1.

The final purified graphite was subsequently characterized using various analytical techniques, as discussed in the following subsections.

Table 32. Main impurities in the obtained graphite after treating 120 g of EABM-1 (after leaching in the H_2SO_4 + H_2O_2 system), determined by ICP.

	Mn (%)	Zn (%)	K (%)	Na (%)	Fe (%)	Ba (%)	Ca (%)	Pb (%)	Sr (%)
1	0.1145	0.0869	0.1175	0.0298	1.4474	3.4167	0.0838	0.1949	0.0504
2	0.1211	0.0873	0.1544	0.0402	1.5633	3.5222	0.0939	0.2251	0.0522
3	0.1173	0.0484	0.1330	0.0349	1.4431	3.4411	0.0772	0.2133	0.0503
Average	0.1176	0.0742	0.1350	0.0350	1.4846	3.4600	0.0849	0.2111	0.0510

6.3.5.1 XRD

The purified graphite was characterized using XRD to identify its major phases (Figure 5). The analysis revealed that the primary constituents are graphite and quartz, with no detectable presence of barite. This indicates the near-complete removal of barium sulphate as a result of the purification process using EDTA leaching followed by HCl leaching.

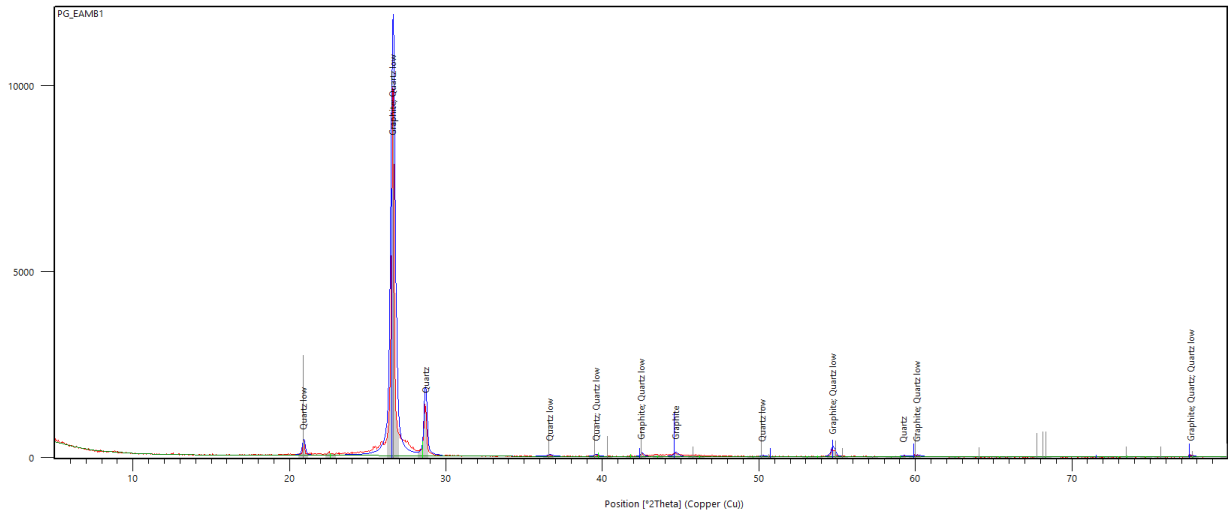

Figure 5. XRD pattern of the purified graphite obtained from EABM-1 (EDTA and HCl system).

6.3.5.2 XRF

The purified graphite was analysed using XRF to identify residual impurities. Table 33 presents the XRF results for this sample, while Table 34 reports the major impurities, estimated in the form of oxides and sulphates.

Table 33. XRF analysis of the final purified graphite obtained from EABM-1 (EDTA and HCl system).

Element	(%)	Element	(%)	Element	(%)
Na	-	**As**	0.00032	**Nd**	0.00355
Mg	<0.0020	**Se**	0.00006	**HF**	0.00005
Al	<0.0020	**Br**	0.00061	**Ta**	<0.00010
Si	2.017	**Rb**	0.00013	**W**	0.00015
P	0.00433	**Sr**	0.00171	**Hg**	0.00054
S	0.06866	**Y**	0.00008	**Tl**	0.00007
Cl	0.1781	**Zr**	<0.00010	**Pb**	0.00342
K	0.1185	**Nb**	0.00051	**Bi**	0.00035
Ca	0.01074	**Mo**	0.00003	**Th**	<0.00010
Ti	0.5315	**Ag**	0.00007	**U**	<0.00010
V	0.00333	**Cd**	0.00008		
Cr	0.00326	**Sn**	0.00501		
Mn	0.02063	**Sb**	<0.00030		
Fe	0.07555	**Te**	<0.00030		
Co	<0.00030	**I**	<0.00030		

Ni	0.00296	**Cs**	<0.00040
Cu	0.00077	**Ba**	0.3444
Zn	0.00530	**La**	<0.00020
Ga	0.00022	**Ce**	<0.00020
Ge	0.00001	**Pr**	<0.00020

Table 34. Estimated major impurities in the final purified graphite obtained from EABM-1 (EDTA and HCl system).

Impurity	**SiO_2**	**TiO_2**	**Fe_2O_3**	**$BaSO_4$**	**$PbSO_4$**	**$SrSO_4$**	**Sum**	**Graphite Purity**
Wt. %	4.32	0.88	0.08	0.10	0.00	0.00	5.39	**94.25%**

6.3.5.3 ICP

The purity of the purified graphite was also determined by dissolving a portion of the graphite in aqua regia and analysing it using ICP. Table 35 presents the ICP results, which are consistent with those shown in Table 30 and Table 31. This further confirms the effectiveness of the proposed method for purifying graphite.

Table 35. Final purity levels of the purified graphite obtained from EABM-1 (EDTA and HCl system).

	Mn (%)	**Zn (%)**	**K (%)**	**Na (%)**	**Fe (%)**	**Ba (%)**	**Ca (%)**	**Pb (%)**	**Sr (%)**	**Sum (%)**
1	0.0100	0.0162	0.0381	0.0553	0.0577	0.0629	0.1110	0.0022	0.0022	0.3557
2	0.0133	0.0147	0.0287	0.0393	0.0599	0.0646	0.0591	0.0024	0.0018	0.2838
3	0.0079	0.0114	0.0259	0.0399	0.0543	0.0643	0.0521	0.0025	0.0019	0.2602
Average	0.0104	0.0141	0.0309	0.0448	0.0573	0.0639	0.0741	0.0023	0.0019	0.2999

6.3.5.4 TGA

The purified graphite was further characterized by TGA to evaluate weight loss during heating. The sample was heated in air up to 1100 °C at a constant rate of 5 °C/min. The results are presented in Figure 6. As can be seen the total weight loss up to 1100 °C is about 94.5%.

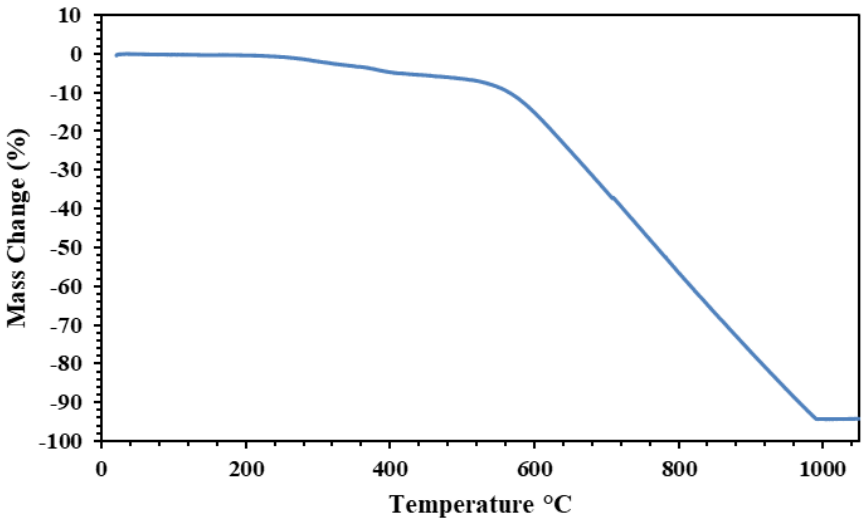

Figure 6. TGA graph of the purified graphite obtained from EABM-1 (EDTA and HCl system).

6.3.5.5 PSD

The particle size distribution of the purified graphite was also analysed. The results are presented in Table 36 and illustrated in Figure 7.

Table 36. PSD results for the purified graphite obtained from EABM-1 (EDTA and HCl system).

	mm
D (0.1)	10.97
D (0.5)	69.02
D (0.9)	300.03

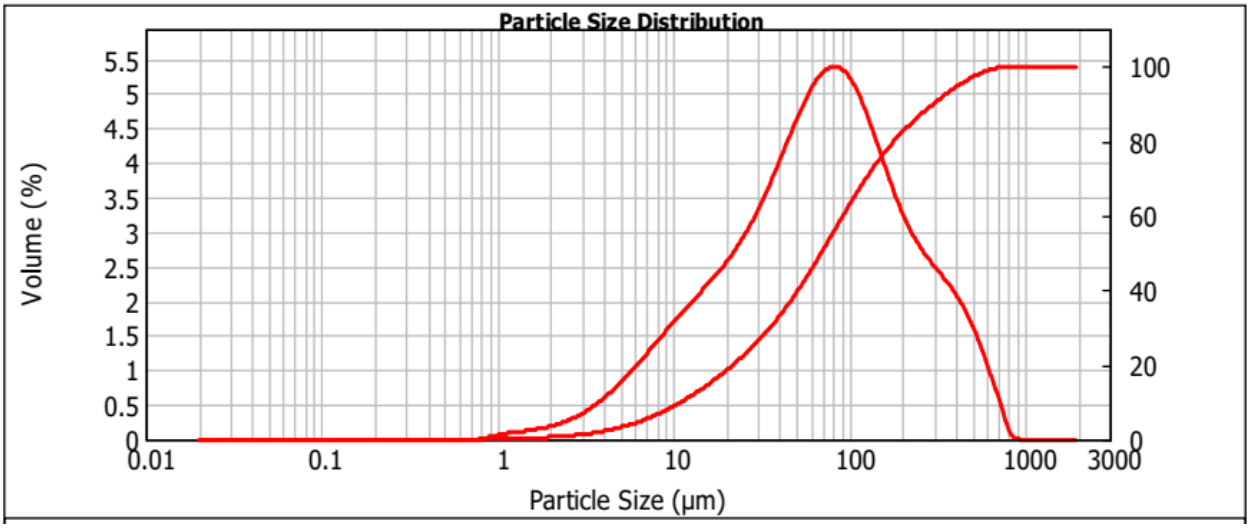

Figure 7. PSD of the purified graphite obtained from EABM-1 (EDTA and HCl system).

6.3.6 Final Purity of Obtained Graphite

The impurities present in the final graphite are calculated in Table 34; these impurities are in the form of silica, sulfates, and oxides, and the sum is **5.39%.** Table 30 includes the percentage of impurities in the elemental form **(0.3668%).** So, the overall purity of the final graphite obtained is **94.25%.**

The characterization results indicated that the obtained purified graphite is the highest-quality sample (94.25% pure) produced during the evaluation of various purification systems. Consequently, this sample was selected for further investigation.

6.4 Conclusions

This chapter contains the overall process for the high-purity graphite recovery from the spent alkaline black mass. This black mass was first converted to an exhausted alkaline black mass by leaching using sulfuric acid. In this step, most of the manganese, potassium, and zinc oxides were removed, leaving behind a relatively pure black mass compared to the as-received sample. Due to the partial dissolution of manganese oxides in sulfuric acid, a reducing agent was required to enhance the removal of manganese, particularly MnO_2, from EABM. Accordingly, binary systems comprising a strong acid (H_2SO_4 or HCl) and a reducing agent (H_2O_2 or citric acid, $C_6H_8O_7$) were evaluated as the primary purification systems. In this study, a combination of H_2SO_4 with two reducing agents was investigated by a fractional factorial design. Different leaching conditions, such as temperature, time, and rpm, were also investigated. The optimal condition was determined from the H_2SO_4 + citric acid system (corresponding to Run 6 in Table 17) involving leaching in a solution containing 1 M H_2SO_4 and 0.5 M citric acid for 3 hours at 60°C, using a solid-to-liquid ratio of 10%. After treating the whole EABM under these conditions, the obtained sample was then subjected to further purification because significant amounts of barium and iron still remained in the final graphite product after this step. The first step of final purification was done according to Table 28, while the second step was done in two stages, and the results are demonstrated in Tables 30 and 31. The overall concentrations of total impurities were 0.3668 % in the elemental form, while 5.39% in the form of sulfates, oxides, and silica, and overall yielding a high-purity graphite with 94.25% purity.

CHAPTER 7

Optimization of Hydrometallurgical Recycling of Graphite from End-of-Life Lithium-ion Batteries

7.1 Introduction

The graphite market is growing rapidly due to its role in the manufacturing of large battery cells and their ultimate need for the replacement of electric vehicles with fuel-driven cars[145]. Every year, a large number of spent lithium-ion batteries are produced, containing high-value materials. Many industries currently recycle these materials from spent batteries, such as Ni, Co, Al, and Cu, but little attention is given to graphite recovery and its uses[146], as graphite has a lower economic value due to its large abundance.

The graphite is present in almost 12-21 percent of the weight of the lithium batteries[147], and hence, a big bulk of spent graphite is being produced with the increasing use of these batteries. Low-quality graphite obtained during recycling is generally a byproduct of the recycling process in the form of residual slag[148]. The per-ton battery-grade graphite costs almost USD 8000–13,000[149], which is almost 10-15 percent of the cost of the battery manufacturing[147]. Besides the economic point of view, the spent graphite can also cause environmental pollution as it contains some binders, toxic electrolytes (which are also flammable), metals, and plastics as well[150]. So, the recovery of these spent batteries and graphite is crucial not only to reduce resource waste but also to prevent environmental hazards[151].

There are several methods for the recycling of graphite from spent lithium batteries, including pyrometallurgy, hydrometallurgy, and direct recycling. In pyrometallurgy, the feedstock impurities are removed by pyrolysis, which sometimes also burns the graphite, and a large amount of energy is required as well[152]. Direct recycling is used to recover cathode active material and the separation of graphite anode, which can be further treated to be reused[153], [154]. In hydrometallurgy, the metals from the black mass are leached in the form of metal ions with some mineral acids and reducing agents, and further precipitated in the form of salts[155]. Various alkalis and deionized water are also used to recover metal ions; for instance, the solid electrolyte interface layers and lithium can be removed from spent graphite anodes with deionized water[156].

The worthy recovery process will only be guaranteed if the recovered graphite can be used as a battery-grade product. In order to achieve such processes, some sustainable and efficient methods are needed to separate and purify the graphite from the waste battery materials[157]. In this study, the graphite from the spent lithium-ion batteries, which is referred to as impure lithium graphite (ILG), was recovered through different hydrometallurgical approaches. The recovered graphite has good purity and can be used for further applications. This work was done under the LIFE-GRAPhiREC project, and the samples were provided by Orim s.p.a. industry.

7.2 Materials and methods

The materials and methods are the same as described in Chapter 6 (section 6.2).

7.3 Results and discussions

7.3.1 Characterization of received sample: Impure lithium graphite (ILG)

In this section, the characterization of the input materials (ILG) was carried out prior to treatment. Various analytical techniques, including XRD, XRF, ICP, PSD, and TGA, were employed to evaluate the variability of the input material.

7.3.1.1 XRF analysis

The as-received (ILG-1) sample was also analysed using XRF to identify the main impurities. The results are presented in Table 1, indicating that the primary impurities include Na, Mg, Si, S, K, Ca, Fe, Cu, and Zn.

Table 1. XRF results for ILG-1.

Element	(%)	Element	(%)	Element	(%)
Na	0.51569	**As**	<0.00005	**Nd**	0.00169
Mg	0.01741	**Se**	<0.00005	**HF**	<0.00010
Al	<0.00201	**Br**	0.00017	**Ta**	<0.00010
Si	0.61214	**Rb**	0.00002	**W**	0.00793
P	<0.00030	**Sr**	0.00024	**Hg**	<0.00010
S	0.02334	**Y**	0.00008	**Tl**	<0.00010
Cl	0.00828	**Zr**	0.00944	**Pb**	0.00107
K	0.01341	**Nb**	<0.00009	**Bi**	0.00025
Ca	0.01200	**Mo**	0.00049	**Th**	<0.00010
Ti	0.00994	**Ag**	0.00008	**U**	<0.00009
V	0.00220	**Cd**	0.00004		
Cr	0.00381	**Sn**	0.00341		
Mn	<0.00010	**Sb**	0.00016		
Fe	0.06239	**Te**	<0.00030		
Co	<0.00029	**I**	<0.00030		

Ni	0.00393	**Cs**	<0.00040
Cu	2.33495	**Ba**	0.00404
Zn	0.04773	**La**	0.00169
Ga	0.00076	**Ce**	<0.00020
Ge	<0.00005	**Pr**	0.00131

7.3.1.2 ICP analysis

To obtain more accurate impurity data, the ILG-1 sample was dissolved in aqua regia, and the resulting solution was analysed using ICP. This analysis was performed in three replicates to calculate the associated error. The results are presented in Table 2.

Table 2. Main impurities in ILG-1 determined by ICP.

Al (%)	Ba (%)	Ca (%)	Mg (%)	Na (%)	K (%)	Li (%)	Fe (%)	Zn (%)	Cu (%)
0.00921	0.00876	0.03847	0.01051	0.10855	0.00964	0.00042	0.04475	0.04677	7.83393
±	±	±	±	±	±	±	±	±	±
0.0025	0.0049	0.01072	0.00291	0.00144	0.00047	0.00028	0.01149	0.00440	0.65574

Table 3 presents the moisture content of the ILG-1 sample, determined by drying at 105 °C for 24 hours. These measurements were also conducted in here replicates to assess variability and error.

Table 3. Moisture content of ILG-1.

	(%)
Moisture	1.2096 ± 0.3130

7.3.1.3 TGA analysis

The ILG-1 sample was further characterized by TGA to evaluate weight loss during heating. The sample was heated in air up to 1050 °C at a constant rate of 5 °C/min. The results are presented in Figure 24. As can be seen the total weight loss up to 1050 °C is about 88.16%.

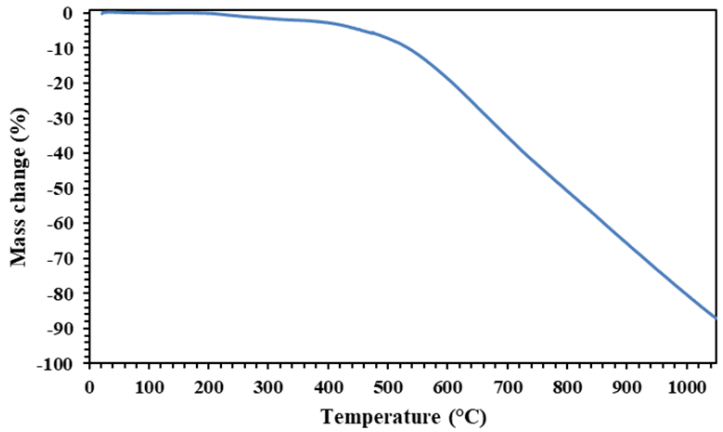

Figure 1. TGA graph of ILG-1 (heating rate of 5 °C/min in air).

7.3.1.4 CHNS analysis

CHNS analysis was conducted to determine the carbon content of the ILG-1 sample. As shown in Table 4, ILG-1 contains approximately 91% carbon.

Table 4. CHNS analysis results for ILG-1.

Run	Mass (mg)	C (%)	H (%)	N (%)	S (%)
1	4.41	89.25	0.05	0	0
2	3.24	92.11	0.02	0	0
Average		90.68	0.04	0	0

7.3.1.5 PSD analysis

The particle size distribution of the ILG-1 sample was also analysed. The results are presented in Table 5 and illustrated in Figure 2.

Table 5. PSD results for ILG-1.

	mm
D (0.1)	8.604
D (0.5)	19.533
D (0.9)	104.536

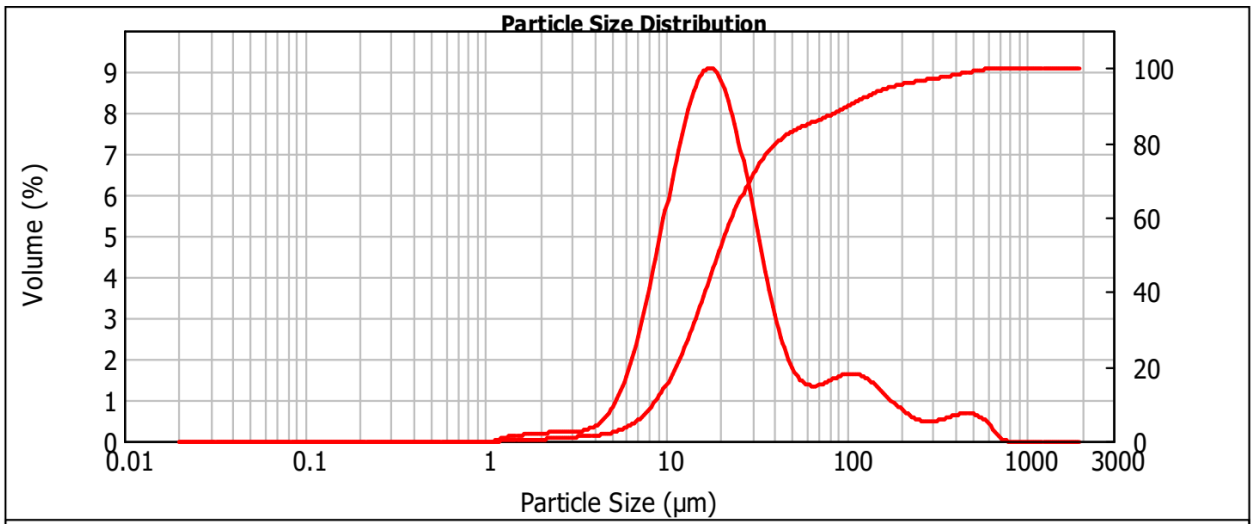

Figure 2. PSD of ILG-1.

7.3.2 Hydrometallurgical tests on impure lithium graphite

7.3.2.1 Leaching purification experiments

In this section, purification experiments were conducted to recover and purify graphite from the ILG-1 sample (Table 2), selected as a representative of the ILG group. Due to the presence of metallic copper in the sample, an oxidizing agent is required to enhance the removal of copper from ILG. Accordingly, a binary system comprising a strong acid (H_2SO_4) and an oxidizing agent (H_2O_2) was evaluated as the primary purification system.

7.3.2.1.1 Sulfuric acid and hydrogen peroxide system

As previously mentioned, Cu is the main impurity in ILG and is almost insoluble in sulfuric acid alone. Therefore, an oxidizing agent is essential to facilitate its dissolution. Hydrogen peroxide, for instance, is an effective oxidizing agent for this purpose, as demonstrated by Equation 1.

$$Cu + H_2SO_4 + H_2O_2 \rightarrow CuSO_4 + 2H_2O \quad (1)$$

A series of experiments was designed using a fractional factorial design approach to assess the effect of key leaching parameters on impurity removal and graphite purification. Table 6 summarizes the parameter levels used in the leaching experiments. Each test was performed using 20 mL of solution. After leaching, all solids were dissolved in aqua regia and analysed by ICP to determine the impurity content.

Table 6. Levels of leaching parameters to recover and purify graphite from ILG in H_2SO_4 + H_2O_2 system.

Parameter	Level (-1)	Level (+1)

Temperature (°C)	25	60
Time (h)	1	3
H_2SO_4 Concentration (M)	1	2
H_2O_2 (30%) Concentration (%V/V)	5	10
S/L (%)	10	20

Table 7 and Table 8 present the conditions of the purification experiments and the chemical composition of the final graphite, respectively. As shown in Table 8, the lowest impurity level was achieved in Run 6; however, a considerable amount of impurities remained. The main residual elements were Cu, and Fe. Table 9 summarizes the leaching efficiency of each element across the 16 experiments.

Table 7. Leaching purification conditions to recover and purify graphite from ILG in H2SO4 + H2O2 system.

Run	Temperature (°C)	Time (h)	H_2SO_4 Conc. (M)	H_2O_2 (30%) Conc. (%V/V)	S/L (%)
1	25	1	2	10	20
2	25	3	2	5	20
3	60	1	1	10	20
4	25	1	1	10	10
5	60	3	2	10	20
6	60	3	2	5	10
7	25	3	1	10	20
8	60	3	1	5	20
9	25	3	1	5	10
10	60	1	2	5	20
11	60	1	2	10	10
12	25	1	1	5	20
13	25	3	2	10	10
14	60	3	1	10	10
15	60	1	1	5	10
16	25	1	2	5	10

Table 8. Chemical composition of the recovered graphite from ILG according to the conditions of Table 151 in H_2SO_4 + H_2O_2 system.

Run	Al (%)	Ba (%)	Ca (%)	Mg (%)	Na (%)	K (%)	Li (%)	Fe (%)	Zn (%)	Cu (%)	Sum (%)
1	0.0046	0.0094	0.0176	0.0043	0.0141	0.0033	0.0000	0.0342	0.0031	0.0645	0.1550
2	0.0057	0.0074	0.0299	0.0061	0.0142	0.0027	0.0000	0.0314	0.0041	0.0418	0.1433

3	0.0041	0.0086	0.0355	0.0047	0.0125	0.0039	0.0000	0.0249	0.0037	0.0963	0.1941
4	0.0056	0.0091	0.0193	0.0046	0.0136	0.0022	0.0000	0.0369	0.0032	0.0421	0.1367
5	0.0026	0.0080	0.0191	0.0026	0.0097	0.0026	0.0000	0.0182	0.0026	0.0221	0.0875
6	0.0024	0.0123	0.0149	0.0020	0.0094	0.0026	0.0000	0.0179	0.0033	0.0201	0.0849
7	0.0024	0.0077	0.0147	0.0032	0.0095	0.0015	0.0000	0.0315	0.0021	0.0275	0.1000
8	0.0019	0.0104	0.0166	0.0026	0.0088	0.0021	0.0000	0.0268	0.0032	0.0289	0.1013
9	0.0033	0.0053	0.0104	0.0020	0.0100	0.0015	0.0000	0.0251	0.0016	0.0450	0.1041
10	0.0026	0.0188	0.0160	0.0031	0.0091	0.0016	0.0000	0.0210	0.0039	0.0312	0.1072
11	0.0031	0.0072	0.0178	0.0031	0.0092	0.0022	0.0000	0.0202	0.0031	0.0265	0.0925
12	0.0040	0.0066	0.0099	0.0023	0.0108	0.0015	0.0000	0.0362	0.0027	0.1505	0.2245
13	0.0023	0.0075	0.0200	0.0038	0.0117	0.0017	0.0000	0.0251	0.0025	0.0361	0.1107
14	0.0027	0.0098	0.0159	0.0027	0.0087	0.0017	0.0000	0.0192	0.0025	0.0223	0.0855
15	0.0048	0.0078	0.0341	0.0035	0.0143	0.0029	0.0000	0.0306	0.0300	0.0264	0.1544
16	0.0026	0.0075	0.0139	0.0023	0.0106	0.0016	0.0000	0.0278	0.0026	0.0431	0.1120

Table 9. Leaching efficiency of impurities in purification experiments of graphite from ILG (H2SO4 + H2O2 system).

Run	**Al (%)**	**Ba (%)**	**Ca (%)**	**Mg (%)**	**Na (%)**	**K (%)**	**Li (%)**	**Fe (%)**	**Zn (%)**	**Cu (%)**	**Weight loss (%)**
1	61.29	0.39	54.17	66.14	92.15	80.89	100.00	35.10	93.74	99.34	11.15
2	59.27	0.53	43.90	56.08	92.09	83.68	100.00	39.28	92.11	99.51	12.3
3	67.04	0.71	39.52	64.66	93.03	78.45	100.00	48.96	93.07	98.94	13.425
4	53.43	1.19	53.48	63.08	90.98	83.24	100.00	30.15	93.87	99.51	9.9
5	78.99	0.92	51.58	77.70	94.56	84.08	100.00	63.63	94.94	99.75	15.05
6	80.90	1.00	60.96	86.10	94.17	83.45	100.00	66.75	94.16	99.78	12.15
7	75.43	0.60	58.41	71.37	94.39	89.63	100.00	33.75	95.85	99.70	11.05
8	80.39	0.39	55.95	78.65	94.93	86.96	100.00	50.16	94.03	99.69	11.425
9	68.58	1.26	65.26	76.94	93.68	88.74	100.00	40.20	96.35	99.47	10.7
10	78.78	0.22	62.13	83.55	94.83	91.04	100.00	56.21	93.15	99.68	12.025
11	76.27	1.27	57.62	74.00	94.28	84.50	100.00	59.36	94.14	99.70	13.2
12	61.74	0.62	66.21	75.22	93.63	89.55	100.00	31.49	94.81	98.19	10.2
13	75.16	0.59	51.00	67.05	92.56	86.57	100.00	40.71	94.86	99.59	13.25
14	78.57	0.99	59.87	79.98	94.59	88.02	100.00	62.37	95.87	99.76	14.3
15	66.67	1.34	43.98	72.66	91.50	80.98	100.00	47.35	63.68	99.75	15.5
16	73.80	1.18	62.35	78.48	93.27	88.87	100.00	39.17	95.08	99.51	12.95

All leaching data were statistically evaluated using analysis of variance (ANOVA). The ANOVA results for impurities are summarized in Table 10, where parameters with a p-value of less than 0.1 are considered significant in the leaching process. Non-significant parameters were excluded (except those required to support hierarchy); therefore, Table 10 presents only the significant parameters for impurity removal.

Table 11 presents the ANOVA fit statistics for leaching efficiency of impurities in the purification experiments. The high R^2 values indicate a good model fit to the experimental data for each impurity element. Table 12 summarizes the final models for predicting the leaching efficiency of each element based on the significant parameters.

Table 10. Analysis of variance for leaching efficiency of impurities in purification experiments of graphite from ILG (H2SO4 + H2O2 system).

Source	Sum of Squares	Degree of Freedom	Mean Square	F-Value	p-Value	
			Al			
Model	1068.84	8	133.61	24.51	0.0002	significant
A-Temperature	389.27	1	389.27	71.4	< 0.0001	
B-Time	212.09	1	212.09	38.9	0.0004	
C-H_2SO_4	66.43	1	66.43	12.18	0.0101	
D-H_2O_2	0.9732	1	0.9732	0.1785	0.6853	
E-S/L	6.8	1	6.8	1.25	0.3008	
BC	155.74	1	155.74	28.57	0.0011	
BD	110.05	1	110.05	20.19	0.0028	
CE	127.48	1	127.48	23.38	0.0019	
Residual	38.16	7	5.45			
Cor Total	1107.01	15				
			Ba			
Model	1.92	9	0.213	22.83	0.0006	significant
A-Temperature	0.0146	1	0.0146	1.57	0.257	
B-Time	0.0263	1	0.0263	2.82	0.1441	
C-H_2SO_4	0.0624	1	0.0624	6.69	0.0414	
D-H_2O_2	0.0008	1	0.0008	0.0899	0.7744	
E-S/L	1.23	1	1.23	131.99	< 0.0001	
AC	0.0566	1	0.0566	6.07	0.0489	
AD	0.1966	1	0.1966	21.06	0.0037	
BE	0.1676	1	0.1676	17.96	0.0055	
DE	0.1608	1	0.1608	17.24	0.006	
Residual	0.056	6	0.0093			
Cor Total	1.97	15				
			Ca			
Model	890.18	10	89.02	12.15	0.0065	significant
A-Temperature	33.6	1	33.6	4.59	0.0851	
B-Time	3.49	1	3.49	0.4765	0.5207	
C-H_2SO_4	0.0642	1	0.0642	0.0088	0.929	
D-H_2O_2	77.01	1	77.01	10.51	0.0229	
E-S/L	32.02	1	32.02	4.37	0.0908	
AB	114.23	1	114.23	15.6	0.0109	
AC	263.41	1	263.41	35.97	0.0019	
BC	265.08	1	265.08	36.19	0.0018	
BD	37.97	1	37.97	5.18	0.0718	
BE	63.31	1	63.31	8.64	0.0322	

Residual	36.62	5	7.32			
Cor Total	926.8	15				
			Mg			
Model	927.26	10	92.73	9.56	0.0112	significant
A-Temperature	247.56	1	247.56	25.52	0.0039	
B-Time	16.14	1	16.14	1.66	0.2536	
C-H_2SO_4	2.68	1	2.68	0.276	0.6218	
D-H_2O_2	119.35	1	119.35	12.3	0.0172	
E-S/L	38.81	1	38.81	4	0.1019	
AB	95.25	1	95.25	9.82	0.0259	
AC	122.48	1	122.48	12.62	0.0163	
BC	135.54	1	135.54	13.97	0.0135	
BD	101.72	1	101.72	10.48	0.023	
BE	47.74	1	47.74	4.92	0.0773	
Residual	48.51	5	9.7			
Cor Total	975.77	15				
			Na			
Model	22.43	10	2.24	13.77	0.0049	significant
A-Temperature	5.21	1	5.21	31.97	0.0024	
B-Time	3.33	1	3.33	20.44	0.0063	
C-H_2SO_4	0.0894	1	0.0894	0.5486	0.4922	
D-H_2O_2	0.1548	1	0.1548	0.9505	0.3744	
E-S/L	1.31	1	1.31	8.04	0.0364	
AC	2.57	1	2.57	15.76	0.0106	
AD	0.8191	1	0.8191	5.03	0.075	
BC	5.77	1	5.77	35.44	0.0019	
BD	1.02	1	1.02	6.27	0.0542	
CE	2.16	1	2.16	13.27	0.0148	
Residual	0.8144	5	0.1629			
Cor Total	23.25	15				
			K			
Model	192.74	9	21.42	13.02	0.0027	significant
A-Temperature	11.72	1	11.72	7.13	0.037	
B-Time	11.61	1	11.61	7.06	0.0377	
C-H_2SO_4	0.3859	1	0.3859	0.2347	0.6453	
D-H_2O_2	20.01	1	20.01	12.17	0.013	
E-S/L	0.0007	1	0.0007	0.0004	0.9843	
AC	24.53	1	24.53	14.92	0.0083	
BC	51.27	1	51.27	31.18	0.0014	
BD	51.88	1	51.88	31.55	0.0014	
DE	21.34	1	21.34	12.98	0.0113	
Residual	9.87	6	1.64			
Cor Total	202.61	15				
			Fe			
Model	2129.84	6	354.97	46.05	< 0.0001	significant
A-Temperature	1700.2	1	1700.2	220.56	< 0.0001	
B-Time	150.3	1	150.3	19.5	0.0017	
C-H_2SO_4	194.51	1	194.51	25.23	0.0007	

D-H_2O_2	0.7309	1	0.7309	0.0948	0.7652	
E-S/L	47.21	1	47.21	6.12	0.0353	
AD	36.89	1	36.89	4.79	0.0565	
Residual	69.38	9	7.71			
Cor Total	2199.22	15				
			Zn			
Model	870.09	14	62.15	1.84	0.5262	Not significant
A-Temperature	70.68	1	70.68	2.1	0.3847	
B-Time	83.92	1	83.92	2.49	0.3595	
C-H_2SO_4	37.99	1	37.99	1.13	0.4809	
D-H_2O_2	67.89	1	67.89	2.02	0.3907	
E-S/L	35.07	1	35.07	1.04	0.4936	
AB	69.31	1	69.31	2.06	0.3876	
AC	75.8	1	75.8	2.25	0.3743	
AD	68.26	1	68.26	2.03	0.3899	
AE	60.02	1	60.02	1.78	0.4093	
BC	84.28	1	84.28	2.5	0.3589	
BE	65.21	1	65.21	1.94	0.3967	
CD	44.22	1	44.22	1.31	0.4568	
CE	65.21	1	65.21	1.94	0.3967	
DE	42.23	1	42.23	1.25	0.4641	
Residual	33.69	1	33.69			
Cor Total	903.77	15				
			Cu			
Model	2.36	9	0.2619	11.9	0.0035	significant
A-Temperature	0.3104	1	0.3104	14.1	0.0095	
B-Time	0.4272	1	0.4272	19.41	0.0045	
C-H_2SO_4	0.2158	1	0.2158	9.8	0.0203	
D-H_2O_2	0.0321	1	0.0321	1.46	0.2725	
E-S/L	0.3179	1	0.3179	14.44	0.009	
AD	0.3109	1	0.3109	14.12	0.0094	
BC	0.2078	1	0.2078	9.44	0.0219	
BE	0.3575	1	0.3575	16.24	0.0069	
CE	0.1777	1	0.1777	8.07	0.0295	
Residual	0.1321	6	0.022			
Cor Total	2.49	15				

Table 11. Fit statistics of ANOVA for leaching efficiency of impurities in purification experiments of graphite from ILG (H_2SO_4 + H_2O_2 system).

	Al	**Ba**	**Ca**	**Mg**	**Na**	**K**	**Fe**	**Zn**	**Cu**
Std. Dev.	2.33	0.0966	2.71	3.11	0.4036	1.28	2.78	5.8	0.1484
Mean	71.02	0.8247	55.4	73.23	93.41	85.54	46.54	92.48	99.49
C. V. %	3.29	11.71	4.89	4.25	0.432	1.5	5.97	6.28	0.1491
R^2	0.9655	0.9716	0.9605	0.9503	0.965	0.9513	0.9685	0.9627	0.9469
Adjusted R^2	0.9261	0.9291	0.8815	0.8509	0.8949	0.8783	0.9474	0.4409	0.8674
Predicted R^2	0.8199	0.7983	0.5954	0.4909	0.6413	0.6537	0.9003	-8.542	0.6227

Adeq. Precision	16.350	13.125	12.168	9.9548	11.827	13.704	18.594	5.7291	12.251

Table 12. Final models to predict leaching efficiency of impurities in ILG in accordance with the significant parameters (H2SO4 + H2O2 system).

Parameters	**Al (%) =**	**Ba (%) =**	**Ca (%) =**	**Mg (%) =**	**Na (%) =**	**K (%) =**	**Fe (%) =**	**Zn (%) =**	**Cu (%) =**
	+19.953	+4.588	+84.046	+92.615	+89.500	+88.449	+20.481	-	+98.913
Temperature (°C)	+0.282	-0.027	-1.084	-0.528	-0.075	-0.261	+0.329	-	+0.032
Time (h)	+5.133	-0.348	+7.535	+1.428	+1.500	+0.820	+3.065	-	+0.057
H_2SO_4 (M)	+33.491	-0.414	-3.300	-0.978	+2.812	+0.835	+6.973	-	+0.056
H_2O_2 (%V/V)	-2.197	-0.225	-2.110	-3.110	-0.461	-0.502	-1.390	-	+0.153
S/L (%)	+1.563	-0.157	+0.513	+0.379	+0.278	+0.692	-0.343	-	-0.151
Temperature*Time			+0.153	+0.139				-	
Temperature*H_2SO_4		+0.007	+0.464	+0.316	+0.046	+0.142		-	
Temperature*H_2O_2		+0.003			+0.005		+0.035	-	-0.003
Temperature*S/L								-	
Time*H_2SO_4	-6.240		-8.141	-5.821	-1.201	-3.580		-	-0.228
Time*H_2O_2	+1.049		+0.616	-1.009	+0.101	+0.720		-	
Time*S/L		+0.020	-0.398	-0.345				-	+0.030
H_2SO_4*H_2O_2								-	
H_2SO_4*S/L	-1.129				-0.147			-	+0.042
H_2O_2*S/L		+0.008				-0.092		-	

7.3.2.1.2 Counter-current approach

Based on the above results, it can be concluded that using 1 M H_2SO_4 and 5 vol% H_2O_2 (30%) is effective for removing most impurities and purifying graphite. However, to achieve higher purification efficiency, a counter-current leaching approach was considered, as illustrated in Figure 3. Five leaching tests were conducted under the conditions listed in Table 13, following the sequence below to repeat the counter-current process at least twice and approach the equilibrium state of the system:

- **1st leaching:** Charging ILG-1 and reagents into R2 (Figure 3), followed by filtration to separate the solid (S1) and liquid (L1).
- **2nd leaching:** Charging the recovered liquid from the 1st leaching (L1) and new ILG-1 into R1 (Figure 38), then filtration to obtain S2 and L2.
- **3rd leaching:** Charging the solid recovered from the 2nd leaching (S2) with fresh reagents into R2, followed by filtration to obtain S3 and L3.
- **4th leaching:** Charging the recovered liquid from the 3rd leaching (L3) and new ILG-1 into R1, then filtration to obtain S4 and L4.

- **5th leaching:** Charging the solid recovered from the 4th leaching (S4) with fresh reagents into R2, followed by filtration to obtain S5 and L5.

For each test, 40 g of ILG-1 was used as the new ILG-1 sample. After each leaching step, the resulting solid cake was washed following filtration. The S3 and S5 samples were targeted as the purified graphite products and subsequently analysed using chemical attack and ICP to evaluate their purity levels.

It should be noted that the counter-current experiments were conducted at both room temperature and 70°C, and the results are presented in the following subsections.

Table 13. Leaching conditions of the counter-current tests conducted to purify ILG-1.

Temperature (°C)	Time (h)	H_2SO_4 (M)	H_2O_2 (%V)	S/L (%)
25 and 70	1	1	5	20

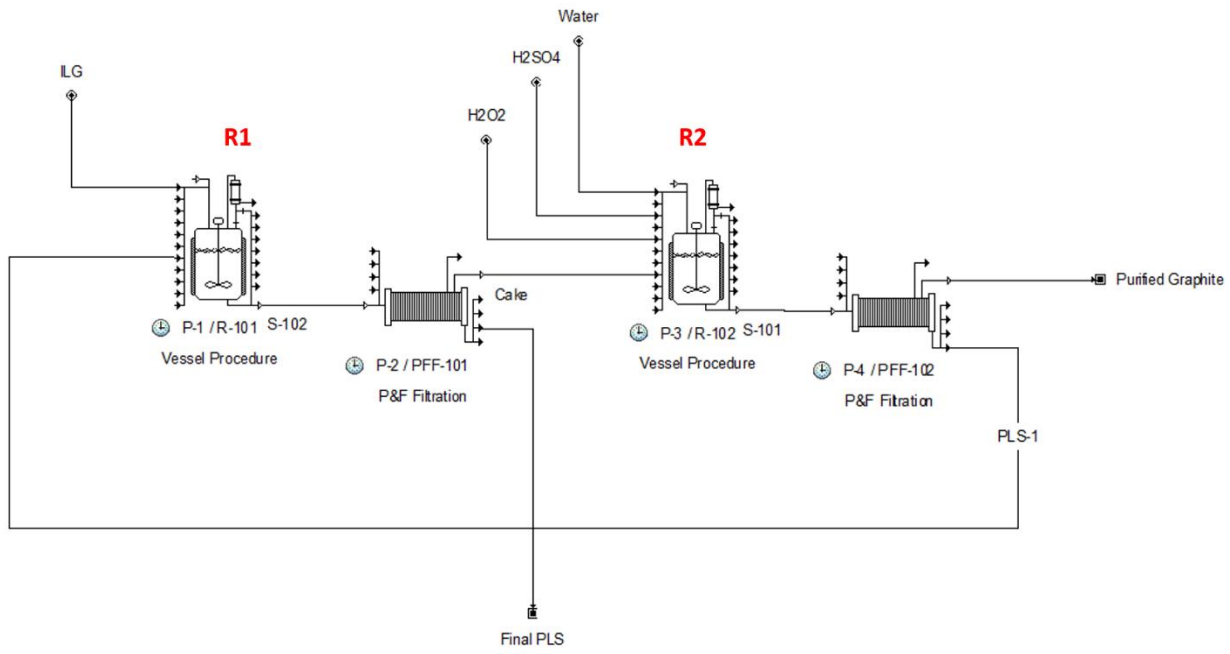

Figure 3. Scheme of the counter-current process applied for the leaching purification of ILG-1.

7.3.2.1.2.1 Room temperature counter-current leaching

In this section, the counter-current leaching results at room temperature are presented. Table 14 summarizes the leaching data from the five leaching tests. Table 15 shows the concentrations of metals in the leaching solutions from the second reactor (R2), specifically the outstreams directed to the first reactor (R1), namely L1, L3, and L5, along with their corresponding washing waters (W1, W3, and W5). Table 16 presents the metal concentrations in the final pregnant leach solutions (PLS), which, in the real process, would be directed to the

electrowinning section for copper recovery; this includes L2 and L4 and their respective washing waters (W2 and W4). Finally, Table 17 shows the impurity levels in the targeted solids (S3 and S5), representing the purified graphite, determined by dissolving a portion of the solid in aqua regia and analysing it by ICP.

As shown in Table 17, significant amounts of impurities, particularly Fe and Cu, remain in the purified samples. Therefore, an additional hydrochloric acid leaching was performed on S5 at two different temperatures under the conditions outlined in Table 18, to attempt further purification. Table 19 presents the impurity levels of the two treated samples, again determined by dissolving a portion of the solid in aqua regia and analysing it with ICP. As shown, there are no significant differences in impurity levels before and after HCl treatment, indicating that HCl leaching was ineffective in removing Fe and Cu (Table 19).

Table 14. Leaching data of the five leaching tests carried out at room temperature (counter-current approach).

Counter-current approach	m (g)	V initial (ml)	V final (ml)	pH	V wash water (ml)	V final wash water (ml)	pH wash water	Solid	Liquid
1st Leaching	40	200	177	0.56	200	198	1.49	S1	L1
2nd Leaching	40	L1	162	0.69	200	196	1.26	S2	L2
3rd Leaching	S2	200	180	0.61	200	195	1.42	S3	L3
4th Leaching	40	L3	163	0.71	200	198	1.42	S4	L4
5th Leaching	S4	200	183	0.43	200	196	1.23	S5	L5

Table 15. Metals concentration in leaching solutions of the second reactor (out streams of R2) which go to the first reactor (R1) (counter current at room temperature).

	mg/L									
	Al	**Ba**	**Ca**	**Mg**	**Na**	**K**	**Li**	**Fe**	**Zn**	**Cu**
L1	15.75	0.08	27.14	13.00	278.60	31.01	0.98	33.43	71.98	14603.80
ww1	1.55	0.03	3.84	1.38	19.30	1.73	0.06	4.01	7.36	1215.32
L3	2.05	0.04	1.15	1.73	9.98	1.33	0.03	3.82	9.49	7028.44
ww3	0.45	0.01	0.74	0.29	4.65	0.21	0.01	1.75	1.17	780.24
L5	1.17	0.04	1.09	1.20	5.96	0.86	0.08	3.27	2.54	1292.08
ww5	0.20	0.01	1.92	0.46	0	0	0.01	2.19	1.25	552.85

Table 16. Metals concentration in the final PLS (out streams of R1), which goes to the electrowinning section (counter-current at room temperature).

	mg/L									
	Al	**Ba**	**Ca**	**Mg**	**Na**	**K**	**Li**	**Fe**	**Zn**	**Cu**
L2	27.83	0.04	87.00	26.42	635.88	65.93	2.07	73.20	122.71	20479.66
ww2	2.40	0.03	7.14	3.14	45.42	3.75	0.13	9.85	14.62	1813.82
L4	15.41	0.03	28.20	15.61	300.48	36.10	0.97	37.05	82.86	22295.89

ww4	1.32	0.02	4.04	1.75	22.53	2.10	0.09	7.17	9.24	2162.74

Table 17. The impurity levels of the purified graphite obtained from ILG-1 (counter-current at room temperature).

	Al (%)	**Ba (%)**	**Ca (%)**	**Mg (%)**	**Na (%)**	**K (%)**	**Li (%)**	**Fe (%)**	**Zn (%)**	**Cu (%)**	**Sum (%)**
S3-1	0.0027	0.0084	0.0353	0.0050	0.0178	0.0048	0.0000	0.0210	0.0033	0.0189	0.1173
S3-2	0.0030	0.0087	0.0180	0.0038	0.0128	0.0017	0.0000	0.0169	0.0017	0.0153	0.0818
S3-3	0.0053	0.0076	0.0276	0.0047	0.0142	0.0024	0.0000	0.0190	0.0029	0.0145	0.0982
S3 (Average)	0.0037	0.0082	0.0270	0.0045	0.0149	0.0030	0.0000	0.0190	0.0027	0.0162	0.0991
S5-1	0.0063	0.0082	0.0241	0.0046	0.0159	0.0026	0.0000	0.0241	0.0025	0.0123	0.1005
S5-2	0.0033	0.0079	0.0212	0.0039	0.0169	0.0033	0.0000	0.0219	0.0033	0.0146	0.0962
S5-3	0.0024	0.0073	0.0241	0.0045	0.0164	0.0021	0.0000	0.0255	0.0022	0.0107	0.0951
S5 (Average)	0.0040	0.0078	0.0231	0.0043	0.0164	0.0026	0.0000	0.0238	0.0027	0.0125	0.0973

Table 18. HCl leaching conditions to treat graphite (S5) after counter-current test at room temperature.

Temperature (°C)	**Time (h)**	**HCl (M)**	**S/L (%)**
25 and 60	2	1	10

Table 19. The impurity levels of the purified graphite after HCl treatment (after counter-current test at room temperature).

	Al (%)	**Ba (%)**	**Ca (%)**	**Mg (%)**	**Na (%)**	**K (%)**	**Li (%)**	**Fe (%)**	**Zn (%)**	**Cu (%)**	**Sum (%)**
Before HCl	0.0040	0.0078	0.0231	0.0043	0.0164	0.0026	0.0000	0.0238	0.0027	0.0125	0.0973
S5-1-25°C	0.0030	0.0056	0.0409	0.0066	0.0101	0.0033	0.0005	0.0318	0.0067	0.0212	0.1295
S5-2-25°C	0.0038	0.0066	0.0350	0.0069	0.0114	0.0027	0.0006	0.0331	0.0034	0.0354	0.1390
S5-3-25°C	0.0037	0.0065	0.0183	0.0038	0.0087	0.0026	0.0005	0.0276	0.0034	0.0151	0.0903
S5-25°C Average	0.0035	0.0062	0.0314	0.0057	0.0101	0.0029	0.0005	0.0308	0.0045	0.0239	0.1196
S5-1-60°C	0.0020	0.0037	0.0451	0.0078	0.0092	0.0019	0.0004	0.0206	0.0026	0.0112	0.1044
S5-2-60°C	0.0036	0.0035	0.0224	0.0043	0.0082	0.0026	0.0005	0.0240	0.0037	0.0128	0.0856
S5-3-60°C	0.0021	0.0037	0.0189	0.0034	0.0067	0.0017	0.0007	0.0233	0.0032	0.0112	0.0749
S5-60°C Average	0.0026	0.0036	0.0288	0.0052	0.0080	0.0020	0.0005	0.0226	0.0032	0.0117	0.0883

7.3.2.1.2.2 High temperature counter-current leaching

In this section, the counter-current leaching results at 70°C are presented. Table 20 summarizes the leaching data from the five leaching tests. Table 21 shows the concentrations of metals in the leaching solutions from the second reactor (R2), specifically the outstreams directed to the first reactor (R1), namely L1, L3, and L5, along with their corresponding washing waters (W1, W3, and W5). Table 22 presents the metal concentrations in the final pregnant leach solutions (PLS), which, in the real process, would be directed to the electrowinning section for copper recovery; this includes L2 and L4 and their respective washing waters (W2 and W4). Finally, Table 23 shows the impurity levels in the targeted solids (S3 and S5), representing the purified graphite, determined by dissolving a portion of the solid in aqua regia and analysing it by ICP.

Table 20. Leaching data of the five leaching tests carried out at 70°C (counter-current approach).

	m (g)	V initial (ml)	V final (ml)	pH	V wash water (ml)	V final wash water (ml)	pH wash water	Solid	Liquid
1st Leaching	40	200	156	0.77	200	195	1.99	S1	L1
2nd Leaching	40	L1	199	0.51	200	195	1.02	S2	L2
3rd Leaching	S2	200	170	0.56	200	193	1.11	S3	L3
4th Leaching	40	L3	138	0.63	200	195	1.32	S4	L4
5th Leaching	S4	200	181	0.44	200	196	1.08	S5	L5

Table 21. Metals concentration in leaching solutions of the second reactor (out streams of R2) which go to the first reactor (R1) (counter current at 70°C).

	mg/L									
	Al	**Ba**	**Ca**	**Mg**	**Na**	**K**	**Li**	**Fe**	**Zn**	**Cu**
L1	17.72	0.10	55.87	14.89	270.53	40.20	0.95	48.78	96.23	18685.64
ww1	1.99	0.02	4.50	2.12	34.23	3.17	0.09	6.95	10.82	2169.50
L3	0.92	0.09	6.51	0.85	11.83	1.44	0.03	3.97	15.04	11878.86
ww3	0.12	0.02	0.54	0.13	0.99	0.14	0.01	0.74	1.50	971.57
L5	0.78	0.14	0.54	0.57	2.11	0.64	0.00	1.82	3.19	2235.15
ww5	0.11	0.02	0.47	0.13	0.31	0.07	0.01	0.44	0.35	219.69

Table 22. Metals concentration in the final PLS (out streams of R1) which goes to the electrowinning section (counter current at 70°C).

	mg/L									
	Al	**Ba**	**Ca**	**Mg**	**Na**	**K**	**Li**	**Fe**	**Zn**	**Cu**
L2	42.15	0.12	88.67	30.74	692.77	66.80	2.44	174.84	210.37	25461.28
ww2	6.88	0.03	14.07	6.78	100.55	13.95	0.35	32.23	32.84	4462.80
L4	21.22	0.11	43.61	14.96	337.10	50.60	1.17	98.30	118.50	27237.93
ww4	1.90	0.03	4.19	1.74	32.80	3.19	0.09	9.26	11.07	2815.36

Table 23. The impurity levels of the purified graphite obtained from ILG-1 (counter current at 70°C).

	Al (%)	Ba (%)	Ca (%)	Mg (%)	Na (%)	K (%)	Li (%)	Fe (%)	Zn (%)	Cu (%)	Sum (%)
S3-1	0.0016	0.0078	0.0095	0.0016	0.0247	0.0014	0.0000	0.0147	0.0010	0.1540	0.2163
S3-2	0.0025	0.0080	0.0067	0.0015	0.0070	0.0022	0.0002	0.0072	0.0012	0.0406	0.0772
S3-3	0.0023	0.0077	0.0081	0.0011	0.0064	0.0022	0.0002	0.0055	0.0014	0.0791	0.1140
S3 (Average)	0.0021	0.0078	0.0081	0.0014	0.0127	0.0019	0.0001	0.0091	0.0012	0.0912	0.1358
S5-1	0.0020	0.0048	0.0085	0.0015	0.0069	0.0014	0.0000	0.0065	0.0007	0.0139	0.0461
S5-2	0.0016	0.0055	0.0061	0.0012	0.0063	0.0012	0.0000	0.0054	0.0013	0.0131	0.0417
S5-3	0.0019	0.0042	0.0065	0.0011	0.0065	0.0013	0.0002	0.0063	0.0014	0.0125	0.0420
S5 (Average)	0.0018	0.0048	0.0070	0.0013	0.0066	0.0013	0.0001	0.0061	0.0011	0.0132	0.0433

As shown in Table 23, significant amounts of impurities, particularly Fe and Cu, were removed in the purified samples. To confirm these results and validate the overall process, an additional series of counter-current tests was conducted under similar conditions. The results of the replicated experiments are presented in Tables 24 to 27.

Table 27 presents the impurity levels of the final purified sample, determined by dissolving a portion of the solid in aqua regia and analysing it using ICP. As shown, there are no significant differences in impurity levels between the two replicated series of experiments conducted at 70°C (Table 23 and Table 27), confirming the effectiveness of the counter-current process at 70°C in removing most of the Fe and Cu impurities.

Table 24. Leaching data of the five leaching tests carried out at 70°C (replicate of counter-current tests).

	m (g)	V initial (ml)	V final (ml)	pH	V wash water (ml)	V final wash water (ml)	pH wash water	Solid	Liquid
1st Leaching	40	200	153	0.55	200	192	1.11	S1	L1
2nd Leaching	40	L1	115	0.55	200	194	1.29	S2	L2
3rd Leaching	S2	200	168	0.54	200	198	1.1	S3	L3
4th Leaching	40	L3	136	0.59	200	193	1.14	S4	L4
5th Leaching	S4	200	160	0.54	200	194	0.98	S5	L5

Table 25. Metals concentration in leaching solutions of the second reactor (out streams of R2) which go to the first reactor (R1) (replicate of counter current tests at 70°C).

	mg/L									
	Al	**Ba**	**Ca**	**Mg**	**Na**	**K**	**Li**	**Fe**	**Zn**	**Cu**
L1	18.14	0.11	29.18	11.91	345.49	36.44	1.04	45.50	67.91	14481.64

ww1	2.54	0.02	4.68	2.25	42.40	3.69	0.13	7.81	12.46	2714.61
L3	0.62	0.10	0.51	0.40	5.64	0.77	0.01	1.53	9.00	9010.96
ww3	0.08	0.02	0.85	0.16	0.66	0.12	0.00	0.51	1.07	904.11
L5	1.00	0.12	0.80	0.80	4.74	0.64	0.01	2.69	2.82	2026.49
ww5	0.66	0.02	1.14	0.29	0.64	0.12	0.00	0.60	0.57	292.08

Table 26. Metals concentration in the final PLS (out streams of R1), which goes to the electrowinning section (replicate of counter current tests at 70°C).

	mg/L									
	Al	**Ba**	**Ca**	**Mg**	**Na**	**K**	**Li**	**Fe**	**Zn**	**Cu**
L2	44.55	0.20	62.75	26.54	678.10	57.45	2.68	157.11	180.91	24127.53
ww2	4.06	0.02	6.17	3.29	69.78	6.03	0.21	15.67	18.73	3144.51
L4	21.40	0.12	30.47	13.46	325.71	27.51	1.19	92.92	107.18	22885.71
ww4	2.41	0.02	3.55	1.88	36.91	3.20	0.11	10.09	11.73	2508.84

Table 27. The impurity levels of the purified graphite obtained from ILG-1 (replicate of counter-current tests at 70°C).

	Al (%)	**Ba (%)**	**Ca (%)**	**Mg (%)**	**Na (%)**	**K (%)**	**Li (%)**	**Fe (%)**	**Zn (%)**	**Cu (%)**	**Sum (%)**
S5-1	0.0022	0.0058	0.0198	0.0046	0.0111	0.0021	0.0000	0.0041	0.0012	0.0153	0.0663
S5-2	0.0018	0.0052	0.0080	0.0017	0.0098	0.0013	0.0000	0.0035	0.0008	0.0125	0.0446
S5-3	0.0017	0.0058	0.0183	0.0036	0.0097	0.0014	0.0000	0.0030	0.0006	0.0141	0.0583
S5 (Average)	0.0019	0.0056	0.0154	0.0033	0.0102	0.0016	0.0000	0.0036	0.0009	0.0140	0.0564

7.3.3 Characterization of the purified graphite

The final purified graphite (S5), which is Graphite for Lithium-ion Batteries (GLIB), was subsequently characterized using various analytical techniques, as discussed in the following subsections.

7.3.3.1 XRF

The purified graphite was analysed using XRF to identify residual impurities. Table 28 presents the XRF results for this sample, while Table 29 reports the major impurities, estimated in the form of oxides.

Table 28. XRF analysis of the final purified graphite obtained from ILG-1 (counter-current leaching at 70°C).

Element	**(%)**	**Element**	**(%)**	**Element**	**(%)**
Na	0.260	**As**	<0.00005	**Nd**	0.00126
Mg	0.00239	**Se**	<0.00005	**HF**	<0.00010
Al	<0.0020	**Br**	0.00010	**Ta**	0.00156

Si	0.6242	**Rb**	0.00003	**W**	<0.00010
P	<0.00030	**Sr**	0.00022	**Hg**	<0.00010
S	0.04340	**Y**	0.00027	**Tl**	<0.00010
Cl	0.00432	**Zr**	0.01094	**Pb**	0.00008
K	0.00422	**Nb**	0.00011	**Bi**	<0.00010
Ca	<0.0010	**Mo**	0.00030	**Th**	0.00007
Ti	0.00700	**Ag**	0.00111	**U**	0.00005
V	0.00046	**Cd**	0.00062		
Cr	0.00380	**Sn**	0.00310		
Mn	<0.00010	**Sb**	0.00177		
Fe	0.00896	**Te**	0.00220		
Co	<0.00030	**I**	0.00090		
Ni	0.00158	**Cs**	<0.00040		
Cu	0.02479	**Ba**	0.01198		
Zn	0.00162	**La**	<0.00020		
Ga	<0.00005	**Ce**	<0.00020		
Ge	<0.00005	**Pr**	0.00120		

Table 29. Estimated major impurities in the final purified graphite obtained from ILG-1 (counter-current leaching at 70°C).

Impurity	**SiO_2**	**ZrO_2**	**Cu**	**Sum**	**Graphite Purity**
Wt. %	1.3350	0.0147	0.0135	1.3632	**98.58%**

7.3.3.2 ICP

The purity of the purified graphite was determined in the previous section by dissolving a portion of the graphite in aqua regia and analysing it using ICP. Table 23 and Table 27 present the ICP results.

7.3.3.3 TGA

The purified graphite was further characterized by TGA to evaluate weight loss during heating. The sample was heated in air up to 1100 °C at a constant rate of 5 °C/min. The results are presented in Figure 4. As can be seen, the total weight loss up to 1100 °C is about 98.6%, which is in accordance with the ash content of the sample (Table 29).

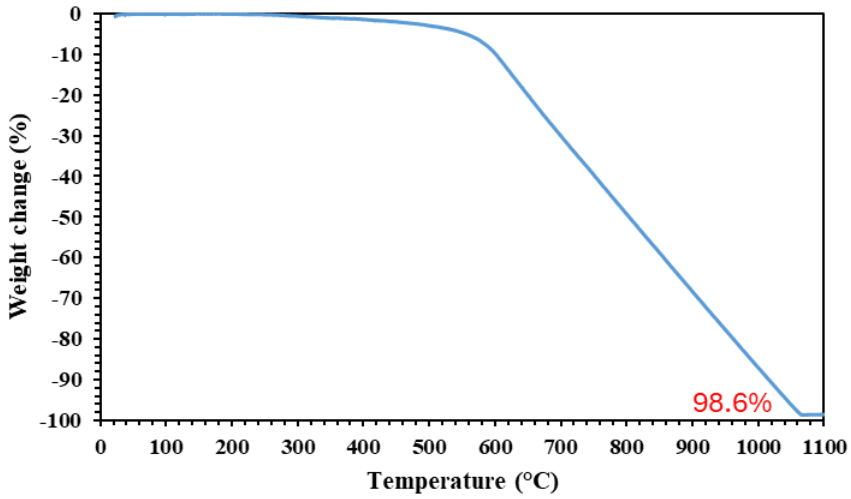

Figure 4. TGA graph of the final purified graphite obtained from ILG-1 (counter-current leaching at 70°C).

7.3.3.4 CHNS

CHNS analysis was conducted to determine the carbon content of the purified graphite. As shown in Table 30, the purified graphite contains approximately 91% carbon, which is significantly lower than expected and inconsistent with the results obtained from TGA and XRF analyses. This discrepancy may be attributed to measurement errors associated with the very small sample size analysed, which is only a few milligrams.

Table 30. CHNS analysis results for the final purified graphite obtained from ILG-1 (counter-current leaching at 70°C).

Run	Mass (mg)	C (%)	H (%)	N (%)	S (%)
1	2.55	96.4	0.1	0.76	0
2	4.48	85.07	0.07	0.81	0
Average		90.74	0.09	0.79	0

7.3.3.5 PSD

The particle size distribution of the purified graphite was also analysed. The results are presented in Table 31 and illustrated in Figure 5.

Table 31. PSD results for the final purified graphite obtained from ILG-1 (counter-current leaching at 70°C).

	mm
D (0.1)	12.191
D (0.5)	38.575

D (0.9)	213.081

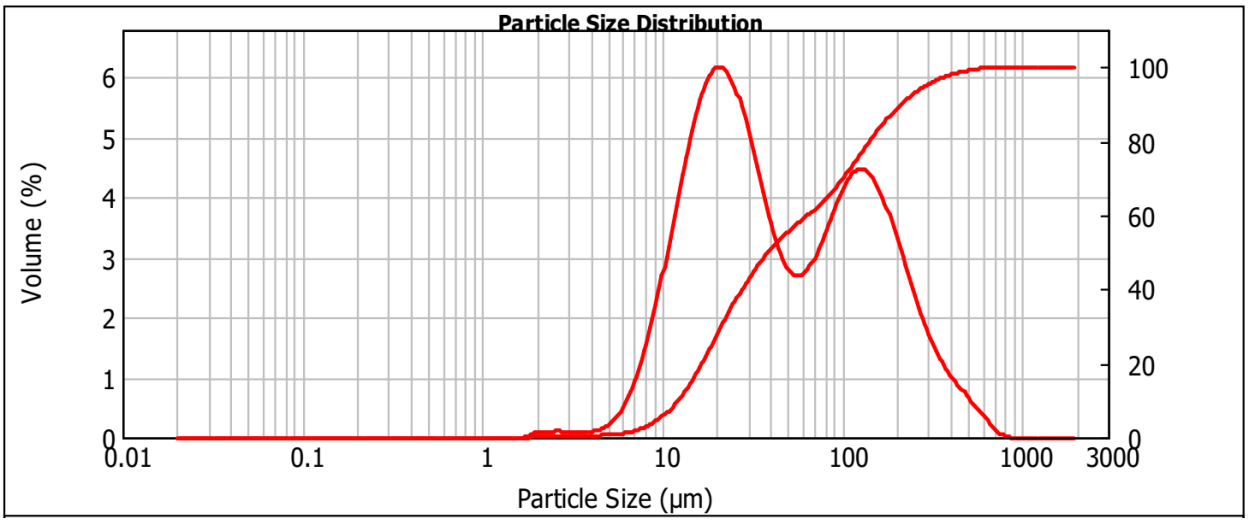

Figure 5. PSD of the final purified graphite obtained from ILG-1 (counter-current leaching at 70°C).

7.3.4 Final purity of the obtained graphite

According to Table 27, the total sum of elemental impurities in the S5 solid (obtained after counter-current leaching) is **0.0564.** And according to Table 29, the sum of other impurities in the form of silica and oxides is **1.3632.** So, the overall purity of the final graphite obtained after countercurrent leaching at 70°C is **98.58%**. It was also observed that there was no significant difference between the counter-current leaching at room temperature and at 70°C.

7.4 Conclusions

This chapter includes the overall purification process for the recovery of graphite from the spent lithium-ion batteries. The as-received sample was referred to as impure lithium graphite (ILG), and the characterization of this sample was done to find the initial impurities. A counter-current leaching approach was applied to remove possible impurities using H_2SO_4 and H_2O_2. These tests were conducted at room temperature as well as at 70°C with a solid to liquid ratio of 20%. It was found that this technique was useful in removing the maximum impurities (Table 27). The sum of impurities in the elemental form was around 0.056%. The main impurities that could not be removed were silica and oxides (ZrO_2) of some elements (Table 29), and the total sum of impurities was 1.36%, resulting in a high-purity graphite with a purity of 98.58%.

CHAPTER 8

Summary and Future Directions

This research focuses on the recovery of valuable metals such as Li, Co, Mn, Cu, Fe, Al, and graphite from spent Li-ion battery waste and K, Mn, Zn, and graphite from the spent alkaline batteries obtained from the automotive sector. A more efficient and reliable method was developed for the recovery process. Instead of the conventional method, integrated hydrometallurgical processes were employed in this research for the recovery of alkaline and lithium-ion batteries. This chapter provides a summary of the different topics studied in this thesis by utilizing different analytical methods and techniques, and optimized recovery processes.

A general and detailed introduction, including the overall representation of the whole thesis, was covered in Chapter 1. Following this, Chapter 2, the basic knowledge, principles, and advantages of the analytical method and techniques used in this research work. The most important part of my research is represented in the following chapters. Chapter 3 describes a comparative study on the recovery of K, Mn, and Zn from spent alkaline batteries. These elements were recovered from the black mass in the form of their nitrates using HNO_3 or sulphates with H_2SO_4. Each recovery route has its own advantages. For instance, the nitrate recovery route could have a yield of marketable potassium salts [KNO_3 and Zn $(NO_3)_2$], while the sulfate route can give fertilizer-grade zinc salt ($ZnSO_4$) and battery-grade manganese salt ($MnSO_4$) due to high purity and selectivity. It was also observed that there is a possibility of decreasing H_2SO_4 and H_2O_2 consumption in the reductive leaching of manganese by increasing leaching time and using higher temperatures. This study could be more aligned with sustainable chemical engineering principles, with minimum reagent consumption and no effect on the recovery yield.

Chapter 4 introduces a comprehensive and scalable approach for the selective recovery of metals from spent LIBs, tackling the technical and environmental challenges associated with LIBs recycling. By optimizing critical parameters such as pH, saponification value, and stripping conditions, an efficient extraction of the elements was achieved. Copper recovery experiments revealed that the optimal ratio of Fe-Cu of 1.2 is sufficient to achieve 85% Cu recovery. Iron and aluminum removal was conducted at a pH of 5.5. The ideal pH for Mn extraction was determined to be 3, resulting in an extraction efficiency of about 92%, using a 15% saponified D2EHPA diluted in n-heptane. Cyanex 272 demonstrated efficacy as an

extractant for cobalt recovery, achieving approximately 91% extraction efficiency at a pH of 4.5. A mathematical model was also studied for the extraction of Mn, Co, and Ni.

After that, the hydrometallurgical recovery of Li and Fe from spent $LiFePO_4$ batteries was successfully optimized as a detailed description was given in chapter 5. A factorial design approach was applied to develop a statistical model for predicting Li extraction efficiency based on key process variables. The optimized conditions, i.e., H_2SO_4 (3 N), 350 rpm agitation, and a 20% solid-to-liquid ratio, revealed a high Li recovery (~90.8%), minimal Al dissolution (2.0%), and excellent Fe recovery (98.0%). These findings highlight the effectiveness of factorial design in optimizing leaching parameters. Oxalic acid precipitation at stoichiometric levels achieved 98.1% Fe removal with only 2% Li loss, and found the best approach for selective precipitation of Fe and Li from solution.

In chapter 6, the recovery of graphite from the exhausted black mass of alkaline spent batteries was investigated. Accordingly, a binary system comprising a strong acid (H_2SO_4 or HCl) and a reducing agent (H_2O_2 or citric acid, $C_6H_8O_7$) was evaluated as the primary purification system. In this study, a combination of H_2SO_4 with two reducing agents was investigated by a fractional factorial design. Different leaching conditions, such as temperature, time, and rpm, were also investigated. The optimal condition was determined from the H_2SO_4 + citric acid system (corresponding to Run 6 in Table 17 of Chapter 6) involving leaching in a solution containing 1 M H_2SO_4 and 0.5 M citric acid for 3 hours at 60°C, using a solid-to-liquid ratio of 10%. After that, a two-step further purification was done using HCl and EDTA. The purity of the final graphite obtained was 94.25%.

At the end, we also studied the recovery of graphite from lithium spent batteries, as explained in Chapter 7. A counter-current leaching approach was applied, which is more convenient than the conventional method to remove possible impurities using H_2SO_4 and H_2O_2. These tests were conducted at room temperature as well as at 70°C with a solid-to-liquid ratio of 20%. The sum of impurities in the elemental form was around 0.056%. The main impurities that could not be removed were silica and oxides (ZrO_2) of some elements (Table 29), and the total sum of impurities was 1.36%, resulting in a high-purity graphite with a purity of 98.58%.

The future direction of the recovery process for elements and graphite from spent batteries is the development of greener and more selective extraction paths, along with environmental sustainability, while lowering the battery waste and minimizing chemical consumption, and a global push towards the greener materials supply chain. Additionally, scalable process

integration, combining hydrometallurgy, membrane separations, and AI-driven optimization, will be essential to maximize recovery efficiency, reduce energy consumption, and enable economically viable, closed-loop recycling systems.

References

[1] D. L. Thompson *et al.*, "The importance of design in lithium ion battery recycling–a critical review," *Green Chemistry*, vol. 22, no. 22, pp. 7585–7603, 2020.

[2] J. Neumann *et al.*, "Recycling of Lithium-Ion Batteries—Current State of the Art, Circular Economy, and Next Generation Recycling," May 01, 2022, *John Wiley and Sons Inc*. doi: 10.1002/aenm.202102917.

[3] N. Akhmetov, A. Manakhov, and A. S. Al-Qasim, "Li-Ion Battery Cathode Recycling: An Emerging Response to Growing Metal Demand and Accumulating Battery Waste," *Electronics (Basel)*, vol. 12, no. 5, p. 1152, 2023.

[4] R. Sommerville, P. Zhu, M. A. Rajaeifar, O. Heidrich, V. Goodship, and E. Kendrick, "A qualitative assessment of lithium ion battery recycling processes," *Resour Conserv Recycl*, vol. 165, p. 105219, 2021.

[5] Y. Dong *et al.*, "Trends of sustainable recycling technology for lithium-ion batteries: Metal recovery from conventional metallurgical processes to innovative direct recycling," *MetalMat*, vol. 1, no. 1, p. e5, 2024.

[6] M. Svärd, C. Ma, K. Forsberg, and P. G. Schiavi, "Addressing the Reuse of Deep Eutectic Solvents in Li-Ion Battery Recycling: Insights into Dissolution Mechanism, Metal Recovery, Regeneration and Decomposition," 2024, *John Wiley and Sons Inc*. doi: 10.1002/cssc.202400410.

[7] M. Bukvić, B. Stojanovic, L. Ivanović, and S. Milojević, "Recycling of the Hybrid and Electric Vehicles," *ACTA TECHNICA CORVINIENSIS–Bulletin of Engineering*, 2017.

[8] L. An, "Recycling of spent lithium-ion batteries," *Processing Methods and Environmental Impacts*, 2019.

[9] G. Harper *et al.*, "Recycling lithium-ion batteries from electric vehicles," *Nature*, vol. 575, no. 7781, pp. 75–86, 2019.

[10] X. Zeng, J. Li, and N. Singh, "Recycling of spent lithium-ion battery: a critical review," *Crit Rev Environ Sci Technol*, vol. 44, no. 10, pp. 1129–1165, 2014.

[11] S. M. Shin, N. H. Kim, J. S. Sohn, D. H. Yang, and Y. H. Kim, "Development of a metal recovery process from Li-ion battery wastes," *Hydrometallurgy*, vol. 79, no. 3–4, pp. 172–181, 2005.

[12] D. H. P. Kang, M. Chen, and O. A. Ogunseitan, "Potential environmental and human health impacts of rechargeable lithium batteries in electronic waste," *Environ Sci Technol*, vol. 47, no. 10, pp. 5495–5503, 2013.

[13] H. Bian *et al.*, “Transforming Organic Solid Waste Management: Embracing Humification for Sustainable Resource Recovery,” *ACS Sustainable Resource Management*, vol. 1, no. 2, pp. 181–198, 2024.

[14] M. López *et al.*, “E-waste dismantling as a source of personal exposure and environmental release of fine and ultrafine particles,” *Science of the Total Environment*, vol. 833, p. 154871, 2022.

[15] C. Achillas, D. Aidonis, C. Vlachokostas, A. Karagiannidis, N. Moussiopoulos, and V. Loulos, “Depth of manual dismantling analysis: A cost-benefit approach,” *Waste Management*, vol. 33, no. 4, pp. 948–956, Apr. 2013, doi: 10.1016/j.wasman.2012.12.024.

[16] J. Guo, X. Li, X. Xing, and Z. Shao, “Recycling, Regeneration, and Reutilization of Cathode Materials of Spent LiNixCoyMn (1-xy) O2 Batteries,” *J Environ Chem Eng*, p. 114740, 2024.

[17] W. Ding *et al.*, “A green cycle strategy for selective leach and recovery of critical metals from spent lithium-ion batteries: experimental and new mechanistic insights,” *J Hazard Mater*, p. 137368, 2025.

[18] C. Zhou, B. Engelen, I. Zaplana, and J. Peeters, “Design of a robotic system for battery dismantling from tablets,” in *Procedia CIRP*, Elsevier B.V., 2022, pp. 273–277. doi: 10.1016/j.procir.2022.02.045.

[19] T. Younas, H. Shalchian, M. Ullah, F. Vegliò, and V. Innocenzi, “Optimizing dismantling approaches for recycling of li-ion batteries: Strategies, challenges and economic analysis,” *J Energy Storage*, vol. 132, p. 117918, 2025.

[20] H. Li *et al.*, “Enhancing Lithium Recycling Efficiency in Pyrometallurgical Processing through Thermodynamic-Based Optimization and Design of Spent Lithium-Ion Battery Slag Compositions,” *ACS Sustainable Resource Management*, 2024.

[21] O. Kwon and I. L. Sohn, “Fundamental thermokinetic study of a sustainable lithium-ion battery pyrometallurgical recycling process,” *Resour Conserv Recycl*, vol. 158, p. 104809, 2020.

[22] A. Liu, G. Hu, Y. Wu, and F. Guo, “Life cycle environmental impacts of pyrometallurgical and hydrometallurgical recovery processes for spent lithium-ion batteries: present and future perspectives,” *Clean Technol Environ Policy*, vol. 26, no. 2, pp. 381–400, 2024.

[23] J. Wang *et al.*, “Toward Direct Regeneration of Spent Lithium-Ion Batteries: A Next-Generation Recycling Method,” *Chem Rev*, vol. 124, no. 5, pp. 2839–2887, 2024.

[24] J. J. Roy *et al.*, “Direct recycling of Li-ion batteries from cell to pack level: Challenges and prospects on technology, scalability, sustainability, and economics,” Jun. 01, 2024, *John Wiley and Sons Inc*. doi: 10.1002/cey2.492.

[25] B. K. Biswal, B. Zhang, P. T. M. Tran, J. Zhang, and R. Balasubramanian, “Recycling of spent lithium-ion batteries for a sustainable future: recent advancements,” *Chem Soc Rev*, 2024.

[26] Z. Wu, H. Zhu, H. Bi, P. He, and S. Gao, “Recycling of electrode materials from spent lithium-ion power batteries via thermal and mechanical treatments,” *Waste Management & Research*, vol. 39, no. 4, pp. 607–619, 2021.

[27] X. Dai *et al.*, “Selective leaching of lithium from mixed spent lithium iron phosphate powder,” *J Environ Chem Eng*, vol. 12, no. 5, p. 114091, 2024.

[28] X. Dai *et al.*, “Selective leaching of lithium from mixed spent lithium iron phosphate powder,” *J Environ Chem Eng*, vol. 12, no. 5, p. 114091, 2024.

[29] M. Colledani, L. Gentilini, E. Mossali, and N. Picone, “A novel mechanical pre-treatment process-chain for the recycling of Li-Ion batteries,” *CIRP Annals*, vol. 72, no. 1, pp. 17–20, 2023.

[30] D. M. Werner, T. Mütze, and U. A. Peuker, “Influence of pretreatment strategy on the crushing of spent lithium-ion batteries,” *Metals (Basel)*, vol. 12, no. 11, p. 1839, 2022.

[31] S. Windisch-Kern *et al.*, “Recycling chains for lithium-ion batteries: A critical examination of current challenges, opportunities and process dependencies,” *Waste management*, vol. 138, pp. 125–139, 2022.

[32] L. Zhao *et al.*, “Recovery of electrode materials from a spent lithium-ion battery through a pyrolysis-coupled mechanical milling method,” *Energy & Fuels*, vol. 38, no. 2, pp. 1310–1318, 2024.

[33] H. Yang *et al.*, “Recent advances in ball-milling-based silicon anodes for lithium-ion batteries,” *Energies (Basel)*, vol. 16, no. 7, p. 3099, 2023.

[34] M. Kosfeld, B. Westphal, and A. Kwade, “Moisture behavior of lithium-ion battery components along the production process,” *J Energy Storage*, vol. 57, p. 106174, 2023.

[35] X. Han, S. Xia, J. Cao, C. Wang, and M. Chen, “Effect of humidity on properties of lithium-ion batteries,” *Int J Electrochem Sci*, vol. 16, no. 5, p. 210554, 2021.

[36] G. Yan, J. Zhang, L. Zhao, S. Liu, X. Gao, and M. Wang, “Research on the method to determine the loss on ignition of electrode materials from spent lithium-ion battery,” *J Environ Chem Eng*, p. 118169, 2025.

[37] H. Anticoi, L. Garcia, G. Dan, P. Sola, and A. D. Dorado, “Methodology for evaluation of lithium-ion black-mass battery recycling,” *J Mater Cycles Waste Manag*, vol. 27, no. 2, pp. 1019–1033, 2025.

[38] B. Lu *et al.*, “High-efficiency leaching of valuable metals from waste Li-ion batteries using deep eutectic solvents,” *Environ Res*, vol. 212, p. 113286, 2022.

[39] L. F. Guimarães, A. B. B. Junior, and D. C. R. Espinosa, “Sulfuric acid leaching of metals from waste Li-ion batteries without using reducing agent,” *Miner Eng*, vol. 183, p. 107597, 2022.

[40] W. Xuan, A. de Souza Braga, and A. Chagnes, “Development of a novel solvent extraction process to recover cobalt, nickel, manganese, and lithium from cathodic materials of spent lithium-ion batteries,” *ACS Sustain Chem Eng*, vol. 10, no. 1, pp. 582–593, 2021.

[41] V. Chaudhary, P. Lakhera, K.-H. Kim, A. Deep, and P. Kumar, “Insights into the eco-friendly recovery process for valuable metals from waste lithium-ion batteries by organic acids leaching,” *Separation & Purification Reviews*, vol. 53, no. 1, pp. 82–99, 2024.

[42] J. Shuai *et al.*, “Efficient extraction and separation of valuable elements from spent lithium-ion batteries by leaching and solvent extraction: A review,” *Chemical Engineering Journal*, vol. 503, p. 158114, 2025.

[43] B. Zhou, H. Su, W. Liu, Z. Zhu, L. Wang, and T. Qi, “Solvent extraction of metal ions from the leaching solutions of waste lithium-ion battery materials: A review,” *Sep Purif Technol*, vol. 354, p. 129173, 2025.

[44] S. Lei, W. Sun, and Y. Yang, “Solvent extraction for recycling of spent lithium-ion batteries,” *J Hazard Mater*, vol. 424, p. 127654, 2022.

[45] J. Shuai *et al.*, “Efficient extraction and separation of valuable elements from spent lithium-ion batteries by leaching and solvent extraction: A review,” *Chemical Engineering Journal*, vol. 503, p. 158114, 2025.

[46] S. Gu, L. Zhang, B. Fu, X. Wang, and J. W. Ahn, “Feasible route for the recovery of strategic metals from mixed lithium-ion batteries cathode materials by precipitation and carbonation,” *Chemical Engineering Journal*, vol. 420, p. 127561, 2021.

[47] X. Yang, Y. Zhang, Q. Meng, P. Dong, P. Ning, and Q. Li, “Recovery of valuable metals from mixed spent lithium-ion batteries by multi-step directional precipitation,” *RSC Adv*, vol. 11, no. 1, pp. 268–277, 2021.

[48] T.-N. Kröger *et al.*, “Direct investigation of the interparticle-based state-of-charge distribution of polycrystalline NMC532 in lithium ion batteries by classification-single-particle-ICP-OES,” *J Power Sources*, vol. 527, p. 231204, 2022.

[49] K. Neubauer, “Using ICP-OES to Improve Lithium-Ion Battery Performance and Reduce Waste,” 2023.

[50] B. Pelletier-Villeneuve, B. Krueger, J. R. Adsetts, M.-C. Ricard, B. Ruchte, and S. B. Schougaard, “Measuring Electrolyte Salt Concentration Gradients in Lithium-Ion Batteries using Benchtop μ-XRF,” *ACS Electrochemistry*, vol. 1, no. 10, pp. 1972–1976, 2025.

[51] C. Korbel *et al.*, “Quantification of lithium using handheld instruments: application of LIBS and XRF spectroscopy to assay the lithium content of mineral processing products,” *J Anal At Spectrom*, vol. 39, no. 7, pp. 1838–1853, 2024.

[52] I. Mantouvalou *et al.*, “Operando Measurement of Transition Metal Deposition in a NMC Li-Ion Battery Using Laboratory Confocal Micro-X-ray Fluorescence Spectroscopy,” *Small*, p. 2502460, 2025.

[53] M. Arif, Y. Li, M. M. El-Dalatony, C. Zhang, X. Li, and E.-S. Salama, “A complete characterization of microalgal biomass through FTIR/TGA/CHNS analysis: An approach for biofuel generation and nutrients removal,” *Renew Energy*, vol. 163, pp. 1973–1982, 2021.

[54] J. Epp, “X-ray diffraction (XRD) techniques for materials characterization,” in *Materials characterization using nondestructive evaluation (NDE) methods*, Elsevier, 2016, pp. 81–124.

[55] P. S. Quinn and A. Benzonelli, “XRD and materials analysis,” *Encycl. Archaeol. Sci*, pp. 1–5, 2018.

[56] B. H. Kaye, “Particle size characterization,” in *Handbook of Powder Science & Technology*, Springer, 1997, pp. 1–34.

[57] R. B. Prime, H. E. Bair, S. Vyazovkin, P. K. Gallagher, and A. Riga, “Thermogravimetric analysis (TGA),” *Thermal analysis of polymers: Fundamentals and applications*, pp. 241–317, 2009.

[58] J. Thakur, P. Phogat, R. Jha, and S. Singh, “Non-rechargeable batteries: a review of primary battery technology and future trends,” *Physical Chemistry Chemical Physics*, 2025.

[59] L.-H. Tran, K. Tanong, A. D. Jabir, G. Mercier, and J.-F. Blais, “Hydrometallurgical process and economic evaluation for recovery of zinc and manganese from spent alkaline batteries,” *Metals (Basel)*, vol. 10, no. 9, p. 1175, 2020.

[60] E. Sayilgan *et al.*, “A review of technologies for the recovery of metals from spent alkaline and zinc–carbon batteries,” *Hydrometallurgy*, vol. 97, no. 3–4, pp. 158–166, 2009.

[61] S. Recknagel, H. Radant, and R. Kohlmeyer, “Survey of mercury, cadmium and lead content of household batteries,” *Waste management*, vol. 34, no. 1, pp. 156–161, 2014.

[62] F. Ferella, I. De Michelis, and F. Veglio, “Process for the recycling of alkaline and zinc–carbon spent batteries,” *J Power Sources*, vol. 183, no. 2, pp. 805–811, 2008.

[63] B. Ebin, M. Petranikova, B.-M. Steenari, and C. Ekberg, “Production of zinc and manganese oxide particles by pyrolysis of alkaline and Zn–C battery waste,” *Waste Management*, vol. 51, pp. 157–167, 2016.

[64] G. Belardi *et al.*, “Characterization of spent zinc–carbon and alkaline batteries by SEM-EDS, TGA/DTA and XRPD analysis,” *Thermochim Acta*, vol. 526, no. 1–2, pp. 169–177, 2011.

[65] M. V Gallegos, L. R. Falco, M. A. Peluso, J. E. Sambeth, and H. J. Thomas, “Recovery of manganese oxides from spent alkaline and zinc–carbon batteries. An application as catalysts for VOCs elimination,” *Waste management*, vol. 33, no. 6, pp. 1483–1490, 2013.

[66] G. Belardi, R. Lavecchia, F. Medici, and L. Piga, “Thermal treatment for recovery of manganese and zinc from zinc–carbon and alkaline spent batteries,” *Waste Management*, vol. 32, no. 10, pp. 1945–1951, 2012.

[67] I. De Michelis, F. Ferella, E. Karakaya, F. Beolchini, and F. Vegliò, “Recovery of zinc and manganese from alkaline and zinc-carbon spent batteries,” *J Power Sources*, vol. 172, no. 2, pp. 975–983, 2007.

[68] G. Senanayake *et al.*, "Comparative leaching of spent zinc-manganese-carbon batteries using sulfur dioxide in ammoniacal and sulfuric acid solutions," *Hydrometallurgy*, vol. 105, no. 1–2, pp. 36–41, 2010.

[69] M. Buzatu, S. Săceanu, V. G. Ghica, G. Iacob, and T. Buzatu, "Simultaneous recovery of Zn and MnO2 from used batteries, as raw materials, by electrolysis," *Waste management*, vol. 33, no. 8, pp. 1764–1769, 2013.

[70] N. M. García, B. Delgado Cano, J. L. Valverde, M. Heitz, and A. Avalos Ramirez, "Extraction and separation of potassium, zinc and manganese issued from spent alkaline batteries by a three-unit hydrometallurgical process," *Journal of Chemical Technology & Biotechnology*, vol. 99, no. 7, pp. 1553–1563, 2024.

[71] L. An, "Recycling of spent lithium-ion batteries," *Processing Methods and Environmental Impacts*, 2019.

[72] G. Harper *et al.*, "Recycling lithium-ion batteries from electric vehicles," *Nature*, vol. 575, no. 7781, pp. 75–86, 2019.

[73] N. Akhmetov, A. Manakhov, and A. S. Al-Qasim, "Li-ion battery cathode recycling: an emerging response to growing metal demand and accumulating battery waste," *Electronics (Basel)*, vol. 12, no. 5, p. 1152, 2023.

[74] M. P. Dos Santos *et al.*, "A technology for recycling lithium-ion batteries promoting the circular economy: The RecycLib," *Resour Conserv Recycl*, vol. 175, p. 105863, 2021.

[75] J. Diekmann *et al.*, "Potential dangers during the handling of lithium-ion batteries," in *Recycling of Lithium-Ion Batteries: The LithoRec Way*, Springer, 2017, pp. 39–51.

[76] R. Golmohammadzadeh, F. Faraji, and F. Rashchi, "Recovery of lithium and cobalt from spent lithium ion batteries (LIBs) using organic acids as leaching reagents: A review," *Resour Conserv Recycl*, vol. 136, pp. 418–435, 2018.

[77] G. Dorella and M. B. Mansur, "A study of the separation of cobalt from spent Li-ion battery residues," *J Power Sources*, vol. 170, no. 1, pp. 210–215, 2007.

[78] X. Zheng *et al.*, "A mini-review on metal recycling from spent lithium ion batteries," *Engineering*, vol. 4, no. 3, pp. 361–370, 2018.

[79] A. Liu, G. Hu, Y. Wu, and F. Guo, "Life cycle environmental impacts of pyrometallurgical and hydrometallurgical recovery processes for spent lithium-ion batteries: present and future perspectives," *Clean Technol Environ Policy*, vol. 26, no. 2, pp. 381–400, 2024.

[80] S. M. Shin, N. H. Kim, J. S. Sohn, D. H. Yang, and Y. H. Kim, "Development of a metal recovery process from Li-ion battery wastes," *Hydrometallurgy*, vol. 79, no. 3–4, pp. 172–181, 2005.

[81] L. Zhou, A. Garg, J. Zheng, L. Gao, and K. Oh, "Battery pack recycling challenges for the year 2030: Recommended solutions based on intelligent robotics for safe and efficient disassembly, residual energy detection, and secondary utilization," *Energy Storage*, vol. 3, no. 3, p. e190, 2021.

[82] R. E. Ciez and J. F. Whitacre, “Examining different recycling processes for lithium-ion batteries,” *Nat Sustain*, vol. 2, no. 2, pp. 148–156, 2019.

[83] O. Kwon and I. L. Sohn, “Fundamental thermokinetic study of a sustainable lithium-ion battery pyrometallurgical recycling process,” *Resour Conserv Recycl*, vol. 158, p. 104809, 2020.

[84] P. Meshram, B. D. Pandey, and T. R. Mankhand, “Hydrometallurgical processing of spent lithium ion batteries (LIBs) in the presence of a reducing agent with emphasis on kinetics of leaching,” *Chemical Engineering Journal*, vol. 281, pp. 418–427, 2015.

[85] J. Wang *et al.*, “Toward direct regeneration of spent lithium-ion batteries: a next-generation recycling method,” *Chem Rev*, vol. 124, no. 5, pp. 2839–2887, 2024.

[86] Z. Wu, H. Zhu, H. Bi, P. He, and S. Gao, “Recycling of electrode materials from spent lithium-ion power batteries via thermal and mechanical treatments,” *Waste Management & Research*, vol. 39, no. 4, pp. 607–619, 2021.

[87] J. Wang *et al.*, “Toward direct regeneration of spent lithium-ion batteries: a next-generation recycling method,” *Chem Rev*, vol. 124, no. 5, pp. 2839–2887, 2024.

[88] Y.-J. Shih, S.-K. Chien, S.-R. Jhang, and Y.-C. Lin, “Chemical leaching, precipitation and solvent extraction for sequential separation of valuable metals in cathode material of spent lithium ion batteries,” *J Taiwan Inst Chem Eng*, vol. 100, pp. 151–159, 2019.

[89] N. Vieceli, N. Reinhardt, C. Ekberg, and M. Petranikova, “Optimization of manganese recovery from a solution based on lithium-ion batteries by solvent extraction with D2EHPA,” *Metals (Basel)*, vol. 11, no. 1, p. 54, 2020.

[90] H. Wang and B. Friedrich, “Development of a highly efficient hydrometallurgical recycling process for automotive Li–Ion batteries,” *Journal of Sustainable Metallurgy*, vol. 1, no. 2, pp. 168–178, 2015.

[91] J. D. Miller and L. W. Beckstead, “Surface deposit effects in the kinetics of copper cementation by iron,” *Metallurgical transactions*, vol. 4, no. 8, pp. 1967–1973, 1973.

[92] P. Meshram, S. Virolainen, and T. Sainio, “Solvent extraction for separation of 99.9% pure cobalt and recovery of Li, Ni, Fe, Cu, Al from Spent LIBs,” *Metals (Basel)*, vol. 12, no. 6, p. 1056, 2022.

[93] P. K. Parhi, S. Panigrahi, K. Sarangi, and K. C. Nathsarma, “Separation of cobalt and nickel from ammoniacal sulphate solution using Cyanex 272,” *Sep Purif Technol*, vol. 59, no. 3, pp. 310–317, 2008.

[94] H. Shalchian, M. Khalili, A. Kiani-Rashid, B. Nateq, and F. Vegliò, “Selective Leaching of Lithium and Beyond: Sustainable Eggshell-Mediated Recovery from Spent Li-Ion Batteries,” *Minerals*, vol. 14, no. 11, p. 1120, 2024.

[95] A. Keller, M. W. Hlawitschka, and H.-J. Bart, “Application of saponified D2EHPA for the selective extraction of manganese from spend lithium-ion batteries,” *Chemical Engineering and Processing-Process Intensification*, vol. 171, p. 108552, 2022.

[96] S. Wu, N. Kaden, and K. Dröder, “A Systematic Review on Lithium-Ion Battery Disassembly Processes for Efficient Recycling,” Jun. 01, 2023, *MDPI*. doi: 10.3390/batteries9060297.

[97] G. D. J. Harper *et al.*, “Roadmap for a sustainable circular economy in lithium-ion and future battery technologies,” *JPhys Energy*, vol. 5, no. 2, Apr. 2023, doi: 10.1088/2515-7655/acaa57.

[98] T. Younas, F. Veglio, M. Prisciandaro, and V. Innocenzi, “Assessing risks and safety protocols in the dismantling of lithium-ion batteries,” in *10TH INTERNATIONAL SYMPOSIUM ON ENERGY FROM BIOMASS AND WASTE HOTEL MONACO & GRAND CANAL, VENICE (IT)*, VENICE (IT): 10TH INTERNATIONAL SYMPOSIUM ON ENERGY FROM BIOMASS AND WASTE HOTEL MONACO & GRAND CANAL, VENICE (IT) / 25-27 NOVEMBER 2024, 2024.

[99] J. Hassoun, F. Croce, I. Hong, and B. Scrosati, “Lithium-iron battery: Fe2O3 anode versus LiFePO4 cathode,” *Electrochem commun*, vol. 13, no. 3, pp. 228–231, 2011.

[100] M. David *et al.*, “Critical raw materials,” *Future-Proofing Fuel Cells: Critical Raw Material Governance in Sustainable Energy*, pp. 15–33, 2021.

[101] J. Tomala and M. Urbaniec, “Towards sustainable development in the European Union: a critical raw materials perspective,” *Economics and Environment*, vol. 88, no. 1, p. 654, 2024.

[102] S. Zhang, C. Zhang, X. Zhang, and E. Ma, “A mechanochemical method for one-step leaching of metals from spent LIBs,” *Waste Management*, vol. 161, pp. 245–253, 2023.

[103] M. Svärd, C. Ma, K. Forsberg, and P. G. Schiavi, “Addressing the Reuse of Deep Eutectic Solvents in Li-Ion Battery Recycling: Insights into Dissolution Mechanism, Metal Recovery, Regeneration and Decomposition,” 2024, *John Wiley and Sons Inc*. doi: 10.1002/cssc.202400410.

[104] V. Reisch, “The race for raw materials: contributions to the debate on the EU’s raw materials policy following the publication of the Fourth Critical Raw Materials List and the 2020 Action Plan,” 2022.

[105] F. Forte, M. Pietrantonio, S. Pucciarmati, M. Puzone, and D. Fontana, “Lithium iron phosphate batteries recycling: An assessment of current status,” *Crit Rev Environ Sci Technol*, vol. 51, no. 19, pp. 2232–2259, 2021.

[106] T. Younas, H. Shalchian, P. Romano, Z. Yao, F. Vegliò, and V. Innocenzi, “A novel integrated approach for selective separation and recovery of critical metals from ground cathode-anode mixtures of spent li-ion batteries,” *J Energy Storage*, vol. 129, p. 117373, 2025.

[107] P. Yadav, C. J. Jie, S. Tan, and M. Srinivasan, “Recycling of cathode from spent lithium iron phosphate batteries,” *J Hazard Mater*, vol. 399, p. 123068, 2020.

[108] X. Liang, J. Tang, L. Li, Y. Wu, and Y. Sun, “A review of metallurgical processes and purification techniques for recovering Mo, V, Ni, Co, Al from spent catalysts,” *J Clean Prod*, vol. 376, p. 134108, 2022.

[109] X. Chen, Y. Chen, T. Zhou, D. Liu, H. Hu, and S. Fan, “Hydrometallurgical recovery of metal values from sulfuric acid leaching liquor of spent lithium-ion batteries,” *Waste management*, vol. 38, pp. 349–356, 2015.

[110] H. Wang and B. Friedrich, “Development of a highly efficient hydrometallurgical recycling process for automotive Li–Ion batteries,” *Journal of Sustainable Metallurgy*, vol. 1, pp. 168–178, 2015.

[111] V. Chaudhary, P. Lakhera, K.-H. Kim, A. Deep, and P. Kumar, “Insights into the eco-friendly recovery process for valuable metals from waste lithium-ion batteries by organic acids leaching,” *Separation & Purification Reviews*, vol. 53, no. 1, pp. 82–99, 2024.

[112] B. K. Biswal, U. U. Jadhav, M. Madhaiyan, L. Ji, E.-H. Yang, and B. Cao, “Biological leaching and chemical precipitation methods for recovery of Co and Li from spent lithium-ion batteries,” *ACS Sustain Chem Eng*, vol. 6, no. 9, pp. 12343–12352, 2018.

[113] D. Song *et al.*, “Characteristic comparison of leaching valuable metals from spent power Li-ion batteries for vehicles using the inorganic and organic acid system,” *J Environ Chem Eng*, vol. 10, no. 1, p. 107102, 2022.

[114] S. Zhang, C. Zhang, X. Zhang, and E. Ma, “A mechanochemical method for one-step leaching of metals from spent LIBs,” *Waste Management*, vol. 161, pp. 245–253, 2023.

[115] H. Palomäki, “Electrochemical methods for the recovery of battery metals from lithium-ion battery waste leach solutions,” 2021.

[116] N. Zhang, “Efficient methods for recycling cathodes of spent lithium-ion batteries,” 2022.

[117] M. Wang *et al.*, “Recycling of lithium iron phosphate batteries: Status, technologies, challenges, and prospects,” *Renewable and Sustainable Energy Reviews*, vol. 163, p. 112515, 2022.

[118] H. Li, S. Xing, Y. Liu, F. Li, H. Guo, and G. Kuang, “Recovery of lithium, iron, and phosphorus from spent LiFePO4 batteries using stoichiometric sulfuric acid leaching system,” *ACS Sustain Chem Eng*, vol. 5, no. 9, pp. 8017–8024, 2017.

[119] J. Cong *et al.*, “Study on deep synergistic leaching mechanism of spent lithium iron phosphate under the H2SO4-H2O2 system and precise chemical precipitation recovery strategy of lithium carbonate,” *Sep Purif Technol*, vol. 363, p. 132326, 2025.

[120] S. Kim *et al.*, “A comprehensive review on the pretreatment process in lithium-ion battery recycling,” *J Clean Prod*, vol. 294, p. 126329, 2021.

[121] M. Kaya and S. Hussaini, “Hydrometallurgical Processing of Electronic Waste,” *Electronic Waste Management: Policies, Processes, Technologies, and Impact*, pp. 254–269, 2023.

[122] M. Bruno, C. Francia, and S. Fiore, “Closed-loop recycling of lithium iron phosphate cathodic powders via citric acid leaching,” *Environmental Science and Pollution Research*, pp. 1–16, 2024.

[123] R. Lerchbammer, E. Gerold, and H. Antrekowitsch, “Gluconic acid leaching of spent lithium-ion batteries as an environmentally friendly approach to achieve high leaching efficiencies in the recycling of NMC active material,” *Metals (Basel)*, vol. 13, no. 8, p. 1330, 2023.

[124] S. Lei *et al.*, “Tailoring crystal plane of short-process regenerated LiFePO4 towards enhanced rate properties,” *Journal of Energy Chemistry*, vol. 99, pp. 458–465, 2024.

[125] M. Ali, N. Iqbal, T. Noor, and N. Zaman, “Selective lithium recovery from spent LFP Li-ion batteries using organic acids,” *Ionics (Kiel)*, vol. 31, no. 1, pp. 273–286, 2025.

[126] P. K. Choubey, M. Kim, R. R. Srivastava, J. Lee, and J.-Y. Lee, “Advance review on the exploitation of the prominent energy-storage element: Lithium. Part I: From mineral and brine resources,” *Miner Eng*, vol. 89, pp. 119–137, 2016.

[127] J. C. Kelly, M. Wang, Q. Dai, and O. Winjobi, “Energy, greenhouse gas, and water life cycle analysis of lithium carbonate and lithium hydroxide monohydrate from brine and ore resources and their use in lithium ion battery cathodes and lithium ion batteries,” *Resour Conserv Recycl*, vol. 174, p. 105762, 2021.

[128] V. Reisch, “The race for raw materials: contributions to the debate on the EU’s raw materials policy following the publication of the Fourth Critical Raw Materials List and the 2020 Action Plan,” 2022.

[129] B. E. Murdock, K. E. Toghill, and N. Tapia-Ruiz, “A perspective on the sustainability of cathode materials used in lithium-ion batteries,” *Adv Energy Mater*, vol. 11, no. 39, p. 2102028, 2021.

[130] A. Mayyas, D. Steward, and M. Mann, “The case for recycling: Overview and challenges in the material supply chain for automotive li-ion batteries,” *Sustainable materials and technologies*, vol. 19, p. e00087, 2019.

[131] X. Chen, B. Xu, T. Zhou, D. Liu, H. Hu, and S. Fan, “Separation and recovery of metal values from leaching liquor of mixed-type of spent lithium-ion batteries,” *Sep Purif Technol*, vol. 144, pp. 197–205, 2015.

[132] A. P. Paiva and C. A. Nogueira, “Ionic liquids in the extraction and recycling of critical metals from urban mines,” *Waste Biomass Valorization*, vol. 12, no. 4, pp. 1725–1747, 2021.

[133] E. Worrell and M. A. Reuter, *Handbook of Recycling: State-of-the-art for Practitioners, Analysts, and Scientists*. Newnes, 2014.

[134] E. Sayilgan *et al.*, “A review of technologies for the recovery of metals from spent alkaline and zinc–carbon batteries,” *Hydrometallurgy*, vol. 97, no. 3–4, pp. 158–166, 2009.

[135] R. Mende, D. Kaiser, S. Pavón, and M. Bertau, “The COOL process: A holistic approach towards lithium recycling,” *Waste Biomass Valorization*, vol. 14, no. 9, pp. 3027–3042, 2023.

[136] P. Rasoulnia, R. Barthen, K. Valtonen, and A.-M. Lakaniemi, “Impacts of phosphorous source on organic acid production and heterotrophic bioleaching of rare earth elements and base metals from spent nickel-metal-hydride batteries,” *Waste Biomass Valorization*, vol. 12, no. 10, pp. 5545–5559, 2021.

[137] R. K. Nekouei, S. Maroufi, S. S. Mofarah, and V. Sahajwalla, “Regeneration of waste Zn-MnO2 batteries: value-added transformation to regenerate essential materials for sustainable battery manufacturing,” *J Energy Storage*, vol. 80, p. 110159, 2024.

[138] X. Xiang, F. Xia, L. Zhan, and B. Xie, “Preparation of zinc nano structured particles from spent zinc manganese batteries by vacuum separation and inert gas condensation,” *Sep Purif Technol*, vol. 142, pp. 227–233, 2015.

[139] X. Hu, A. Robles, T. Vikström, P. Väänänen, M. Zackrisson, and G. Ye, “A novel process on the recovery of zinc and manganese from spent alkaline and zinc-carbon batteries,” *J Hazard Mater*, vol. 411, p. 124928, 2021.

[140] Y. Chen, S. Li, S. Lin, M. Chen, C. Tang, and X. Liu, “Promising energy-storage applications by flotation of graphite ores: A review,” *Chemical Engineering Journal*, vol. 454, p. 139994, 2023.

[141] D. Davoise, G. Gascó, P. Almendros, and A. Méndez, “Advances in the potential application of froth flotation for the recovery of graphite from spent alkaline and Zn/C batteries,” *J Mater Cycles Waste Manag*, vol. 27, no. 6, pp. 4730–4747, 2025.

[142] C. A. Young, *SME mineral processing and extractive metallurgy handbook*. Society for Mining, Metallurgy & Exploration, 2019.

[143] A. D. Jara, A. Betemariam, G. Woldetinsae, and J. Y. Kim, “Purification, application and current market trend of natural graphite: A review,” *Int J Min Sci Technol*, vol. 29, no. 5, pp. 671–689, 2019.

[144] H. Wang *et al.*, “Reclaiming graphite from spent lithium ion batteries ecologically and economically,” *Electrochim Acta*, vol. 313, pp. 423–431, 2019.

[145] M. Abdollahifar, S. Doose, H. Cavers, and A. Kwade, “Graphite recycling from end-of-life lithium-ion batteries: processes and applications,” *Adv Mater Technol*, vol. 8, no. 2, p. 2200368, 2023.

[146] L. Yang *et al.*, “Closed-loop regeneration of battery-grade FePO4 from lithium extraction slag of spent Li-ion batteries via phosphoric acid mixture selective leaching,” *Chemical Engineering Journal*, vol. 431, p. 133232, 2022.

[147] B. Moradi and G. G. Botte, “Recycling of graphite anodes for the next generation of lithium ion batteries,” *J Appl Electrochem*, vol. 46, no. 2, pp. 123–148, 2016.

[148] S. Natarajan, S. R. Ede, H. C. Bajaj, and S. Kundu, “Environmental benign synthesis of reduced graphene oxide (rGO) from spent lithium-ion batteries (LIBs) graphite and its application in supercapacitor,” *Colloids Surf A Physicochem Eng Asp*, vol. 543, pp. 98–108, 2018.

[149] L. De Vita *et al.*, “A Green Process for Effective Direct Recycling and Reuse of Graphite from End-of-Life Li-Ion Batteries Black Mass,” *ChemSusChem*, vol. 18, no. 17, p. e202500550, 2025.

[150] J. Wu *et al.*, “Direct recovery: A sustainable recycling technology for spent lithium-ion battery,” *Energy Storage Mater*, vol. 54, pp. 120–134, 2023.

[151] P. Cattaneo *et al.*, “Sorting, Characterization, Environmentally Friendly Recycling, and Reuse of Components from End-of-Life 18650 Li Ion Batteries,” *Adv Sustain Syst*, vol. 7, no. 9, p. 2300161, 2023.

[152] E. Asadi Dalini, G. Karimi, S. Zandevakili, and M. Goodarzi, “A review on environmental, economic and hydrometallurgical processes of recycling spent lithium-ion batteries,” *Mineral Processing and Extractive Metallurgy Review*, vol. 42, no. 7, pp. 451–472, 2021.

[153] L. Yang *et al.*, “Separation and recovery of carbon powder in anodes from spent lithium-ion batteries to synthesize graphene,” *Sci Rep*, vol. 9, no. 1, p. 9823, 2019.

[154] G. Harper *et al.*, “Recycling lithium-ion batteries from electric vehicles,” *Nature*, vol. 575, no. 7781, pp. 75–86, 2019.

Finanziato dall'Unione europea-*NextGeneration EU*
Missione 4, Componente 1 – CUP E13C22001060006